Politecnico di Torino

Hard chrome plating & alternative coatings in the automotive industry

TESI DI LAUREA MAGISTRALE IN
AUTOMOTIVE ENGINEERING
INGEGNERIA DELL'AUTOVEICOLO

Academic Year: 2022-23

Candidate: **Vishnu Narayanan Chittilamana Mohanakumar**

Student ID: S291049
Advisor: Professor Paolo Matteis (DISAT)
Company advisor: Giancarlo Marchiaro

Abstract

Hexavalent chromium coating technology is one of the most sought out electrolytic coating processes adopted in the automotive industry. These coatings possess exceptional corrosion resistance, wear and tear resistance and hardness making them suitable for applications in the automotive industry. However, There has been a growing concern regarding its applications as it accounts for carcinogenic and hazardous properties. Due to this, strict restrictions has been imposed by REACH (Registration, Evaluation, Authorization and Restriction of Chemicals) and EPA (Environmental Protection Agency) in Europe and the USA respectively regarding the usage of hexavalent chromium. As a result, there have been efforts to explore high quality coating techniques that do not depend on electrolysis. This thesis deals with the characterization of hard chrome coatings, mainly hexavalent chromium and trivalent chromium, and other alternative coatings (in view of reducing the usage of hexavalent chromium) such as PVD & CVD, electroless nickel, and heat treatment by gas nitriding process on metal substrates (steel). The primary tests employed to study the coatings were optical microscopy & scanning electron microscopy (EDS) for morphological analysis, neutral salt spray test for corrosion resistance, vicker's hardness test for evaluating micro-hardness, and again microscopic analysis for thickness inspection. The analysis were carried out at the group materials laboratory of Centro Ricerche Fiat (CRF), Italy. Although, it was already understood that hexavalent chromium will show excellent properties while subjected to these tests, the study was primarily focussed on understanding the behaviour of alternative coatings and how they can be used for various applications in terms of varying functionalities, thus highlighting the need for alternate solutions, all the while giving importance to sustainability and green manufacturing in the coating processes.

.

Key-words: Hexavalent chromium, Sustainability, Coating characterization, PVD & CVD coatings, Electroless nickel coatings.

Abstract in Italiano

La tecnologia di rivestimento al cromo esavalente è uno dei processi di rivestimento elettrolitico più ricercati adottati nell'industria automobilistica. Questi rivestimenti possiedono un'eccezionale resistenza alla corrosione, resistenza all'usura e durezza che li rendono adatti per applicazioni nell'industria automobilistica. Tuttavia, c'è stata una crescente preoccupazione per quanto riguarda le sue applicazioni in quanto rappresenta proprietà cancerogene e pericolose. Per questo motivo, sono state imposte severe restrizioni da parte di REACH (Registration, Evaluation, Authorization and Restriction of Chemicals) e EPA (Environmental Protection Agency) rispettivamente in Europa e negli Stati Uniti per quanto riguarda l'uso del cromo esavalente. Di conseguenza, ci sono stati sforzi per esplorare tecniche di rivestimento di alta qualità che non dipendano dall'elettrolisi. Questa tesi si occupa della caratterizzazione di rivestimenti di cromo duro, principalmente cromo esavalente e cromo trivalente, e di altri rivestimenti alternativi (al fine di ridurre l'uso di cromo esavalente) come PVD e CVD, nichel chimico e trattamento termico mediante processo di nitrurazione gassosa su substrati metallici (acciaio). I test principali impiegati per studiare i rivestimenti sono stati la microscopia ottica e la microscopia elettronica a scansione (EDS) per l'analisi morfologica, il test in nebbia salina neutra per la resistenza alla corrosione, il test di durezza di vicker per la valutazione della microdurezza e di nuovo l'analisi microscopica per l'ispezione dello spessore. Le analisi sono state effettuate presso il laboratorio materiali del Gruppo del Centro Ricerche Fiat (CRF), Italia. Sebbene si fosse già capito che il cromo esavalente avrebbe mostrato eccellenti proprietà durante la sottoposizione a questi test, lo studio si è concentrato principalmente sulla comprensione del comportamento dei rivestimenti alternativi e su come possano essere utilizzati per varie applicazioni in termini di funzionalità variabili, evidenziando così la necessità di soluzioni alternative, dando importanza alla sostenibilità e alla produzione green nei processi di rivestimento.

Parole chiave: Cromo esavalente, Sostenibilità, Caratterizzazione dei rivestimenti, Rivestimenti PVD e CVD, Rivestimenti in nichel chimico.

Acknowledgements

First of all, I would like to thank my thesis advisor, Professor Paolo Matteis (DISAT), for providing me with the wonderful opportunity of doing a thesis in the field of metal coatings in collaboration with Centro Ricerche Fiat (CRF), Italy. His guidance and mentership was critical in carrying out the research effectively.

Additionally, I would like to thank Mr. Giancarlo Marchiaro, my supervisor in the company, whose excellent guidance and expertise in the field of coatings made it very helpful for carrying out the different analysis. I would also like to extend my sincere gratitude to all the people in the R&D, Materials & Sustainability department, CRF, for helping me out with the characterization of different coatings.

Last but not least, I want to express my gratitude to my family and close friends for their unwavering support throughout all of my professional endeavors, particularly my pursuit of a Master of Science in Automotive Engineering. They were always there to offer comfort and words of encouragement to get me through the tough times, especially when I was feeling self-conscious.

Table of Contents

List of Figures

List of Tables

Introduction

One of the earliest inventions that is recognized for improving the shape and function of the material it protects is metal coating, often known as surface finishing. On both metallic and non-metallic materials known as substrates, it can be used as a surface protectant. Its lengthy history has had a significant impact on global community infrastructures, almost every industry, and millions of people's general quality of life. When it comes to surface finishing, electroplating leads the line. Electroplating is a process that involves adding a layer of metal onto either a conductive or specially treated nonconductive surface. This is achieved by passing a current through a solution allowing metal ions to accumulate and form the desired coating. It's quite versatile as it can be used with metals, like cadmium, chromium, and copper for purposes such as improving resistance to corrosion or creating attractive finishes (Horner, 1994). The most widely used electroplating technique has been chromium plating due to their excellent properties such as high corrosion resistance, high wear & tear, and high hardness. Chromium plating is of two types: Hexavalent chromium (Cr (VI)) & Trivalent chromium (Cr (III)). Even if many systems are now more dependable and durable thanks to metal coatings, some coating application techniques (Cr (VI)) have sparked criticism due to unfavorable outcomes. Chrome coating is hazardous because it uses extremely poisonous chromium precursors and is applied electrolytically (high current) in extremely low pH acid baths (K. Legg, M. Graham, P. Chang, F. Rastagar, A. Gonzales and B. Sartwell, May 1996). There is an effort to identify more environmentally friendly coating methods to replace the current ones that present significant threats to the environment, among other reasons (R. A. Lane, C. Fink, C. Grethlein and N. Rome, Sept. 2012) (K. Legg, M. Graham, P. Chang, F. Rastagar, A. Gonzales and B. Sartwell, May 1996).

Considering the toxic aspects of chromium coatings, electroless coating techniques such as electroless nickel, CVD & PVD coatings have gained popularity due to their environmentally friendly aspects. Electroless deposition is one of the most refined techniques for alloy generation. The technique exploits the autocatalytic reduction of cations by electrons released from suitable chemical reducing agents at the substrate/solution interface to form binary, tertiary, or even quaternary alloys. Not only can coatings be produced in homogeneous or microcrystalline non-equilibrium states using the electroless deposition technique, but heat treatment after deposition can be used to successfully produce the more commonly recognized equilibrium phases, expanding the range of properties that can be achieved and, consequently, the applications that the technique can be applied to. Similarly, Chemical Vapor

Deposition (CVD) and Physical Vapor Deposition (PVD) are two cutting edge coating methods widely utilized across industries. CVD involves applying a high-quality film onto a surface by reacting precursors chemically. This results in distribution and precise control over the films' characteristics. On the other hand, PVD is a process where a source material is evaporated or sputtered and then condensed onto the surface offering outstanding adhesion and resistance to wear. Both CVD and PVD coatings enhance surface properties providing durability protection against corrosion and customized functionalities for surfaces. These techniques have become very popular in fields such as electronics, automotives, aerospace engineering and the manufacturing of cutting tools.

This thesis focuses on the characterization of all the previously mentioned coatings using different characterization tests performed at the group materials laboratory of Centro Ricerche Fiat (CRF), Italy, in order to understand and analyze the properties of various coatings. By doing so, the properties & behavior of alternative coatings to hexavalent chromium is studied, which in turn is crucial in reducing the usage of hexavalent chromium thus promoting green coating processes. Going deeper into this study, the first four chapters focuses on the theoretical study part of the coatings with lots of existing research data, while the remaining chapters focuses on characterization of the coatings providing sufficient and substantial results.

1 Hard Chrome Plating – a theoretical study

When it comes to the discussion of coating technologies in any sort of industry, Chrome plating takes the forefront. Chrome plating, in the Automotive industry, is a widely utilized electroplating technique to enhance the aesthetic appeal as well as the functionalities of various automotive components. Generally, there is decorative chrome plating (solely for aesthetic appeal) for plastics and hard chrome plating (in view of achieving functional durability) for metals. The technique is carried out by depositing a thin layer of chromium onto a base metal or plastic (substrate) through various processes. The material after hard chrome plating possesses properties such as exceptional corrosion resistance, high hardness, and excellent reflective properties, thus making it very much suitable to be applied on components such as bumpers, trims, cam shafts, rocker arms of shock absorbers and so on. Hard chrome plating is mainly of two types, hexavalent chromium (Cr (VI)) and trivalent chromium (Cr (III)). This thesis delves into the characterisation of the above-mentioned coatings as well as some alternate coatings such as CVD & PVD coatings, electroless nickel coatings on pulleys, and about the reduction in usage of hexavalent chromium to reduce its toxic effects.

1.1. Chromium plating process

Automotive industry is one of the most demanding sectors for the application of chromium plating and it uses special specifications, which require exceptional quality of deposits, with resistance to climate changes and extremely high corrosion resistance. Electrolytic deposition of chromium began during the third decade of the twentieth century. Electrodeposited metals are often an ideal means of providing a thin surface coating which has some properties superior to that of the substrate. It may, for example, be possible to employ a cheaper or stronger substrate than could otherwise be used and yet achieve good corrosion resistance by applying a suitable electrodeposited coating. Chromium is used to take advantage of its characteristics of stainlessness, brightness and corrosion resistance. Chromium plating is used to enable materials that are cheaper and simpler to process, like steel and plastic. Chromium and

nickel form the most important couple of metals in the galvanic deposition. We can have two kind of deposition:

- Decorative chromium: a thin layer (less than 1 μm) with bright lasting appearance.
- Hard chromium: deposition (with standard thicknesses ranging from 200 to 600 μm) for industrial applications that has high resistance for oxidation, wear, abrasion, corrosion and low friction coefficient.

However, our attention is on hard chrome plating on metals, particularly on **steel** samples. Generally, hard chromium coatings can be divided into two. Hexavalent chromium coatings (Cr (VI)) and trivalent chromium (Cr(III)) coatings. In this section, we are going to observe in detail the plating line process for hard chrome coatings in general and their technical data.

1.1.1. Hard chromium process flow

To provide a surface that is resistant to wear, has a low coefficient of friction, is hard, resistant to corrosion, and may be used to replenish surfaces that have been worn down by use, hard plating involves directly depositing a reasonably thick coating of chromium on the base metal, which is typically steel. Products including plastic molds, machinery rolls, zinc die castings, hydraulic cylinders and rods, engine parts, and marine hardware are all coated with hard plating.

A flow diagram of the hard chromium electroplating process is shown (Figure 1.1) (Electroplating). Alkaline cleaning, chromic acid anodizing, chromium electroplating, and preparation make up the procedure. Grinding, polishing, and degreasing are examples of preparation procedures (Electroplating). Thinning out involves either submerging the component in organic solvents, like perchloroethylene or trichloroethylene, or eliminating surface grease utilizing the fumes from organic solvents. When using alkaline cleansing, utilizing inorganic cleaning agents like sodium phosphate or carbonate, remove surface dirt. Sodium hydroxide, perhaps. To remove oxide coatings or tarnish, one optional method is acid immersion generated throughout the alkaline cleaning process and to balance the alkaline layer. Solutions for acid dips usually include between 10% and 30% sulfuric or hydrochloric acid. Another alternative procedure that cleans the metal surface and improves chromium adherence during the electroplating process is chromatic acid anodic treatment. The electroplating procedure itself is the process's last stage (Electroplating).

A heat exchanger of some kind is usually installed in the plating tanks. Bath composition and temperature are consistently maintained by using compressed air or mechanical agitators connected to pipes on the bottom of the tank. It takes continual

supervision of the plating bath to electroplate chromium bath composition, plating duration, temperature, and current density (Electroplating).

The most popular baths for plating chromium on metal are those containing hexavalent chromium. Water, sulfuric acid, and chromic acid make up hexavalent chromium baths. The hexavalent chromium that reacts and deposits on the metal is produced by the chromic acid released into the air (Electroplating). The processes leading to chromium deposition are catalyzed by the sulfuric acid present in the bath. It takes between 80 and 90 minutes for hydrogen gas to evolve from chemical reactions at the cathode. 90% of the electricity used for the plating bath, with the remaining 10% to 20% going towards the reaction to deposition. Misting appears at the plating's surface as a result of the hydrogen gas evolving bath, which causes chromic acid to be lost into the atmosphere (Electroplating).

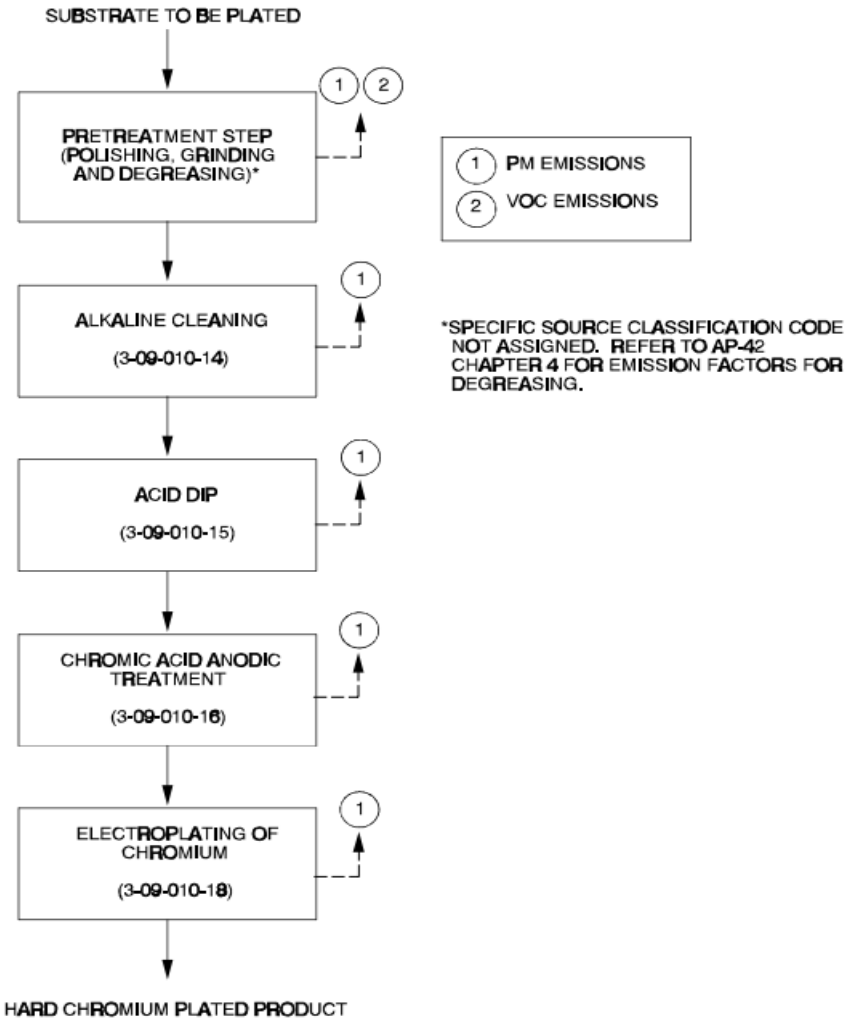

Figure 1.1 Hard chromium process flow.

1.2. Hard Chrome plating characterization – Crack density & Tribology

From the early 1930's, electrolytic hard-chrome coatings have been in practice in various industries such as Aerospace, Automotive, Medical, Military and so on for applications that require extensive corrosion resistance and wear and tear protection (B. Podgornik, O. Massler, F. Kafexhiu, M. Sedlacek, 2018). Although they have been in practice for a long time, the environmental hazards and health issues related predominantly to the use of hexavalent chromium cannot be neglected that easily. Because of this, there have been strict regulations imposed in Europe by REACH (REACH stands for Registration, Evaluation, Authorization and Restriction of Chemicals) and in the USA by EPA (Environmental Protection Agency) (B. Podgornik, O. Massler, F. Kafexhiu, M. Sedlacek, 2018). It is quite a known fact that Cr (VI) is a carcinogen which affects the respiratory system, kidneys, liver, skin, and eyes (B. Podgornik, O. Massler, F. Kafexhiu, M. Sedlacek, 2018). The predominant reason behind this is associated with the plating process and the treatment of chemicals and rather not with the final plated substrate metal (B. Podgornik, O. Massler, F. Kafexhiu, M. Sedlacek, 2018). So, even after identifying this serious issue, the complete replacement of hexavalent chromium is practically impossible because of their unmatched aesthetics and far greater technical capabilities such as high corrosion resistance, low value of friction coefficient, adhesion, low deposition temperatures high hardness and excellent wear resistance (B. Podgornik, O. Massler, F. Kafexhiu, M. Sedlacek, 2018).

Nonetheless, the different properties that has been mentioned here can be observed by varying the process parameters associated with coating process (B. Podgornik, O. Massler, F. Kafexhiu, M. Sedlacek, 2018). Usually, the coating thickness of hard chrome ranges from several hundred microns to a few hundred microns. Similarly, the hardness number for the same ranges from 65 to 68 HRC. However, the performance of hard chrome coatings not only depends on these properties, but also on the micro cracks and the tensile residual stresses developed during the chrome plating process (B. Podgornik, O. Massler, F. Kafexhiu, M. Sedlacek, 2018). During the hard chrome plating process, it has been observed that the coatings creep during the process because of the change in lattice structure which in turn leads to the generation of micro cracks or internal tensile stresses (B. Podgornik, O. Massler, F. Kafexhiu, M. Sedlacek, 2018).

Generally, the cracks observed in hard chrome plated metals have a typical depth of about 2 micrometers. Now, this might not seem to be a severe issue at first glance, but there is always the possibility of crack propagation, i.e., the association of different cracks to form dendritic structures of varying size, depth, and density. An adverse

effect of crack patterns is that it can severely reduce the corrosion resistance of the electroplated components (B. Podgornik, O. Massler, F. Kafexhiu, M. Sedlacek, 2018). Nonetheless, they also provide numerous positive effects such as increased surface wettability (B. Podgornik, O. Massler, F. Kafexhiu, M. Sedlacek, 2018) and increased surface area covered by the fluid film (B. Podgornik, O. Massler, F. Kafexhiu, M. Sedlacek, 2018). Going further into this review, an experimental study on the crack density and tribological performance of hard chrome coatings carried out (B. Podgornik, O. Massler, F. Kafexhiu, M. Sedlacek, 2018) is being analyzed. The study was aimed at how the crack size and density of the chrome plated components affects the wear performance of the same in a lubricated environment.

For this study, the material chosen for the base metal was AISI 52100 graded steel with a hardness number of about 60 HRC with a chemical composition of 1% C, 1.5% Cr, 0.35% Mn, 0.25% Si, bal. Fe. The material was disc shaped and surface polished to a surface roughness of 0.1 micrometres (B. Podgornik, O. Massler, F. Kafexhiu, M. Sedlacek, 2018). The different parameters such as deposition temperature, voltage, current density, and bath composition were altered for the purpose of obtaining crack patterns with varied crack density and crack width. In this study, the chromium coating was preserved with an amorphous microstructure alongside a 40-micrometre thickness. Since this study was to analyse how crack density affected the wear performance, 3 different samples with 3 different crack densities were prepared. They were, standard process A, standard process B with decreased density and standard process C, with much higher crack size and density. In order to obtain various surface topographies, a post-polishing process in synthetic naples cloth and 1 micrometre diamond paste further followed by ultrasound cleaning in acetone and ethanol was carried out (B. Podgornik, O. Massler, F. Kafexhiu, M. Sedlacek, 2018). The different surface topographies obtained are shown in Table 1.1.

Specimen	Process	Post-process	Crack density
A	Standard	–	Standard
A′	Standard	Polishing	Standard-smooth
B	Modified −	–	Reduced
B′	Modified −	Polishing	Reduced-smooth
C	Modified +	–	Increased
C′	Modified +	Polishing	Increased-smooth

Table 1.1 Hard Chrome coating variations, B Podgornik et al.

Morphological analysis using the JEOL JSM6500F scanning electron microscope on both the surface and cross-section of the coatings were carried out to calculate the width and depth of the cracks. Following the scanning electron microscopy, in order to determine the crack density, the ratio of average roughness to height of the selected

area, the root mean square height, the maximum height, the skewness, the curtosis and the developed interfacial ratio, the coatings were further observed with an Alicona infinite focus G4 3D optical microscope. The term interfacial ratio is defined as the percentage of extra surface area that has been contributed by the texture when it is compared with an ideal plane (B. Podgornik, O. Massler, F. Kafexhiu, M. Sedlacek, 2018). The interfacial ratio is mainly dependent on the amplitude of the texture and spacing. Higher the spacing and lower the amplitude, lower will be the interfacial ratio.

To analyse the tribological performance of the coatings, the principle of reciprocating sliding motion with the application of a ball on test configuration was adopted (B. Podgornik, O. Massler, F. Kafexhiu, M. Sedlacek, 2018) as shown in Figure 1.2. The setup consisted of a hardened 52,100 bearing steel ball with a 32 mm diameter and 60 HRC as the hardness, that is oscillating. Against this oscillating bearing, a hard chrome coated disc is loaded. For caarying out the friction and wear tests, mixed lubrication conditions were chosen to make the setup in such a way that half of the load is carried out by the lubricant and the other half by the roughness/irregularities (B. Podgornik, O. Massler, F. Kafexhiu, M. Sedlacek, 2018). Before carrying out the tests, the disc

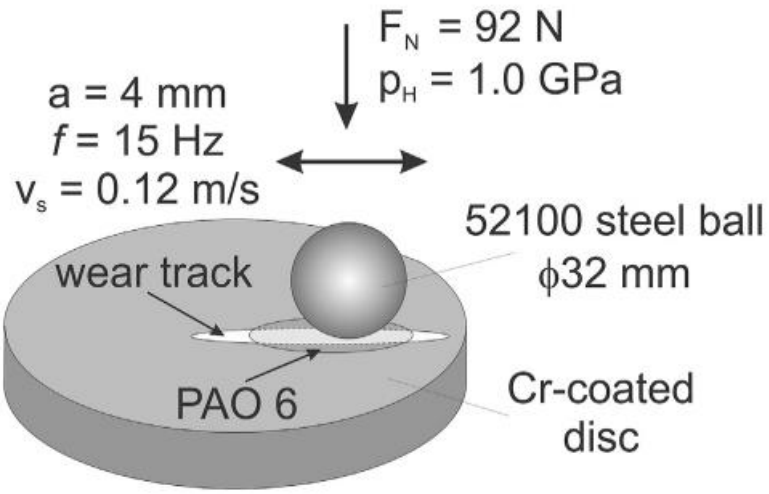

Figure 1.2 Tribo-test configuration, B Podgornik et al.

surface was applied with a homogenous film of non-additivated PAO 6 oil in the form a single droplet. The test load was set as 92 N and a contact pressure of 1 Gpa alongside with an average sliding speed of 0.12 m/s to ensure a mixed lubrication setup. An average sliding distance of 300 m was also maintained to ensure that the coated film

was stable (B. Podgornik, O. Massler, F. Kafexhiu, M. Sedlacek, 2018). The obtained test results were measured as the wear volume Wb of the steel ball and the coated specimen. Concerning the coefficient of friction, it was measured by evaluating the coefficient of friction vs. time. A 3D optical profilometer was used to measure the wear rate of the chromium coated disc (B. Podgornik, O. Massler, F. Kafexhiu, M. Sedlacek, 2018). The findings, from the analysis of surface topography can be found in Table 1.2.

Coating	Cracks		Roughness parameters					
	Width [μm]	Density [%]	S_a [μm]	S_q [μm]	S_z [μm]	S_{sk} [/]	S_{ku} [/]	S_{dr} [%]
A	0.389 ± 0.091	3.2 ± 0.3	0.31 ± 0.02	0.38 ± 0.02	10.93 ± 0.88	0.16 ± 0.06	3.80 ± 0.75	0.54 ± 0.02
A′	0.286 ± 0.088	2.6 ± 0.3	0.12 ± 0.01	0.16 ± 0.01	4.02 ± 0.40	−0.04 ± 0.03	4.98 ± 0.79	0.10 ± 0.01
B	0.288 ± 0.079	2.6 ± 0.2	0.16 ± 0.01	0.21 ± 0.01	5.26 ± 0.72	−0.23 ± 0.09	4.69 ± 0.91	0.17 ± 0.04
B′	0.240 ± 0.065	0.6 ± 0.1	0.14 ± 0.01	0.18 ± 0.02	4.17 ± 0.45	−0.05 ± 0.03	4.07 ± 1.05	0.13 ± 0.02
C	1.343 ± 0.336	17.2 ± 1.3	0.25 ± 0.01	0.31 ± 0.01	10.50 ± 1.36	−0.03 ± 0.09	11.84 ± 1.18	0.35 ± 0.03
C′	1.064 ± 0.321	14.0 ± 1.4	0.20 ± 0.01	0.25 ± 0.01	5.94 ± 0.91	0.07 ± 0.09	4.06 ± 1.05	0.25 ± 0.02

Table 1.2 Surface topography results, B Podgornik et al.

The changes made to the deposition process resulted in coating B, which achieved crack widths and densities as coating A after post polishing. However, the impact of post polishing was more significant, for coating B reducing the crack width to 0.24 μm and the crack density to 0.6% (B. Podgornik, O. Massler, F. Kafexhiu, M. Sedlacek, 2018). On the other hand, coating C exhibited the cracks and highest density of cracks with a cracking pattern consisting of numerous shorter cracks. In this case, the crack width exceeded 1.3 μm (B. Podgornik, O. Massler, F. Kafexhiu, M. Sedlacek, 2018). The density was over 17%. Additionally, after polishing, coating C still had a crack width above 1 μm and a crack density of about 14% which is times larger than coatings A and B (as shown in Table 1.2) (B. Podgornik, O. Massler, F. Kafexhiu, M. Sedlacek, 2018).

The variations in crack widths and densities are also evident, in the surface roughness/topography parameters. However, these differences do not directly correlate with scattering as all investigated crack widths and densities exhibit scattering characteristics (as indicated in Table 1.2). Coating A, which was applied using process parameters had the highest average surface roughness, among all the specimens examined (Podgornik B, Vilhena LM, Sedlacek M, Rek Z, Zun I, 2012). Surfaces with extremely high values of kurtosis and negative skewness are expected to exhibit better tribological properties under boundary and mixed lubrication conditions (Sedlacek M, Podgornik B, Vizintin J, 2012).

Through the polishing of coating A, a significant improvement in surface roughness was achieved, reducing the roughness parameters by a factor of 2.5 and decreasing the developed interfacial area ratio by a factor of 5 (Table 1.2) (B. Podgornik, O. Massler, F. Kafexhiu, M. Sedlacek, 2018).

According to the data presented in Table 1.2, it is evident that all three types of hard chrome coatings, A/, B/ and C/ exhibit skewness and kurtosis values (Ssk ≈ 0, Sku ≈ 4). (B. Podgornik, O. Massler, F. Kafexhiu, M. Sedlacek, 2018) regardless of the crack size and density. This information is crucial, for my literature review as it highlights the behavior of these coating variations in terms of their properties and surface characteristics.

Going on to the wear rate, which was the following metric. It was evident that surface qualities affected wear rates when it came to the steel ball (B. Podgornik, O. Massler, F. Kafexhiu, M. Sedlacek, 2018). Because of its plateau-like topography, which is characterized by negative skewness and extremely high kurtosis, Coating C had the lowest wear rate among the coatings applied originally, despite having a substantially greater amount of surface roughness (B. Podgornik, O. Massler, F. Kafexhiu, M. Sedlacek, 2018). With Coating A/ exhibiting the lowest wear rate and kurtosis for the steel ball, the polishing process greatly decreased wear rates. Moreover, there was a 30% decrease in the steel ball's wear rate fluctuations when coatings were post-polished (B. Podgornik, O. Massler, F. Kafexhiu, M. Sedlacek, 2018).

When moving from Coating A to Coating C, wear rates for the chrome disc adhesive markedly reduced. For denser fracture networks and advantageous surface characteristics, larger kurtosis values were predominantly responsible for this. Coating A/ showed the wear rate, whilst Coating C/ had the greatest, however polishing reversed this tendency (B. Podgornik, O. Massler, F. Kafexhiu, M. Sedlacek, 2018). Furthermore, there was no discernible relationship found between surface roughness and abrasive wear; instead, abrasive wear rates were correlated with smaller cracks and lower densities in the applied coatings (B. Podgornik, O. Massler, F. Kafexhiu, M. Sedlacek, 2018).

Another important parameter was the coefficient of friction. One of the main objectives was to develop techniques to reduce the coefficient of friction in systems in order to reduce energy consumption. In lubricated conditions, three distinct hard chrome coatings were inspected. Through post polishing, which produced a lubrication film and switched to film lubrication, a considerable reduction in friction was attained. Both Coatings A and B achieved a steady state coefficient of friction of 0.05 after polishing, however, the effects of surface smoothing and oil application were offset by deeper cracks and higher contact pressure resulting in coating C having saw the coefficient of friction value remained at 0.1 (B. Podgornik, O. Massler, F. Kafexhiu, M. Sedlacek, 2018).

The study also considered the coatings' running-in period. To attain a degree of friction during running in, Coating A needed about fifteen minutes or a 110-meter sliding distance (B. Podgornik, O. Massler, F. Kafexhiu, M. Sedlacek, 2018). In contrast to other coatings, Coating B demonstrated instant running in with low levels of friction because of its smaller and less thick fissures. Due to its fractures, Coating C accelerated

the running in process, although it did not lower friction levels. Significantly, post-polishing influenced the coating process because, because of the crack reservoirs, the coating ran with very little friction (around 0.05) (B. Podgornik, O. Massler, F. Kafexhiu, M. Sedlacek, 2018). There was a decrease in friction at first when Coating B was used. Unfortunately, crack-related problems meant that this improvement was only momentary. Conversely, Coating C performed well during the running-in process but had no appreciable effect in lowering friction (B. Podgornik, O. Massler, F. Kafexhiu, M. Sedlacek, 2018).

Additionally, the study (B. Podgornik, O. Massler, F. Kafexhiu, M. Sedlacek, 2018) showed that coating performance could not be determined by a single roughness parameter. Rather, a variety of variables including surface roughness, developed area ratio, skewness (a measure of asymmetry), and kurtosis (a measure of peakiness) were important (B. Podgornik, O. Massler, F. Kafexhiu, M. Sedlacek, 2018). Surfaces with plateaus were indicated by higher kurtosis values. It was discovered to be associated with better performance when the lubricant was used. By removing running in and lowering wear and friction, the post-polishing procedure greatly improved the characteristics. The degree of this improvement, which was dependent on the size and density of the cracks, included reaching low wear rates and a friction coefficient of about 0.05 (B. Podgornik, O. Massler, F. Kafexhiu, M. Sedlacek, 2018).

1.3. Hard chrome characterization – Microstructural observation & Microhardness of chrome coating by pulse plating

Pulse plating is a very popular means of technology that can be used to alter the microstructure of the coating layer (Yong Choi , M. Kim , S.C. Kwon , 2003). The different steps involved in the process are ion diffusion in front of the substrate, charge-transfer reaction, adatom formation, surface diffusion, growth and stress, ion relief during off-time (Yong Choi , M. Kim , S.C. Kwon , 2003). The microstructural alteration takes place due to the variation in current wave as the double layer in front of the substrate during plating is influenced by the amplitude and on/off time. Another important aspect is that during the pulse plating process, the instantaneous peak current density is very much higher than that of direct current plating process. Pulse plating results in crack free deposition as it allows for the selective deposition on a cathode. This is since the current pulses affect the charge transfer during the plating process (Yong Choi , M. Kim , S.C. Kwon , 2003).

Generally, it has been concluded that pulse plated chromium metals have a microstructure with well refined grains and low porosity. Going deeper into the lattice structure, from a cold electrolyte which has been kept at approximately 20 C, alpha-chromium that has a hexagonal closed packed structure was deposited. Similarly, a warm electrolyte kept somewhere around 50 C was used to deposit beta-chromium that has a body centered lattice configuration. Due to the presence of irregularities, defects, cracks, and residual stresses, the general corrosion resistance capability of chromium deposited metals in the usual bath is comparatively poor. To have a better understanding about the aftereffects of pulse on microstructure and mechanical properties of the plated components, the study conducted by (Yong Choi , M. Kim , S.C. Kwon , 2003) is considered.

By turning on and off the pulse currents, chromium was deposited on a copper surface using pulse plating. At 55°C, an electrochemical reaction took place in a solution containing 500 grams of acid per liter and 10 grams of sulfuric acid per liter. The study encompassed many analyses, including wear testing with a Taber wear tester and scanning electron microscopy to examine the shape of the deposited material. Furthermore, after being separated from the copper substrate, the chromium layers' structure was examined under a transmission electron microscope (Yong Choi , M. Kim , S.C. Kwon , 2003).

It was discovered that the thickness of the chrome increased with longer on/off periods, Figure 1.3 & Figure 1.4 indicating the significance of the duration of these periods as shown in table 1.3. The shape of the surface was also influenced by the pulse patterns, with nodules forming when the durations were longer, and the ratio of on/off times determined both sizes Fig. 1.5, and whether the surface had any cracks (Yong Choi , M. Kim , S.C. Kwon , 2003). The study concentrated on the process of chromium deposition onto a copper surface using patterns of pulse current.

On–off time (ms)	Thickness (μm)
5–5	8.7
15–15	15.7
30–30	21.4
45–45	22.1
60–60	25.6

Table 1.3 Average chrome thickness for a given plating time of 2.5 h by several pulsed currents, Y Choi et al.

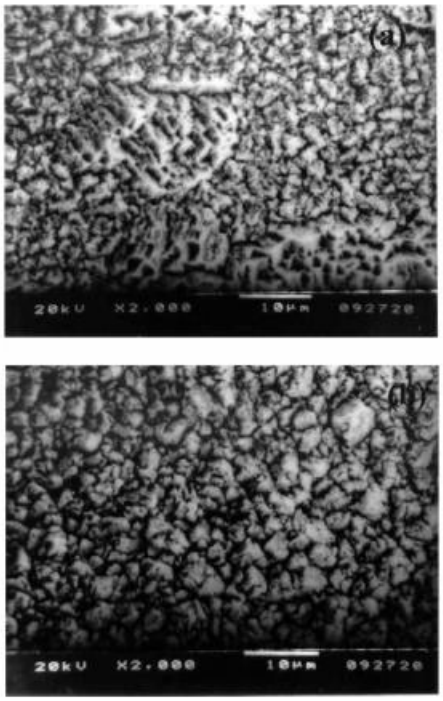

Figure 1.3 Surface morphology for Ton/Toff = 15/15 ms

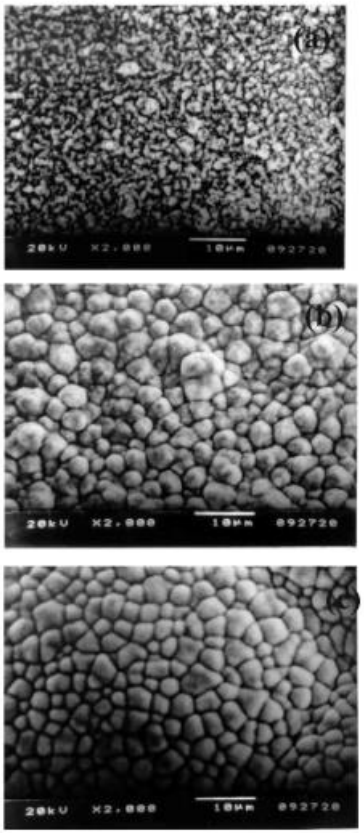

Figure 1.4 Surface morphology Ton/Toff = 30/30 ms

Upon getting the transmission electron micrograph results, it was discovered that pulse plating, as opposed to direct plating, considerably enlarged the size of the chrome grains. Stress was lessened because of this grain size change (Yong Choi , M. Kim , S.C. Kwon , 2003). Additionally, it was found that the hardness well declined as the length of on-off intervals decreased. Pulse length time and density both affected the chromium layer's resistance to wear. Direct current density and decreased wear resistance were related to each other; however, pulse current density and wear resistance were not (Yong Choi , M. Kim , S.C. Kwon , 2003). Pulse plating, in summary, influences wear resistance, hardness, residual stress, and grain size; nevertheless, the duration of the off period should get consideration Table 1.4. As the on/off time and peak voltage increased, so did the rate of chromium deposition with an equal on/off time ratio (Yong Choi , M. Kim , S.C. Kwon , 2003).

The smaller grain indicates that the length of off-time and on/off time ratio are the primary determinants of nodule size and form in the chrome development kinetic. The duration of the on/off period decreased the micro-hardness values of the pulse plated chrome layers (Yong Choi , M. Kim , S.C. Kwon , 2003).

On–off time (ms)	Knoop (100 g)	Taber wear factor
5–5	371.7	3.45
15–15	457.4	3.37
30–30	464.7	3.28
45–45	488.1	3.14
60–60	498.3	3.01
DC[a]	970.5	1.50

Table 1.4 Microhardness & wear susceptibility of chrome layers, Y Choi et al.

As the on/off time and peak voltage increased, so did the rate of chromium deposition with an equal on/off time ratio. The smaller grain indicates that the length of off-time and on/off time ratio are the primary determinants of nodule size and form in the chrome development kinetic (Yong Choi , M. Kim , S.C. Kwon , 2003). The duration of the on/off period decreased the micro-hardness values of the pulse plated chrome layers. The microstructural analysis using TEM and SEM indicated a drop in strength, which was associated with an increase in grain size and the release of residual stress during part-time employment Figure 1.6 (Yong Choi , M. Kim , S.C. Kwon , 2003).

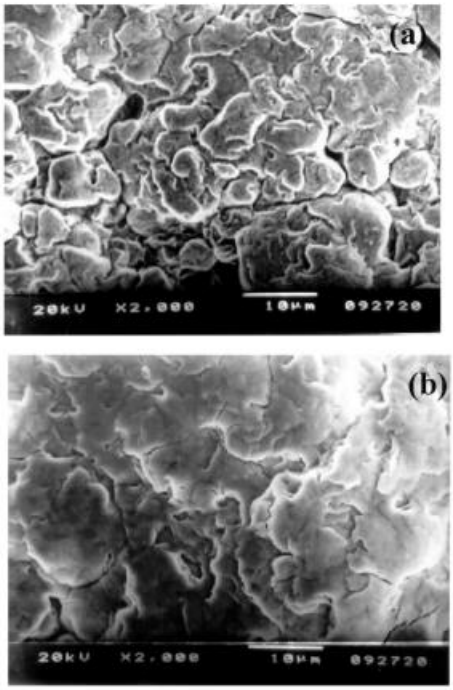

Figure 1.5 (a)Ton/Toff = 60/120 ms (b) Ton/Toff = 60/180 ms

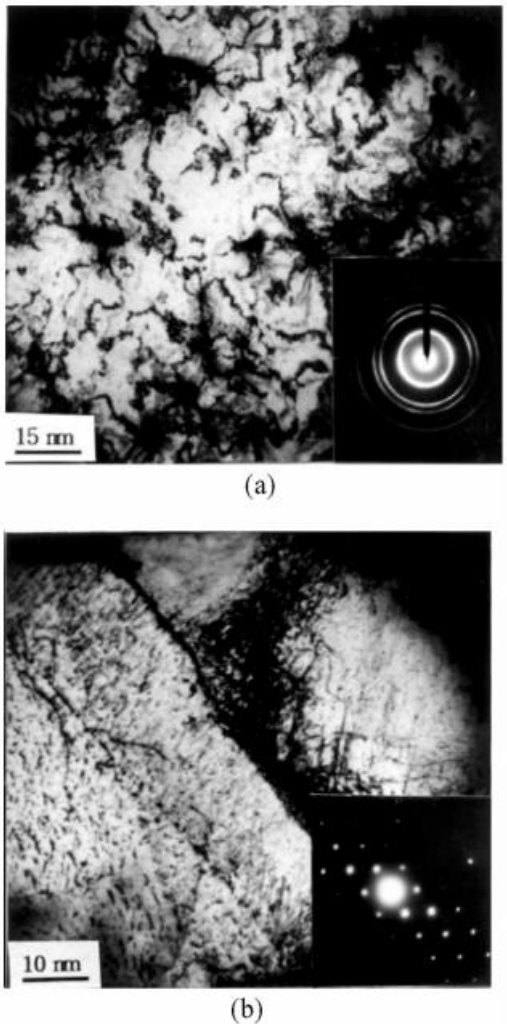

Figure 1.6 TEM images & SAD patterns (a) DC plating with 1.6 mA mm^{-2} (b) with 1.6 mA mm^{-2} and Ton/Toff = 5/5 ms

2 CVD & PVD coatings – a theoretical study

These days, hard coatings are frequently used in tools and automobile applications to decrease friction, increase wear and oxidation resistance, or both. An overview of the characterization of chemical and physical vapor deposition procedures pertinent to the synthesis of hard coatings, is provided in this chapter. With vapor deposition, coatings can be created atom by atom, frequently under non-equilibrium settings with kinetic constraints or when the film surface is exposed to severe ion irradiation while growing. These circumstances produce coatings with large defect densities and stresses, nanometer-sized grains, metastable phases, and high distances from thermodynamic equilibrium. Many of the various coatings that have been studied based on transition metal nitrides and carbonitrides, carbides, borides, oxides, and diamond-like carbon are now conventional materials in the coating industry. One can customize coating materials and phase or layer structures with specific property combinations by combining advanced synthesis techniques with theoretical predictions of phase stabilities and characteristics.

2.1. Process description

PVD and CVD processes play a major role in depositing layers of materials with precision. PVD involves transforming liquid source material into atoms or molecules transporting them through a vacuum or low-pressure environment and then condensing them onto a substrate (Donald M. Mattox). It offers flexibility allowing the deposition of films that ranges from a nanometer to several micrometers thick (Donald M. Mattox). PVD finds applications in areas including creating layer coatings and shaping complex forms.

On the other hand, CVD relies on chemical vapor precursors that are activated by heat or plasma to deposit atoms or molecules onto a substrate. This process enables the formation of compounds and can be carried out at temperatures compared to traditional thermal CVD (Donald M. Mattox). Variations such as Plasma Enhanced

CVD (PECVD) employ radio plasmas for deposition. Both PVD and CVD techniques are indispensable in industries like semiconductor manufacturing offering control over film thickness, composition and properties (Donald M. Mattox). These techniques have implications across fields, particularly in semiconductor technology where they facilitate the production of microelectronics and advanced coatings. PVD is highly adaptable when it comes to film thickness and can be applied to substrates of varying sizes and shapes. However, chemical vapor deposition (CVD) enables the application of compounds and polymers offering options, like PECVD for temperatures (Donald M. Mattox). These deposition techniques are crucial in creating materials and coatings with properties, which contribute to the progress of technology and applications, in industries (Donald M. Mattox).

2.2. Tungsten carbide (W-C)/Diamond like carbon (DLC) coatings – Tribological applications

DLC coatings have become a mainstay in the department of material science in various industries due to their set of properties. Because of their hardness, surface smoothness, chemically inert nature all along with low coefficient of friction make these coatings ideally suited for wear-resistant applications. Like every coin has two sides, these coatings also have their own fair share of incompetencies. One such negative aspect of these coatings is the high value of internal compressive strength and the lesser chemical interaction between films and their base metal which ultimately results in poor adhesion to the substrate. This places a very huge restriction on their commercial usage. As of today, it has been found out that using metal or silicon interlayers between the substrate and DLC solves the adhesion problem (C. Rincon , G. Zambrano , A. Carvajal , P. Prieto , H. Galindo , E. Martınez , A. Lousa , J. Esteve, 2001) .

One of the very popular techniques for the deposition of these coatings is magnetron sputtering. One major advantage of this technique is that it provides control over various parameters like deposition rate, temperature, and composition of the gas during the process. Generally speaking, multitarget sputtering systems are used to create multilayer films. A new technique was introduced in this study that uses a single sputtering target made of two equal parts—one half tungsten, the other half carbon to produce W–C and DLC multilayer coatings. The different layers are created without any breaks in the operation by varying the composition of the argon or methane sputtering gas. In order to increase the DLC protective coatings' adherence and wear resistance on steel substrates, multilayer coatings have been created using

this deposition technique. The coatings are composed of an upper DLC layer and a multilayer stack of various W–C layers (C. Rincon , G. Zambrano , A. Carvajal , P. Prieto , H. Galindo , E. Martınez , A. Lousa , J. Esteve, 2001).

The study (C. Rincon , G. Zambrano , A. Carvajal , P. Prieto , H. Galindo , E. Martınez , A. Lousa , J. Esteve, 2001) focused on the process of depositing and analyzing coatings with a focus on coatings made of tungsten carbide (WC) and diamond like carbon (DLC). For the deposition process, a radio frequency (RF) magnetron sputtering system operating at 13.56 MHz was used. The sputtering target consisted of tungsten (W) and carbon (C) bonded to a cooling plate. Coatings were applied onto silicon wafers and high-speed steel substrates positioned 6 cm below the target. Before introducing the gas, which was argon, the vacuum chamber was evacuated to a pressure of 10 Pa. The coatings were then deposited under conditions, including argon (Ar) and a mixture of methane (CH_4) and argon at varying substrate temperatures. In addition to that, various deposition conditions were employed to create coatings with structures and layers of DLC. Table 2.1 shows the different process parameters used in this case. (C. Rincon , G. Zambrano , A. Carvajal , P. Prieto , H. Galindo , E. Martınez , A. Lousa , J. Esteve, 2001).

Process	WC multilayer		Upper DLC
	A	B	C
Reactive sputtering gas	Pure Ar	20% CH_4/Ar mixture	40% CH_4/Ar mixture
Substrate temperature	500°C	500°C	150°C
Sputtering gas pressure	4 Pa	6 Pa	8 Pa
r.f. power	14 W/cm^2		
Target	W–C binary		
Substrates	M2 (AISI) high-speed steel, silicon		
Target-substrate distance	6 cm		

Table 2.1 Process parameters, C. Rincon et al.

Moreover, the analysis of these coatings involved techniques such as X ray diffraction (GIXRD) micro-Raman spectroscopy, scanning electron microscopy (SEM) transmission electron microscopy (TEM) and secondary ion mass spectrometry (SIMS). The films' ability to stick to the steel surface was assessed through a micro scratch technique while the behavior of friction and wear was examined using a ball, on disk micro tribometer under testing conditions (C. Rincon , G. Zambrano , A. Carvajal , P. Prieto , H. Galindo , E. Martınez , A. Lousa , J. Esteve, 2001). In general, this extensive experimental arrangement permitted the application and thorough examination of coatings and their characteristics such as adhesion, friction, and resistance to wear. This makes it highly valuable for research on materials and their applications in industries, like tool manufacturing and automobiles (C. Rincon , G. Zambrano , A. Carvajal , P. Prieto , H. Galindo , E. Martınez , A. Lousa , J. Esteve, 2001).

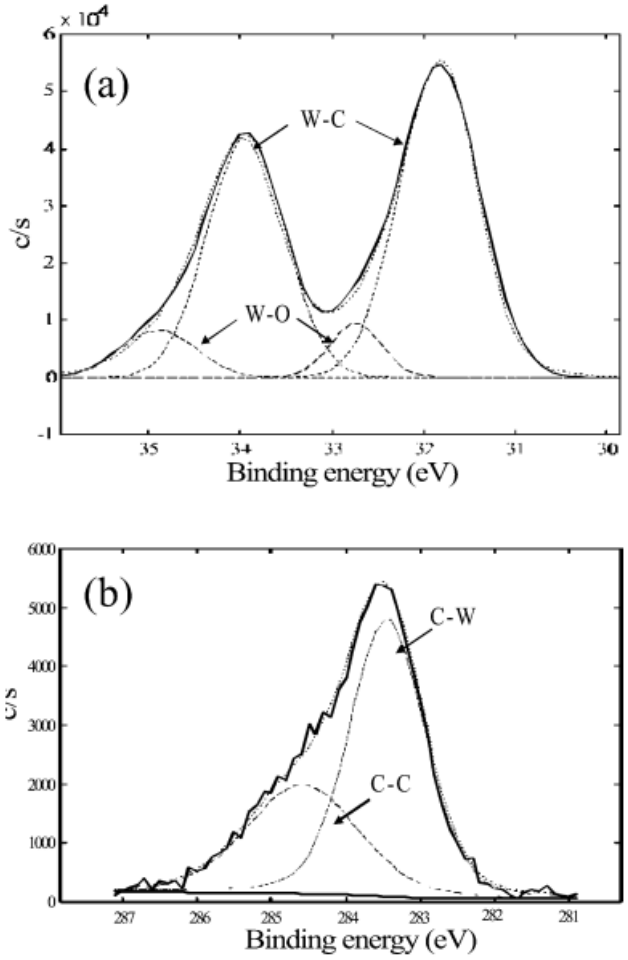

Figure 2.1 (a) Deconvoluted W & C (b) XPS spectra from 20 % of CH_4 in CH_4/Ar mixture

Insights into the composition and structure of the deposited coatings were obtained by the examination of GIXRD and XPS Raman spectroscopy. Through XPS analysis, the type B layer was found to include tungsten (W) mostly in the form of carbide (W C) with trace amounts of oxide (C. Rincon , G. Zambrano , A. Carvajal , P. Prieto , H. Galindo , E. Martınez , A. Lousa , J. Esteve, 2001). Figure 2.1 shows the XPS spectra. With 12% of the carbon bound as C-C, the examination of carbon (C) revealed the presence of C-W and C-C bonds, indicating a stoichiometry of $WC_{0.63}$. As opposed to this, the type A sample had an area-based connection that led to a low C-C bonding and a W-C stoichiometry of 0.40 (C. Rincon , G. Zambrano , A. Carvajal , P. Prieto , H. Galindo , E. Martınez , A. Lousa , J. Esteve, 2001). While there was no Raman signal found for the type A sample, micro-Raman spectra for the type B sample verified the presence of carbon bound as C. The grazing incidence XRD (GIXRD) patterns revealed that the two samples exhibited unique phase separations in their structures: the type A layer's hexagonal W-C formation and the type B layer's cubic sub-stoichiometric

phase WC_{1-x} (C. Rincon , G. Zambrano , A. Carvajal , P. Prieto , H. Galindo , E. Martınez , A. Lousa , J. Esteve, 2001). These results imply that procedures A, B, and C produce coatings that are, respectively, constituted of W-C phase, WC_{1-x} phase, and DLC phase. Consequently, they revealed details about the composition and structure of the materials involved (C. Rincon , G. Zambrano , A. Carvajal , P. Prieto , H. Galindo , E. Martınez , A. Lousa , J. Esteve, 2001).

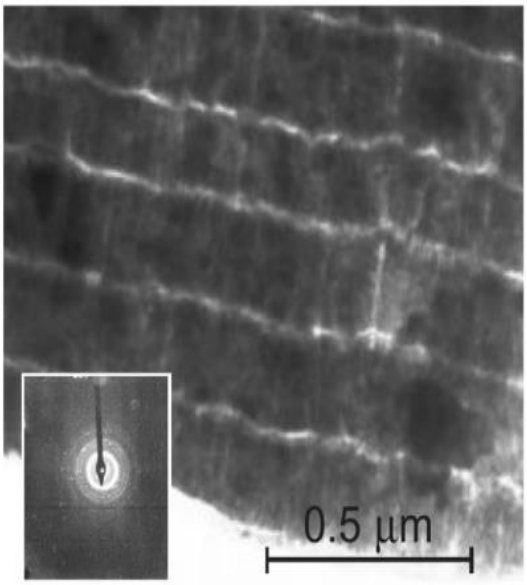

Figure 2.2 SEM multilayer

The experimental results also provided information about the W-C/DLC coatings. A layer of DLC and a thick columnar structure within the multilayer stack were seen when they were examined with a scanning electron microscope (SEM), Figure 2.2 (C. Rincon , G. Zambrano , A. Carvajal , P. Prieto , H. Galindo , E. Martınez , A. Lousa , J. Esteve, 2001). Still, more research was required to understand the stack's internal organization. The multilayer structure was recognized by transmission electron microscopy (TEM) examination Figure 2.3 (C. Rincon , G. Zambrano , A. Carvajal , P. Prieto , H. Galindo , E. Martınez , A. Lousa , J. Esteve, 2001), which revealed electron diffraction patterns suggesting the existence of a WC_{1-x} phase. It was interesting to note that the expected bilayer structure of W_2C/WC_{1-x} was absent, instead, WC_{1-x} layers and brilliant stripes were seen in interface regions rich in carbon (C. Rincon , G. Zambrano , A. Carvajal , P. Prieto , H. Galindo , E. Martınez , A. Lousa , J. Esteve, 2001).

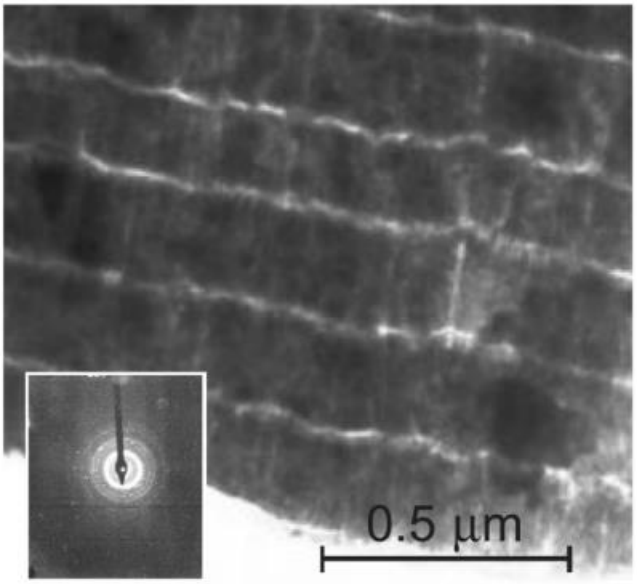

Figure 2.3 TEM multilayer

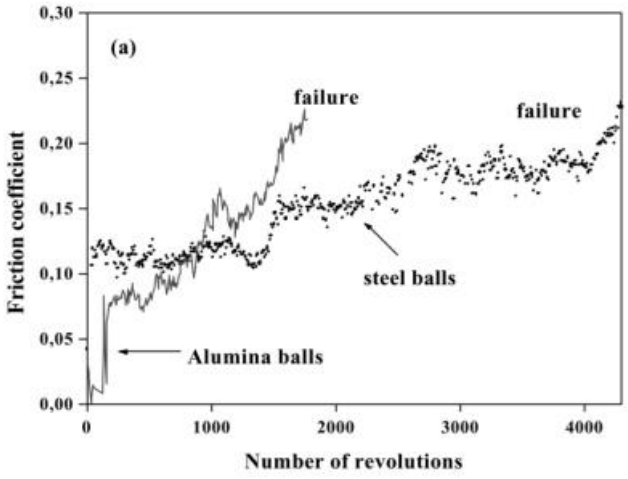

Figure 2.4 Evolution of the friction coefficient of a DLC multilayer

The multilayer coatings showed much better adherence in the scratch tests than the single layer DLC coatings. If single layer DLC coatings showed adhesion at 530 mN, the critical load values for multilayers were approximately 1300 mN (C. Rincon , G. Zambrano , A. Carvajal , P. Prieto , H. Galindo , E. Martınez , A. Lousa , J. Esteve, 2001). Ball on disc testing revealed that the friction coefficients of single DLC and multilayer coatings, Figure 2.4 were 0.12 on steel balls and 0.08 on alumina balls, respectively.

Compared to DLC coatings, multilayer coatings on steel substrates demonstrated notable durability and improved resistance to wear without sacrificing their friction qualities (C. Rincon , G. Zambrano , A. Carvajal , P. Prieto , H. Galindo , E. Martınez , A. Lousa , J. Esteve, 2001).

2.3. Corrosion resistance of tungsten carbide-rich/WCC coatings

Materials with strength and resistance to abrasive chemicals are in greater demand than ever before. This emphasizes the importance of materials, with a focus on WC coatings, such as TiN, Si3N4, SiC, ZrC, and WC. A number of techniques for applying these coatings are discussed, including plasma spraying, chemical vapor deposition (CVD), and physical vapor deposition (PVD), along with the drawbacks of each technique in terms of temperature and stress. To demonstrate how they can increase resistance against wear and corrosion, the application of ion irradiation based coating layer approaches is investigated. In the course of ion bombardment, equilibrium chemicals are formed by a process known as ion beam mixing, or IBM. Indicating possible improvements in chemical resistance, the study also emphasizes the creation of WC coating layers using noble gas ions. In order to design corrosion-resistant coatings, simulation is also applied to estimate element distribution and effective areal density. A study (A.S. Racz , Z. Kerner, M. Menyhard, 2022) is investigated here.

Carbon (C) and tungsten (W) layers were applied to a silicon single crystal substrate to create the structures used in this study. primarily three constructions, with different thicknesses and number of layers, called 102010, 1020, and 2020. Ions of Xenon (Xe+) or Argon (Ar+) at ambient temperature were utilized to create WC layers inside these structures. Considerable testing was also done to investigate circumstances by varying the fluence and ion energy levels (A.S. Racz , Z. Kerner, M. Menyhard, 2022).

Auger electron spectroscopy (AES) depth profiling, developed according to a protocol described in (A.S. Racz , Z. Kerner, M. Menyhard, 2022), was introduced to investigate the composition distributions following ion irradiation. Furthermore, tests were conducted in a sodium chloride solution to ascertain the samples' resistance to corrosion. The region's carbon layer had to be removed before the corrosion experiments, as described in (A.S. Racz , Z. Kerner, M. Menyhard, 2022), could be conducted. By employing a microwave plasma technique for oxidation, this was accomplished. Understanding the refabrication and analysis of WC rich layers within C/W multilayer structures, as reported in (A.S. Racz , Z. Kerner, M. Menyhard, 2022), was provided by this study.

Distribution and corrosion resistance can be better understood by combining ion irradiation, AES depth profiling, and TRIDYN simulation. The research has significant relevance for materials engineering and coatings applications, as indicated by the results of (A.S. Racz , Z. Kerner, M. Menyhard, 2022). The researchers' method gives them control over the WC layer's composition and development. Enhancing material durability and corrosion resistance is the primary goal, as these properties are essential for many technological applications. These analysis' detailed methods are available in (A.S. Racz , Z. Kerner, M. Menyhard, 2022).

A.S. Racz and colleagues investigated the formation and distribution of tungsten carbide (WC) rich layers in carbon/tungsten (C/W) multilayer structures by means of ion irradiation. Because of aberrations from ion mixing and compound creation at the interfaces, the researchers emphasized the significance of correcting depth profiles obtained using Auger electron spectroscopy, or AES (A.S. Racz , Z. Kerner, M. Menyhard, 2022). To highlight the difficulty in distinguishing extremely thin WC layers because of these artifacts, a master curve, Fig. 2.5, was created that shows the simulated amount of WC as a function of the WC layer thickness. The error caused by AES depth profiling stays within 10 15% with values leading to lower errors when the number of WC surpasses 400 per nanometers. The results show that the WC layer growth is dependent on initial layer configurations and ion bombardment circumstances. Through the utilization of irradiation conditions, they are able to effectively get a variety of distributions for WC carbides in three-layer structures, which are then put to the test for corrosion resistance (A.S. Racz , Z. Kerner, M. Menyhard, 2022).

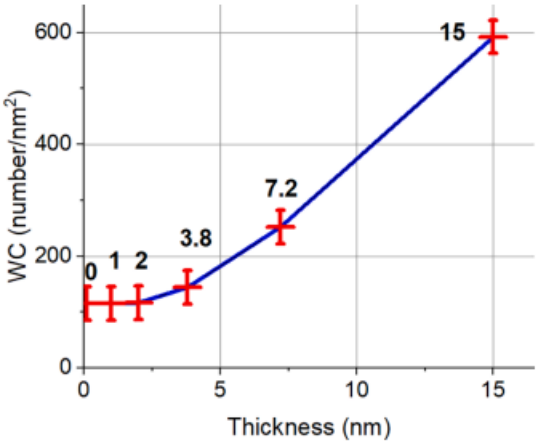

Figure 2.5 Master curve

Assessing the impact of potentiodynamic corrosion tests in a 3.5 weight percent NaCl solution on samples' corrosion resistance was the primary goal of the investigation

(A.S. Racz , Z. Kerner, M. Menyhard, 2022). The objective was to comprehend how these samples' corrosion resistance was affected by the tungsten carbide (WC) development brought about by ion irradiation under specific circumstances. Based on the areal density of WC, the study identified two zones of corrosion resistance by analyzing both low and high fluence ion irradiation scenarios involving Ar+ and Xe+ ions. This revealed a threshold for effective areal density and implied that structural modifications during WC layer formation contributed to improved corrosion resistance (A.S. Racz , Z. Kerner, M. Menyhard, 2022). The outstanding corrosion resistance of IBM-produced WC coatings, which surpasses that of alternative materials like commercially available cermet coatings, is highlighted by these data, which offer insights for coating design and optimization (A.S. Racz , Z. Kerner, M. Menyhard, 2022).

Sample & irradiation	Shape of WC distribution	WC effective areal density (numb/nm^2)	Corrosion current density, j_{corr} (μA/cm^2)
102010 1 × 10^{15} Ar^+/cm^2 40 keV		(169)	0.44
1020 3 × 10^{15} Ar^+/cm^2 80 keV		(247)	0.49
102010 3 × 10^{15} Ar^+/cm^2 40 keV		(248)	0.45
102010 1x10^{15} Xe^+/cm^2 120 keV		(282)	0.44
1020 3 × 10^{15} Ar^+/cm^2 50 keV		(289)	0.5
102010 2.5 × 10^{15} Xe^+/cm^2 40 keV		425	0.49
2020 6 × 10^{15} Ar^+/cm^2 110 keV		469	0.26
102010 1 × 10^{16} Ar^+/cm^2 40 keV		512	0.42
102010 2.5 × 10^{15} Xe^+/cm^2 120 keV		450	0.40
102010 3 × 10^{16} Xe^+/cm^2 120 keV*		1223	0.19
102010 5 × 10^{15} Xe^+/cm^2 120 keV		1407	0.09
102010 1 × 10^{16} Xe^+/cm^2 120 keV		1457	0.06
102010 3 × 10^{16} Ar^+/cm^2 40 keV		1567	0.13
1020 5 × $10^{15}$$Xe^+$/cm^2 160 keV		2370	0.06
1020 3 × 10^{16} Ar^+/cm^2 80 keV		2570	0.13
2020 3 × 10^{16} Ar^+/cm^2 keV		3408	0.05
2020 6 × 10^{16} Ar^+/cm^2 110 keV		3553	0.06

Table 2.2 The shapes of WC distributions, WC effective areal density & corrosion current densities, determined of various samples after the various IBM (first column).

The findings, which are shown in Table 2.2 and Figures 2.6 & 2.7, provide insight into the information gleaned from corrosion testing about corrosion resistance (A.S. Racz , Z. Kerner, M. Menyhard, 2022). AES depth profiles taken during the corrosion tests that contrast low and high fluence ion irradiation conditions are shown in Figure 2.6 (A.S. Racz , Z. Kerner, M. Menyhard, 2022). The effective areal density of WC plays a crucial role in determining corrosion resistance, as seen by the differentiation between the corrosion resistance data in Figure 2.7's two regions (A.S. Racz , Z. Kerner, M. Menyhard, 2022).

The morphologies of the corrosion current densities and effective areal densities of WC distributions are summarized in Table 2.2 (A.S. Racz , Z. Kerner, M. Menyhard, 2022). This synopsis aids in demonstrating the relationship between the structural changes brought about by the creation of WC layers and the enhanced corrosion resistance that

follows. Additionally, a significant idea presented is density, which is essential in determining corrosion resistance. The relationship between corrosion current density and density effective areal density for sample 102010, which was exposed to 120 keV Xe+ irradiation, is shown in Figure 10 (A.S. Racz , Z. Kerner, M. Menyhard, 2022). The study demonstrates how corrosion resistance changes when an areal density threshold is attained. This shift is explained by the percolation behavior associated with defects and the presence of W (tungsten) atoms in the solute metal (A.S. Racz , Z. Kerner, M. Menyhard, 2022).

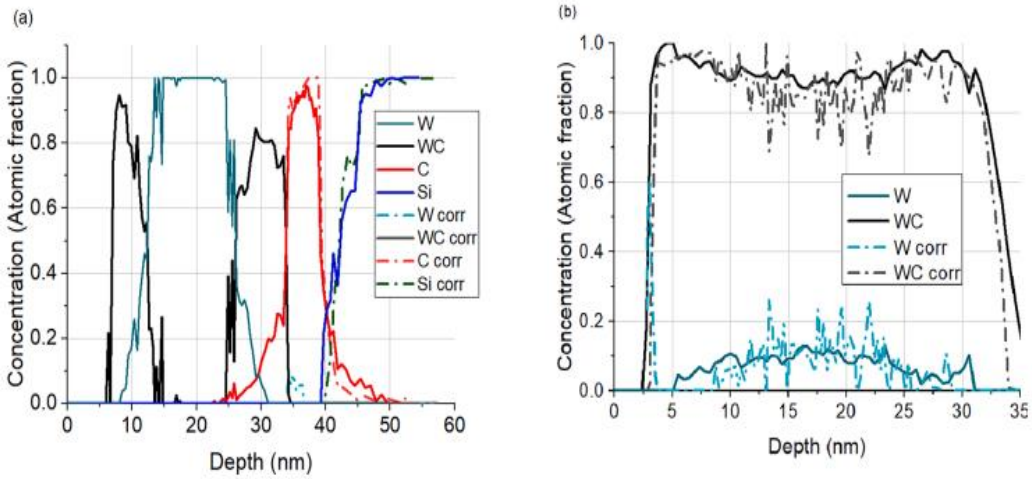

Figure 2.6 AES depth profiles measured before & after the potentiodynamic test of sample 102010 irradiated by (a) Ar+ 40 kev 3 * 10^15 / cm^2 (b) Xe+ 120 kev 5 * 10^15 cm^2.

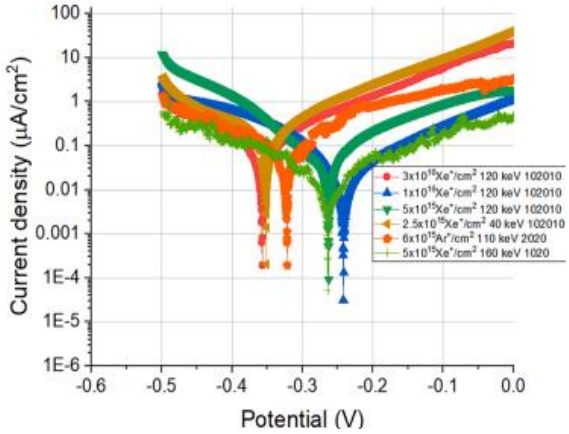

Figure 2.7 Polarization curves obtained for some of the irradiated samples.

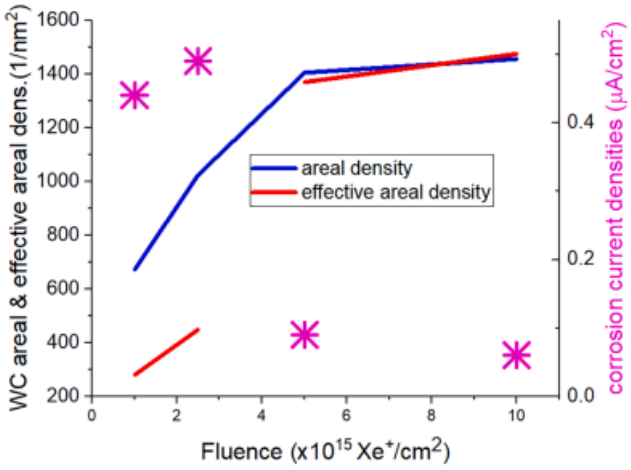

Figure 2.8 Areal density, effective areal density, and corrosion current density vs the irradiation fluence curves. Sample 102010; irradiation Xe+ 120 keV.

This analysis also draws comparisons between IBM-produced WC coatings and other materials, including a commercially available cermet coating, to illustrate the corrosion resistance of the former (A.S. Racz , Z. Kerner, M. Menyhard, 2022). The collective results of this research provide valuable understanding of coatings engineering and design. Within corrosive conditions, they demonstrate the performance of IBM-produced WC coatings and specifically highlight the impact structural changes play in improving corrosion resistance.

In short, the study (A.S. Racz , Z. Kerner, M. Menyhard, 2022) found out that tungsten carbide (WC) was formed when C/W structures were exposed to argon and xenon ions. The layers' structure and the irradiation circumstances affected the amount of WC that generated. The research also determined the connection between corrosion current and WC density to assess corrosion resistance, alongside a correlation between corrosion resistance and WC density. With the use of TRIDYN simulation, (A.S. Racz , Z. Kerner, M. Menyhard, 2022) was able to create specialized coatings with WC concentration.

3 Electroless Nickel plating – a theoretical study

When it comes to producing alloy coatings, electroless deposition is one of the most refined techniques. In order to produce binary, tertiary, or even quaternary alloys, the technique entails the autocatalytic reduction of cations by electrons released from suitable chemical reducing agents at the substrate/solution interface. Additionally, a significant degree of elemental release from these agents allows co-deposition with the reduced metal. The technique works well because it gives the producer the ability to regulate the reducing agent's relative strength when ligand-stabilized metal complexes are present, resulting in the production of alloys with varying composition. Not only can coatings be produced in homogeneous or microcrystalline non-equilibrium states using the electroless deposition technique, but heat treatment after deposition can be used to successfully produce the more commonly recognized equilibrium phases, expanding the range of properties that can be achieved and, consequently, the applications that the technique can be applied to. Reviewing the nickel-phosphorus (NEP) system, which accounts for the great bulk of electroless deposition applicable to the industrial sector globally, this chapter focuses primarily on the use of this binary alloy in coating technology.

3.1. The Nickel-phosphorous system

The process of depositing nickel ions on surfaces that are catalytically active using hypophosphite in a solution is mainly based on three reactions (P Gillespie). The reactions represent the process for nickel deposition happening at a pace and the deposition of phosphorous. The former increases the acidity of the solution while the latter contributes to forming surface deposits in nickel and orthophosphite ions. Adjusting conditions such as pH levels and concentrations of reducing agents and complexing agents allows control over the rates of these reactions enabling the production of coatings with chemical compositions and properties. For information on factors influencing deposition rate and coating composition, Mallorys monograph (P Gillespie) is an excellent resource. Additionally, the following sections provide insights into kinetics, mechanisms and practical considerations related to co deposition of nickel and phosphorus. To sum up, it is very important to manage rates

between nickel and phosphorus deposition reactions for tailoring coatings to requirements.

3.2. The Ni-P kinetics

Several studies have explored the factors that affect the deposition rate of Ni-P coatings, temperature and pH. These studies have also examined factors such, as the production of by products like hypophosphite and the esterification of complexing ligands (P Gillespie). Extensive research conducted by Mallory has shown that specific yet encountered conditions can establish rate laws to describe the kinetics of deposition (P Gillespie). When the solution is properly buffered to prevent acid catalyzed esterification, ligand concentrations are not significantly higher than metal ion concentration and when hyperphosphate ion buildup is minimal, a general empirical rate law can be derived. This rate law encompasses coefficients representing the order of deposition rate concerning ions, nickel ions and acid concentrations well as activation energy, rate constant and temperature.

Furthermore, simplifying the description of kinetics is made easier by observations that reveal reaction orders for chelating systems with matching coordination numbers and annular sizes. For dentate five membered ring complexes formed from ligands such as glycollate, lactate and aminoacetic anions, reaction kinetics consistently follow a similar pattern. This empirical behavior is defined by values, for the reaction orders concerning the ion, nickel ion and acid concentrations. Activation energies display some diversity among these systems ranging from 17 to 23 k cal g mol^{-1} while rate constant k demonstrate variability based on the stability constants between the metal/metal ligand complexes of the system being investigated.

3.3. The Ni-P mechanisms

Although there are many methods for the nickel deposition process, the nickel phosphorus (Ni-P) deposition process focusing on two routes is highlighted here. The first proposed route, called the hydride mechanism starts with the removal of hydrogen, from ions at the surface of the substrate. This leads to the creation of ions that play a role in reducing nickel ions present in the solution (P Gillespie). As a result, a metallic surface deposit is formed while hydrogen gas is released. This mechanism also suggests that an intermediate substance like meta phosphorus acid exists, which undergoes reduction by ions to produce phosphorus metal and release hydrogen gas

(P Gillespie). This mechanism provides insights into the chemical reactions involved in Ni-P deposition.

The second proposed route, known as the Gutzeit mechanism, hypothesizes that atomic hydrogen is primarily responsible for driving the nickel deposition reaction (P Gillespie). It begins with oxidation of ions at the substrate surface leading to the formation of radicals that subsequently reduce nickel ions and form a surface deposit of nickel. Additionally, some hypophosphite ions are believed to be reduced by hydrogen resulting in phosphorus metal being deposited on the surface. This mechanism also accounts for a portion of ions undergoing surface oxidation and liberating hydrogen gas. These pathways based on mechanisms offer understanding into the kinetics and reactions implicated in the formation of Ni-P coatings (P Gillespie).

3.4. Factors & conditions for the deposition process

There are various factors associated with the process of depositing nickel phosphorus (Ni-P) coatings using electroless deposition. Alongside with the factors, there are several conditions that influence the composition and properties of these coatings. Firstly, electroless Ni-P deposits are not solely made up of metal but also contain elements from the reducing agents, which can be advantageous for customizing properties (P Gillespie). The significance of conditions and the need to find a balance between factors in order to achieve desired coating properties should not be neglected. The ratio of nickel ions to phosphorus containing reducing agents has an impact on the composition of the coating with recommended ratios ranging from 0.30 to 0.45 for controlling phosphorus content (P Gillespie). The selection of bath components, such as nickel salts and hypophosphite ions should also be considered, taking into account of the factors as well as their availability.

Furthermore, complexing agents play a role in stabilizing the bath. Must be carefully chosen with an appropriate ligand strength to maintain a deposition rate that is feasible for experimentation. These stabilizers prevent alloy deposition on vessel walls and can improve the brightness of coatings. however, caution should be exercised due to interactions, with the deposition process. Another 2 important factors are acidity (pH) and temperature and their effects on deposition rates. It was seen that lower pH values resulted in reactions while higher pH values led to undesired surface defects (P Gillespie).

In short, the importance of maintaining an equilibrium, between factors and conditions in order to create electroless Ni-P coatings with desired characteristics is

very much needed. This also takes into account aspects such as composition, bath components and control over pH and temperature. These insights are crucial, for optimizing the deposition process in a range of applications (P Gillespie).

3.5. Structure & composition of Ni-P alloys – Phases

Classic diagrams, in the field of materials science have been established for a time based on experiments with alloys that are slowly solidified from the state. These alloys are usually made by combining elements to create phases that're in thermodynamic equilibrium. One example of such a diagram is the nickel phosphorus (Ni-P) system, which was first developed by Konstantinov in 1908 and has since been modified by researchers like Hansen and Metcalfe (P Gillespie). This diagram provides information about the Ni region, including the first eutectic point points where compounds like Ni_3P, NLP_2 and Ni_2P form as well as a small region called the Alpha nickel phase where solid solutions can be found. This diagram has historically been used as a reference for understanding Ni-P alloys (P Gillespie).

However, research conducted over the fifteen years on deposition of Ni-P coatings has shown that these coatings often exhibit properties that do not align with what is predicted by the traditional phase diagram. Detailed studies have revealed the presence of equilibrium phases and structures in these coatings when they are initially deposited. These structures include deposits with microcrystalline characteristics, amorphous phases, and small crystallites. These discoveries challenge the general understanding of thermodynamics thus giving a more specific perspective on this system (P Gillespie).

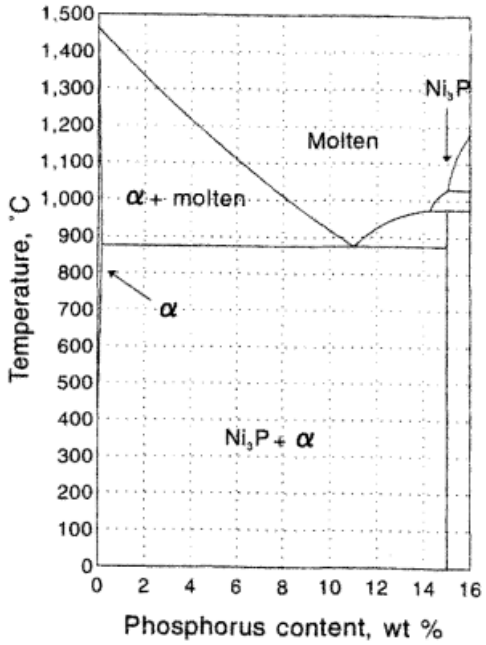

Figure 3.1 Phase diagram for Ni-P alloy

A significant advancement in understanding the complexities of Ni-P coatings comes from the research conducted by Duncan. He introduced a diagram that compares results from studies on electroless coatings with the traditional phase diagram (P Gillespie). This diagram provides insights into the structure of deposited electroless alloys revealing two phases known as β and γ. It also predicts temperature and compositional ranges for phase transitions from β to alpha and γ to Ni_3P contributing to an understanding of the relationships within the Ni-P system (P Gillespie).

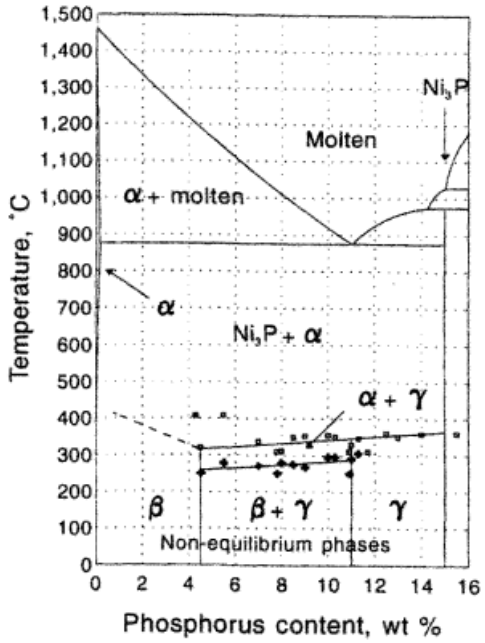

Figure 3.2 Phase diagram for electroless nickel deposits.

The presence of equilibrium metastable phases greatly influences the chemical, physical and tribological properties of electroless coatings (P Gillespie). These unique phases are often preferentially formed during deposition shaping the characteristics of Ni-P coatings (P Gillespie). Consequently, controlling and manipulating these phases through treatment is crucial in fine tuning the final properties of these coatings.

3.6. Physical properties of Ni-P coatings

Ni-P coatings have a range of properties that make them versatile for applications in different industries. The hardness, wear resistance, and corrosion protection of these coatings are influenced by their composition and how they are treated with heat. Coatings with low phosphorus content (1 wt % P) mainly composed of the ß phase exhibit hardness (P Gillespie). On the other hand, medium phosphorus coatings (3.0 9.0 wt % P) containing a mix of ß and α phases strike a balance between properties. High phosphorus coatings (9.0 13.0 wt % P) composed entirely of the γ phase are relatively softer (P Gillespie). The hardness of these coatings can be further modified through heat treatment techniques. The wear resistance is closely linked to the composition with two medium phosphorus coatings offering protection against abrasion. Corrosion protection depends on factors such as coating porosity and chemical inertness making high phosphorus coatings more favorable in this aspect.

	Phosphorus content		
	Low (1.0–3.0 %)	Medium (3.0–9.0 %)	High (9.0–13.0 % P)
As-plated	728–802 β	513–527 β+γ	517–531 γ
250°C	728–838 β	612–643 β+γ	560–572 γ
300°C	795–877 β	872–918 α+γ	870–918 γ
350°C	980–985 $Ni_3P + \alpha$	862–952 $Ni_3P + \alpha$	856–977 γ
400°C	927–987 $Ni_3P + \alpha$	834–897 $Ni_3P + \alpha$	866–987 $Ni_3P + \alpha$
450°C	854–860 $Ni_3P + \alpha$	800–934 $Ni_3P + \alpha$	811–894 $Ni_3P + \alpha$

Table 3.1 Knopp hardness of Ni-P alloys before & after heat treatment

Besides composition and treatment methods, stress levels and magnetic behavior also play roles in determining the suitability of Ni-P coatings for applications. Coatings containing 3.6-10.4 wt % phosphorus experience tensile stress which can impact their fatigue life span negatively (P Gillespie). In contrast, pure phase coatings exhibit stress that enhances their fatigue life expectancy. The magnetic properties of Ni-P coatings change as the phosphorus content varies, i.e., high phosphorus coatings become nonmagnetic compared to others (P Gillespie).

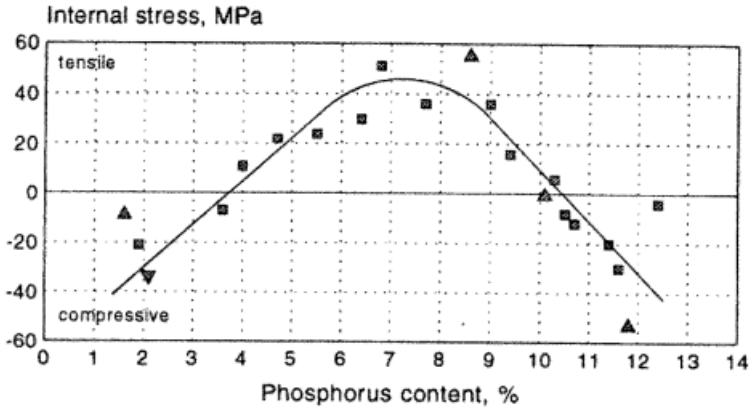

Figure 3.3 Effect of phosphorous on internal stress

Medium phosphorus coatings can have increased coercivity when subjected to heat treatment processes. In brief, coatings made of nickel phosphorus (Ni—P) possess a range of properties, which allow them to be versatile in meeting industrial and engineering needs (P Gillespie).

Composition	Structure	Coersivity (Oe)
3.0–6.0	High β content	80–20
7.0–9.0	(β + γ)	1–2
11.0	Pure γ	0

Table 3.2 Magnetic properties of Ni-P alloys

3.7. Electroless nickel plating on sintered iron parts

Despite its use there are still challenges associated with the electroless nickel plating process that researchers continue to investigate in order to improve its efficiency. We have chosen sintered pulleys for the nickel coating process because pulleys will be subjected to performance tests (which is explained in detail in chapter 5.1). So, considering this, an experimental study (L. M. Apininskaya; I. D. Radomysel'skii, 1965) focussed on the electroless nickel plating on sintered iron parts is observed in the following section.

The focus of this study (L. M. Apininskaya; I. D. Radomysel'skii, 1965) revolves around expanding the application of electroless nickel plating to sintered iron base parts. These parts have a very high level of porosity and possess complex challenges during the coating process. It also emphasizes the importance of protecting both the outer surfaces of these parts from corrosion setting the groundwork for the objectives of this study (L. M. Apininskaya; I. D. Radomysel'skii, 1965).

Digging into the principles behind nickel plating, nickel ions are reduced from solutions containing nickel salts using hypophosphites. This reduction process is catalyzed by metals belonging to group VIII, in the periodic table. During deposition atomic hydrogen and phosphorus are formed. The detailed chemical scheme provided offers insights into the steps involved in nickel plating and enhances our understanding of its underlying mechanisms (L. M. Apininskaya; I. D. Radomysel'skii, 1965). The study thoroughly explores the challenges faced when electroless nickel plating iron specimens. It notes that alkaline solutions are not suitable due to the low corrosion resistance of coatings produced in environments. Instead, solvents or cold degreasing solutions for degreasing before the nickel-plating process are adopted. The choice of sintered materials for coating, such as 100% iron, iron with 1% graphite and iron with 1% graphite and 2.5% copper is strategically made based on their usage in constructing parts (L. M. Apininskaya; I. D. Radomysel'skii, 1965).

Moving on to the phase the study rigorously tests acid nickel-plating solutions to determine the optimal composition for effectively coating sintered parts (L. M. Apininskaya; I. D. Radomysel'skii, 1965). The researchers carefully select a

combination of nickel sulfate, sodium hypophosphite, sodium acetate and sodium citrate concentrations along with defined pH range and temperature conditions. This thorough selection process adds complexity to the investigation as it involves examining corrosion resistance of deposits developing a two stage electroless nickel plating process and addressing challenges related to solution correction. The study also delves into detail about the tackled difficulties in correcting the solution by focusing on issues related to the formation and precipitation of nickel phosphite (L. M. Apininskaya; I. D. Radomysel'skii, 1965). The analysis focuses on the examination of the effectiveness of complex forming agents, such, as ammonium fluoride, sodium citrate, thiourea, magnesium sulfate and glycocoll. The findings suggest that using a combination of sodium citrate and glycocoll in solutions can effectively prevent precipitation of nickel phosphite and ensure operation (L. M. Apininskaya; I. D. Radomysel'skii, 1965) .

To address corrosion problems in sintered parts, a solution containing a volatile phosphate inhibitor called GKZh 94 is used for impregnation (L. M. Apininskaya; I. D. Radomysel'skii, 1965). The mechanism behind this substances ability to make surfaces hydrophobic is explained in detail, including the formation of polymer films during reactions with surface moisture. This impregnation process is crucial for preventing the infiltration of nickel-plating solution into pores and causing corrosion. In order to further enhance surface corrosion resistance, additional steps are introduced (L. M. Apininskaya; I. D. Radomysel'skii, 1965). These include treating the parts with a GKZh 94 solution and polymerization. Comparative corrosion tests provide evidence that these measures significantly improve the properties of nickel phosphorus deposits.

A comprehensive guide is provided for electroless nickel plating, on parts made using the powder metallurgy method (L. M. Apininskaya; I. D. Radomysel'skii, 1965). Each step from plating part preparation to electroless nickel plating stages is thoroughly outlined. The proposed process provides information, about the composition of the solution, pH levels, temperatures and holding times. The attention to detail highlights the thoroughness of the process. Additionally, microsections and photomicrographs are included to demonstrate how well the procedure works by depositing a layer of nickel above the pores, which is filled with polymerized hydropolysiloxane (GKZh 94) (L. M. Apininskaya; I. D. Radomysel'skii, 1965).

To summarize, scientific principles, experimental methods, and technological specifications related to electroless nickel-plating on porous iron parts were discussed briefly . Each challenge is carefully addressed, showcasing an understanding of the complexities involved in achieving corrosion resistance and pleasing nickel phosphorus deposits on sintered constructional iron base parts.

4 Hazardous effects of hard chrome plating

Hard chrome plating procedures release fumes that not only harm the environment but also pose risks to workers' health. People can be exposed to these emissions by inhaling fumes, consuming water or having direct skin contact with the plating solutions. Various research studies (R. A. Lane, C. Fink, C. Grethlein and N. Rome, Sept. 2012) suggest that such exposure increases the likelihood of health problems, including lung cancer, skin issues and birth defects. In 2006, a regulation highlighted hexavalent chromium (Cr(VI)) as a factor for 10 to 45 cases of cancer per 1000 workers comparing it to hazardous substances like asbestos and benzene, Fig.4.1 (R. A. Lane, C. Fink, C. Grethlein and N. Rome, Sept. 2012). To address these health risks, the Occupational Safety and Health Administration (OSHA) proposed a reduction in the exposure level for CrVI from 52µg/m3, to 5µg/m3 in 2006, Fig.4.2 (R. A. Lane, C. Fink, C. Grethlein and N. Rome, Sept. 2012). Moreover, electroplating processes involving chrome and nickel have been linked to asthma.

Material	Cancer Risk (per 1000)	Rulemaking Date
Asbestos	6.7	June 1986
Benzene	10	September 1987
Formaldehyde	0.0056 - 2.64	December 1987
Cadmium	3 - 15	September 1992
1,3 - Butadiene	1.3 - 8.1	November 1996
Methylene Chloride	3.6	January 1997
CrVI	10 - 45	February 2006

Figure 4.1 Cancer risk of Cr (VI) compared to other known carcinogens.

Country	Occupational Exposure Limit (µg/m³)
United States • New OSHA (2006) • Previous OSHA	 5 52
European Union, France, Germany, UK, Finland, China, India, Japan	50
Sweden	20
Denmark	5

Figure 4.2 Cr (VI) - occupational exposure limit

4.1. Known alternatives

It is a well known fact that corrosion protection and wear and tear are some of the main aspects of metal coating techniques. For the automotive sector, it is very important that the metal components should have these qualities in abundance. It is because of this, Cr (VI) are still available in the market.

By substituting platinum for lead in plating anodes, changing the plating bath composition, and installing more effective wastewater treatment systems, several producers have reduced the negative consequences of coating operations. Regrettably, higher production costs are the result of these and other actions. Alternative coating methods have therefore been investigated that offer the same or comparable performance qualities, cost, and appearance attributes. Among these developments are the applications of trivalent chromium, nickel–tungsten nanocrystalline structures, high velocity oxyfuel (HVOF) , and photovoltaic diode (PVD) (K. Legg, M. Graham, P. Chang, F. Rastagar, A. Gonzales and B. Sartwell, May 1996). Commercial substitutes for electrolytic hard chrome procedures that are competitive in terms of cost and performance are presented in Figure 4.3 (K. Legg, M. Graham, P. Chang, F. Rastagar, A. Gonzales and B. Sartwell, May 1996).

Technology	Coating material	Typical component application	Typical purpose	Comments
HVOF	Cr_3C_2/Mo-Ni-Cr	Piston Rings	Wear	OEM only
HVOF	Tribaloy 400, WC-Co	Turbine Shafts, Al bearing surfaces	Fretting, wear, corrosion, hot oxidation	OEM and rebuild
Sputter PVD	CrN, Ti-Al-N, TiN	Hydraulic shafts, molds, pump parts, gears, bearings	Wear, release, erosion, corrosion, decorative	OEM; cannot be thick enough for rebuild. No refinishing needed
Plasma nitride + PVD	CrN, Ti-Al-N	"Soft" steels, hydraulics, molds, shafts, piston rings	Wear, fretting, corrosion, erosion	For relatively soft steel, perhaps Al. No refinishing needed
Arc PVD (thick coating)	CrN, Ti-Al-N	"Soft" steels, hydraulics, shafts	Wear, fretting, corrosion, erosion	For extended wear life, perhaps light rebuild
Laser Cladding	Tribaloy 400, WC-Co	Bearing surfaces, turbine blades, shafts	Wear, fretting, corrosion, erosion	High local temperatures, good metallurgical bond. Must be refinished
Laser CVD	TiN	Bearing surfaces, shafts	OEM, rebuild, wear, fretting	High local temperatures. No refinishing needed.

Figure 4.3 Alternative coating technologies

5 Process flow of experiments and technical data of coatings

The aim of the research was to create a procedure for characterizing:

- an unknown coating (or treatment) applied on wear resistant parts found in the market and used by the competitors.
- Or a well-known coating applied on the parts provided by CRF to evaluate the main characteristics before starting the test activity on bench and / on-vehicle i.e., more expensive and require many resources (persons, time, equipment.).

5.1. Selection of base materials

For the electroless nickel plating, pulleys made with sintered base material (Sintered iron matrix that contains copper) have been used. The pulleys have been obtained by two different processes. Process 1 and process 2. The main difference between the two steps is the presence of sand blasting. In the automotive industry, these coated pulleys are used on engine timing belts. Pulleys are generally subjected to bench tests. Currently, the following pulleys are in production:

- Hard chrome plated pulleys
- Pulleys in Current production – steam treatment.
- Electroless nickel plated pulleys without heat treatment and with heat treatment
- With sandblasting or without sand blasting for improving adhesion.

The reason why pulleys are selected is because they will be subjected to bench tests. So, they needed to be characterized for classifying the different coatings and treatment. The main supplier of the pulley for the analysis was GKN. The plator is Gruppo Gaser and the chemical producer is Tecnochimica. Other features of the pulleys are steam treatment has been done at 560 degrees at high pressure. It is also used to remove oil. This is applied by the supplier of the pulley. Sand blasting is done to remove the oxide layer created with heat treatment because this may have a bad influence on the adhesion of Ni-p alloys.

Moving on to the selection of the base material for hexavalent chromium, a shock absorber rod was considered. The material used for the rod was EN 10277-5 grade cold drawn with a surface hardening of EHT 75 HRA. A cylindrical rod was chosen because to carry out the polishing process easily for better corrosion and wear resistance. Similarly, a cylindrical rod was chosen as the base material for trivalent chromium with a base material of CK45 non-hardened. The Cr (VI) rod was supplied by Magneti Marelli. The trivalent rod and coating were done by Macdermid Enthone at their R&D facility in Germany. So, generally its easier to carry out this kind of post treatment on cylindrical or spherical parts. For the PVD coatings, a very thin rectangular sheet of Ferritic steel of the grade AISI 430 was chosen as the base material. This was chosen as the base material because of its excellent corrosion resistance. By selecting such a material, the corrosion resistance of the coating itself (standalone) could be evaluated. The PVD coatings were done by STS group. The 430-steel surface is bright-annealed.

This research is mainly a validation of procedure (a preliminary characterization for bench and performance tests) for wear resistant coatings. It mainly consists of the following:

1. Physical/chemical characterization of coatings (visual inspection, microscopic analysis, elemental composition, thickness, microhardness, corrosion)
2. Bench test for evaluating the performances of the components (wear resistance, fatigue, abrasion resistance.
3. On vehicle tests for evaluating the performance of the components assembled on the car (position in contact with other parts – environmental condition that cannot be replicated in the laboratory).

The following table displays in short, the list of experiments and base materials adopted for the research.

General list of experiments	**Specimen used (base material)**
Microscopic (SEM & Optical with thickness measurement) analysis, Hardness test (Vicker's test), Neutral salt spray test (Corrosion).	Cr (VI) – EN 10277-5 grade cold-drawn EHT 75 HRA – Cylindrical rod
	Cr (III) – CK 45 non-hardened – Cylindrical rod
	PVD (DLC, CrN, WC) coatings – Ferritic steel AISI 430 – Rectangular thin sheet
	Electroless nickel – sintered material with pores - pulleys

Table 5.1 List of techniques & base materials chosen.

A general process flow of the experiments adopted for this research is shown in figure 5.1.

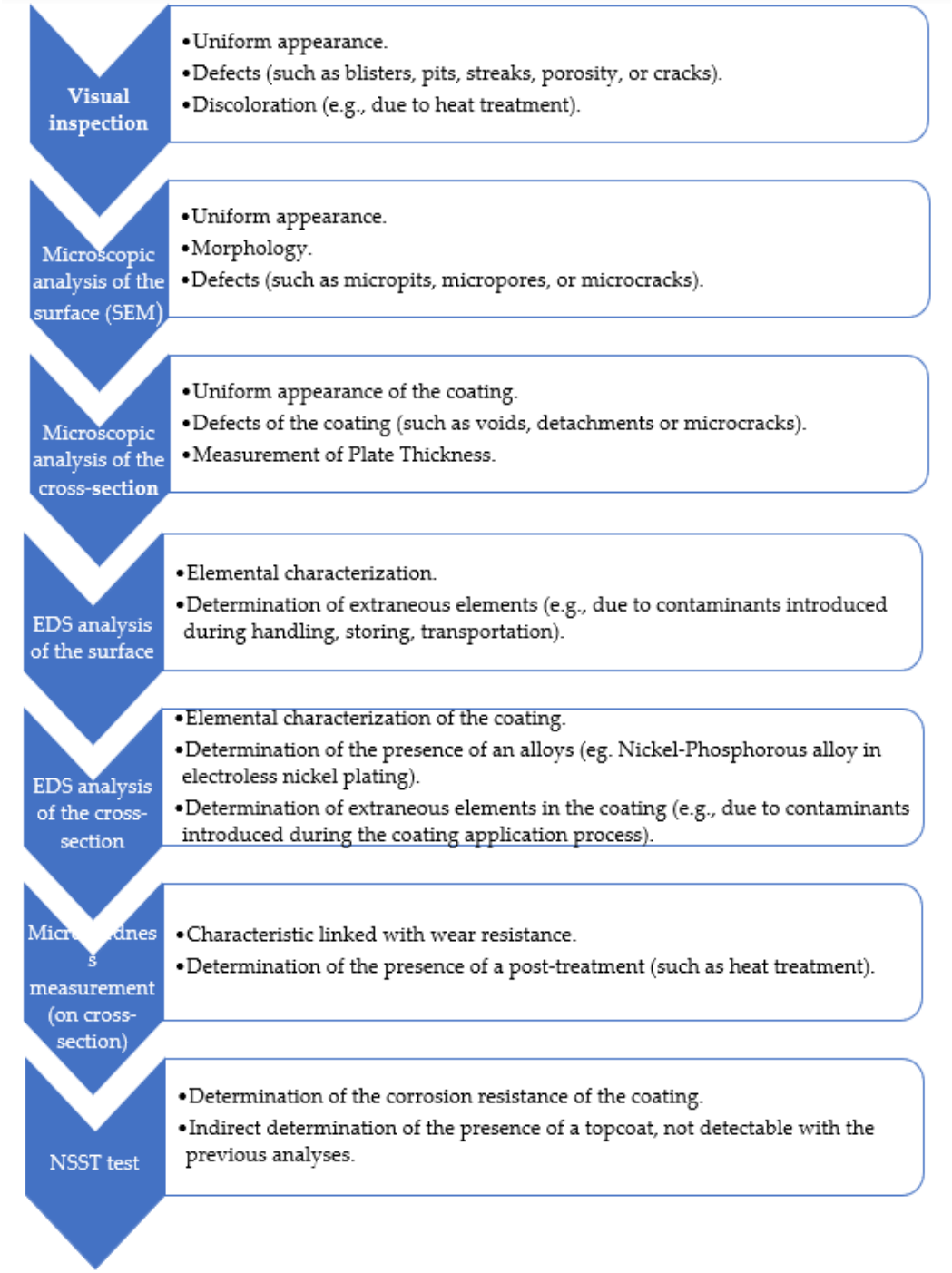

Figure 5.1 Process flow of experiments.

*EDS: Energy-Dispersive X-ray Spectroscopy, *NSST: Neutral Salt Spray Test

In the following section, the different process parameters used for the hard chrome coating process are discussed.

Step 1 - Metal Cleaning

Process parameters:

- Temperature
- Concentration
- Time
- Agitation
- Solution level

Step 2 - Water rinse

Step 3 - Mechanical Preparation

3A) Polishing / Buffing

Process parameters:

- Wheel speed
- Buffing wheel material
- Buffing wheel compound

3B) Abrasive blast process

Process parameters:

- Media type
- Blasting media size
- Blasting media flow or nozzle air pressure
- Dwell time
- Abrasive media level

Step 4 Acid Activation

- Concentration
- Time
- Agitation
- Current / Voltage
- Solution level

Step 5 - Chrome Plate

Process parameters:

- Temperature
- Concentration
- Metallic impurity concentration

- Time
- Agitation
- Current / Voltage
- Solution level

Step 6 - Water rinse

5.1.1. Hexavalent chromium (Cr (VI)) -Technical data

It is possible to plate almost any known type of material to any given thickness using the non-flouride, fast-chromium hexavalent chromium coating process used in this analysis. The coating can be used with lead or platinum plated titanium anodes. Its field of application is very broad, ranging from hydraulic components, wear and tear motor articles, down to printing rollers.. Since the coating does not contain any flourides, the etching effect on base material is kept to a minimum. The coating used is very economical due to its high deposition rate. The process itself is very efficient and easily done.

The coating also boasts exceptional wear resistance and tear alongside a minimum 1000 HV 0.1 hardness. Another feature of the coating is that micro-cracks can be found in the coating. In order to obtain good corrosion resistance, the electrolyte used should meet certain criteria. Through the whole current density range, the coating deposits are bright. The following tables show the operating parameters and other properties associated with the undertaken coating (Technical_Data_Sheet_Hexavalent_chrome).

Parameter	Range
Chromic acid	180 - 350 g/L
Sulfuric acid In relation to chromic acid concentration	1.1% - 1.8%
Density with new bath 300 g/L chromic acid	Minimum 1.215 g/cm³
Temperature	52 - 65 °C
Cathodic current density	10 - 100 A/dm²
Anodic current density	5 - 30 A/dm²

Table 5.2 Parameters - Hexavalent chrome coating

5.1.2. Trivalent Chromium (Cr (III)) – Technical data

An electrolyte based on trivalent chromium facilitated the production of hard chrome deposits during the coating process. The bath environment is then totally cleared of hexavalent chromium.

The table 5.3 shows the operating parameters for the trivalent chromium used (Technical_Data_Sheet_trivalent_chrome).

Parameters		Range
Trivalent chrome source		635 – 750 g/L
Complexing agents for the chrome source		225 – 265 g/L
Expresed as Cr		18,0 – 21,2 g/L
pH		5,0 – 5,5
Density at 20 C		1,15 – 1,20
Agitation		With pump
Current density	Cathode	40 – 50 A/dm²
	Anode	30 – 40 A/dm²
Temperature		50 – 60 °C

Table 5.3 Operating parameters - Trivalent chromium

5.2. CVD & PVD coatings

5.2.1. Diamond like Carbon (DLC) coatings – Technical data

Physical vapor deposition (PVD) and plasma-assisted chemical vapor deposition (PACVD) are two other alternative coating technologies to the typical hard chromium plating that we have seen in the earlier section. The temperatures at which these processes are carried out ranges from 180°C to 450°C, high vacuum (p=0.00005 mbar). Ceramic materials such as titanium nitrides, binitrides, carbonitrides, titanium aluminum and chromium, and in the case of DLC, just Carbon, are used to manufacture coatings of various kinds.

In specific terms, the properties of DLC coatings are excellent toughness and durability against rust and wear (over According to ASTM B117-07a, 1500 hours on titanium),

low comfortable look, asepticity, and friction coefficient. The following industries employ the parts that are typically coated; cars, watches, medical, optical, racing, and plastic molding, or mechanics in general.

These parts' constituent materials include titanium and its alloys, as well as various steels, copper, and aluminum alloys, each of which is supported by a distinct surface treatment (generally galvanic and nickel plating). A first layer of CrN and a second layer of C-based coating are visible when DLC is deposited at a temperature of 200°C. One coating that complies with ISO 10993 standards is DLC; this standard states that DLC is biocompatible and does not exhibit cytotoxicity, skin irritation, or systemic acute toxicity. It is approved by the FDA (Food and Drug Association) and certified EN1935 from a food perspective.

The table 5.4 showcases the operating parameters of the DLC coating used for the analysis (Technical_Data_Sheet_DLC_PVD coating).

Parameter	Value
Composition	a-C:H
Hardness (HV)	2400
Coefficient of friction vs 100Cr6	0.12
Thickness (Micron)	2-4
Temperature of deposition	Max. 200 C
Temperature of use	Up to 350 C
Colour	Black

Table 5.4 Operating parameters - DLC.

5.2.2. Chromium nitride (CrN) coatings – Technical data

Another type of coatings that falls under PVD are CrN coatings. High hardness, high resistance to wear and corrosion, low friction coefficient, asepticity, and aesthetically pleasing properties are the attributes of coatings, with specific reference to Chromium Nitride (CrN). Titanium and its alloys as well as other kinds of steel, with the range of stainless steels providing specific confirmation, are among the materials on which CrN

can be deposited. As a substance that can come into contact with food, chromium nitride satisfies EN1935 regulations. PVD coatings meet the requirements of ISO 10993, which states that they are biocompatible and do not exhibit cytotoxicity, skin irritation, or systemic acute toxicity.

The table 5.5 showcases the operating parameters of the CrN coatings that were analysed (Technical_Data_Sheet_CrN_PVD_coatings).

Parameter	Value
Composition	CrN
Hardness (HV)	1800
Coefficient of friction vs 100Cr6	0.5
Thickness (Micron)	1-10*
Temperature of deposition	180-480 C
Temperature of use	Up to 750 C
Colour	Light Grey

Table 5.5 Operating parameters - CrN.

*High thickness version

5.2.3. Tungsten Carbide (WC/C) coatings – Technical data

Amorphous carbon flakes deposited via sputtering technology alternate with tungsten carbide flakes in the structure of WC/C. WC/C is characterized by its low friction coefficient, asepticity, high hardness, and wear resistance. Its low coefficient of friction, which can stop adhesive problems like seizing and cold welding, is its primary characteristic. In this sense, it is applied to all sliding components—including motor gears, camshafts, compressor screws, sliding guides, ball bearing rings, worm screws, and other moving parts—that are prone to inadequate lubrication. Among the most diverse parts are those used in the food industry, such as oil, pasta, and tobacco handling parts, as well as blades and discs for chopping tea and coffee. These parts are composed of a variety of materials, stainless steels and case-hardening steels in

particular, as well as titanium and its alloys. As little as 180°C can be reached for WC/C deposition.

The operating parameters of WC/C are given in table 5.6 (Technical_Data_Sheet_WC_PVD_coatings)

Parameter	Value
Composition	Tungsten Carbide & Carbon
Hardness (HV)	1300-1800
Coefficient of friction vs 100Cr6	0.15
Thickness (Micron)	1-4
Temperature of deposition	Max. 180 C
Temperature of use	350 C
Colour	Anthracite

Table 5.6 Operating parameters - WC/C.

5.3. Electroless Nickel coatings

Applying a particular finish, such as electroless nickel-phosphorus plating (Ni-P), is undoubtedly one of the traditional methods used in the manufacturing of industrial equipment to preserve the mechanical properties of a material, mainly carbon steel or low alloy steels, as well as to increase the resistance of surfaces to abrasion and corrosion (Fernando B. Mainier, Maria P. Cindra Fonseca, Sérgio S. M. Tavares, Juan M. Pardal, 2013). Carbon steel is coated with Ni-P without the need for an external electrical current. Consequently, this characteristic has either directly or indirectly resulted in the creation of new technologies and specialized instruments for industries in environments with high salinity and corrosive gases like CO_2 and H_2S (Fernando B. Mainier, Maria P. Cindra Fonseca, Sérgio S. M. Tavares, Juan M. Pardal, 2013).

5.3.1. Electroless Nickel - Technical data

Here we are going to see the characteristics & technical details of high phosphorous (10.5 – 12 %) and medium phosphorous (5.5 – 9 %) electroless nickel coatings. Firstly, we are going to see that of the high phosphorous nickel coatings. It is an electroless nickel plating process formulated to produce semi-glossy high-phosphorus deposits with minimal internal stresses, suitable for especially when high thicknesses are required. produces deposits with excellent functional properties in terms of ductility, reduced internal stresses in relation to the aging of the solutions, weldability, and corrosion resistance. It is recommended for applications where high resistance to corrosion is required and corrosion with low thicknesses due to low porosity.

The following table shows the physical properties of the coatings (Technical_Data_Sheet_Electroless_Nickel_High_Phosphorous).

Phosphorous content	10.5 – 12.0%
Hardness after deposition	450 - 525
Hardness after treatment at 400^0 C	850 - 950
Density (g/ cm ^3)	7.6 – 7.9
Melting point	880^0 C
Magnetic properties	Non - magnetic
Nitric acid test	Compliant

Table 5.7 Physical properties of high phosphorous nickel

Moving on, the next one is the one with medium phosphorous content (5.5 - 9%). It is an electroless nickel plating process that deposits an alloy semi-gloss nickel – phosphorus with a medium phosphorus content of 5 to 9%. Process with a high deposition rate while maintaining a high stability. This process does not contain Lead and Cadmium in accordance with the Directive European ELV relating to the end of vehicles. It is a chemical nickel process that is ideal for applications where a high

deposition rate is combined with high stability in a wide operating range. It is recommended for objects with a semi-glossy appearance and with moderate corrosion resistance requirements.

The following table showcases the physical properties of the coating (Technical_Data_Sheet_Electroless_Nickel_Medium_Phosphorous).

Phosphorous content	5.5 – 9.0%
Hardness after deposition	615/56
Hardness after treatment at 400^0 C	1.000/69
Melting point	880-1.150^0 C
Magnetic properties	Magnetic
Nitric acid test	Non-Compliant
Corrosion resistance (10μm)	96 h

Table 5.8 Physical properties of medium phosphorous nickel coatings

6 Characterization tests used

The main characterization tests used in the analysis are given in the table below.

Type of tests	**Features**	**Approximate quantity of samples required**
Microscopic inspection	Optical analysis on cross section and surface.	Approximately 1
	SEM analysis on cross section and surface.	
EDS analysis	For the identification of components. This is also carried out on the surface as well as on the cross section.	EDS is included in SEM. Approximately 1 in number.
Thickness measurement	Microscopic method (ASTM B487), XRF	Approximately 1
Hardness test	Vicker's test - ASTM E 384	Approximately 3
Corrosion resistance	Salt spray test - ASTM B 117	Significant Surface – 1 dm^2

Table 6.1 Characterization tests used.

6.1. Microscopic analysis

6.1.1. Scanning electron microscopic (SEM) analysis

A scanning electron microscope is a type of electron microscope that produces images of a sample by scanning it with a focused beam of electrons. The electrons interact with atoms in the sample, producing various signals that can be detected and that contain information about the sample's surface topography and composition. The most common mode of detection is by secondary electrons emitted by atoms excited by the electron beam (the number of secondary electrons is a function of the angle between the surface and the beam).

In a typical SEM, an electron beam is thermionically emitted from an electron gun fitted with a tungsten filament cathode. Tungsten is normally used in thermionic electron guns because it has the highest melting point and lowest vapor pressure of all metals, thereby allowing it to be heated for electron emission, and because of its low cost. Other types of electron emitters include lanthanum hexaboride (LaB6) cathodes and FEG, which can use tungsten single crystal emitters or emitters of zirconium oxide. The electron beam is focused by one or two condenser lenses, then passes through pairs of scanning coils or pairs of deflector plates in the electron column, typically in the final lens, which deflect the beam in the x and y axes so that it scans in a raster fashion over a rectangular area of the sample surface. When the primary electron beam interacts with the sample, the electrons lose energy by repeated random scattering and absorption within the interaction volume, which extends from less than 100 nm to approximately 5 μm into the surface.

The size of the interaction volume depends on the electron's landing energy, the atomic number of the specimen and the specimen's density. The energy exchange between the electron beam and the sample results in the reflection of high-energy electrons by elastic scattering, emission of secondary electrons by inelastic scattering and the emission of electromagnetic radiation, each of which can be detected by specialized detectors. Electron amplifiers of various types are used to amplify the signals, which are displayed as variations in brightness on a computer monitor. Each pixel of computer video memory is synchronized with the position of the beam on the specimen in the microscope, and the resulting image is therefore a distribution map of the intensity of the signal being emitted from the scanned area of the specimen.

Magnification in an SEM can be controlled over a range of up to 6 order of magnitude, from about 10 to 500000 times. The most common imaging mode collects low-energy of an X-ray beam. The number and energy of the X-rays emitted from a specimen can

be measured by an energy-dispersive spectrometer. As the energy of the X-rays are characteristic of the difference in energy between the two shells, and of the atomic structure of the element from which they were emitted, this allows the elemental composition of the specimen to be measured.

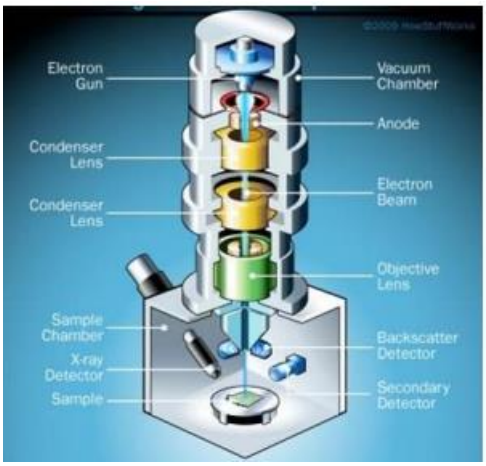

Figure 6.1 Schematic representation of SEM components.

For conventional imaging in the SEM, specimens must be electrically conductive, at least at the surface, and electrically grounded to prevent the accumulation of electrostatic charge at the surface. Nonconductive specimens tend to charge when scanned by the electron beam, and especially in secondary electron imaging mode, this causes scanning faults and other image artifacts. They are therefore usually coated with an ultrathin coating of electrically conducting material, deposited on the sample by sputter coating. In this work, the conductive material used for the sputter coating is silver.

Scanning electron microscope analysis of chromium plated samples is useful in order to observe more details than those observed with the optical microscope. In fact, it is possible to achieve higher magnifications and better resolutions than those obtained with the optical microscope. Furthermore, using the X-rays microanalysis, it is possible to obtain relevant information about the chemical composition of the layers of the different kinds of coating.

Thickness measurement is also included in the microscopic inspection alongside the spectra of coatings for identifying the composition as well.

6.1.2. Optical microscopy

The surface of the sample to be observed is placed on the sample holder, adjustable via two micrometer screws, in the center of which there is a hole for the passage of light. The light coming from a source appropriately collimated by diaphragms and capacitors, is directed through a mirror to the surface of the specimen after passing through the objective lens, figure 6.2. The reflected light is focused into the objective lens again; the signal light is deflected by the prism toward the ocular lens which allows a magnified view of the sample. The signal can finally be deflected by a mirror and sent to a camera. The specimen is placed on the sample holder of the optical microscope and it's possible to proceed with the observation of the coating layers. What is observed at this point is a coating consisting of a layer of copper, a single layer of nickel and a very thin layer of chromium. In order to highlight the different layers of nickel which form the plating , it is necessary to perform a chemical etching. This etching is done by using a solution of 50% acetic acid and 50% nitric acid. The sample is then rinsed with alcohol. Once identified all the different layers which form the chromium plating on the plastic material, is possible to proceed with the measurement of thicknesses at several points throughout the entire sample. This procedure is done using 500X magnification, by means of the appropriate analysis software interfaced to the camera attached to the microscope.

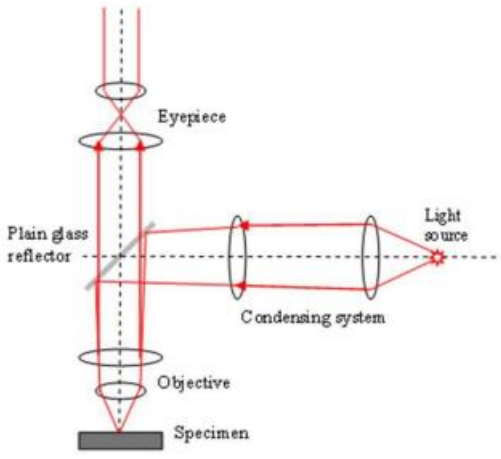

Table 6.2 Optical path in an optical microscope.

6.2. Neutral salt spray test for corrosion resistance

6.2.1. Apparatus used

This test provides an accelerated means of simulating the effects of on-vehicle service in corrosive environments on materials, coatings, parts, and components. This method is based on the appearance, at each time and under attack of corrosive agents, of marks or spots differing in color or appearance from the surface being inspected.

The severity level of the corrosion test will be a function of the following parameters:

- concentration of corrosive agent selected.
- duration of the test.

In the following section, the different components of the salt spray test are reviewed.

Cubic fog chamber, in which corrosive solution is atomized. Fog chamber is coated internally with an inert material (hard rubber, polyvinyl chloride, polyester resin, glass, methacrylate ester, stoneware). The chamber is provided with an air-tight door cover and two apertures measuring a few square centimeters. Of the latter, the aperture in the highest part of the chamber serves as an outlet for the salt fog and is therefore connected to a tube in inert material leading to the outside of the building. The aperture at the base of the chamber is to drain drops of solution which accumulate through condensation on interior of chamber, or which fall from specimens being tested. The chamber is covered to prevent drops of solution accumulating through condensation from falling on specimens being tested. A heater is installed to maintain the chamber temperature. The heater is equipped with an adequately sensitive thermostat and ensures uniformity of temperature inside the chamber. Next is the air supply and conditioning system.

Air supply and conditioning system consisting of:

- A source of compressed air at a pressure of 0.7 to 1.7 bar free from oil and from impurities.
- A pressure regulator valve, where compressed air pressure exceeds 1.7 bar.
- A humidifier, to maintain the solution at the temperature in the chamber (i.e., to prevent evaporation of droplets). The humidifier allows air bubbles to pass through at least 30 cm of distilled water at 55 to 60 °C. The resulting air has a temperature of above 35 °C and relative humidity of approximately 95%. The humidifier is provided with a thermostat to stabilize the water temperature.

An Atomizer made using an inert material (e.g., glass or methacrylate ester) is used for the apparatus. The chamber is provided with nozzles that will be able to maintain

the pluviometric conditions. However, direct striking of the spray jets does not take place during the test. A reservoir in corrosion resistant material of sufficient capacity to hold enough solution for at least 3- or 4-days operation is kept in close vicinity to the arrangement. A thermometer is equipped to measure the temperature in the chamber. The thermometer and sensor of the thermostat are kept adjacent. Another important part of the apparatus is a fog collector. It consists of a 100 mm glass funnel (collecting area of 80 cm^2) with the stem inserted through a rubber stopper into a 250 cm^3 graduated cylinder.

6.2.2. Chemical composition of corrosive environments

Sodium chloride: 50 ± 5 g/l

Check that the solution collected in fog collector is of same composition as original solution. If dilution occurs, atomized air is too humid, which in case reduces the temperature of water in the humidifier. Should the collected liquid be more concentrated than the original solution, increase humidity by raising the water temperature in the humidifier or decreasing supply of air bubbles. Once optimum conditions have been reached, a solution may be used for long periods.

Other factors are:

- Relative humidity – 95%
- pH = 6.5 ÷ 7.2
  If necessary, pH shall be corrected by adding a few drops per liter of HCl N/1 or NaOH N/1 to the solution to lower or raise pH respectively.
- Pluviometric constant = 1 ÷ 2 cm^3/h
  The pluviometric constant, which is a function of the fog concentration, is found by collecting the fine condensate precipitating from the fog over a known area, ideally over a horizontal plane. To determine pluviometric constant, use fog collector positioned as far as possible from the nozzle so that it does not collect drops falling from specimens exposed to the fog.
- Temperature = 35 ± 2 °C

6.2.3. Test procedure

The surface under the test is thoroughly degreased using a solvent and then is cleaned using a suitable detergent. After washing with water, the film of water on the surface

being tested shall not be broken. In the case of conversion layers or layers which have been purposely impregnated with organic substances for protection, preparation of surfaces is with cleaning agents that do not attack the applied products. If specimens have been prepared from coated pieces, cut edges are covered with suitable adhesive tape so that corrosion propagating from edges does not interfere with results.

Exposure conditions in chamber are as follows:

- Specimens are positioned in the chamber so that the solution spray does not impinge upon it.
- Specimen support is an inert nonmetallic material (plastic).
- The significant surface of the specimen faces upwards to form an angle of 30 ± 5° from the vertical. When evaluating results, surfaces facing downwards are not considered.

During extraction, care should be taken to not touch the significant surfaces of the specimens with fingers. Laboratory forceps are used for this. After extraction, samples are immersed in clean running water followed by washing with distilled water and lightly blow dry with compressed air free from water and oil. During this operation, extra care should be taken to prevent corrosion products from being separated or removed.

Corrosion resistance is evaluated with the naked eye at normal reading distance. Test results are evaluated in one of the ways:

- Number of corrosion spots per unit of surface after a given exposure period.
- Time taken for the first corrosion spot to appear or changes to occur.

6.3. Hardness test

Hardness shall be determined exclusively by means of small penetrators, such as the Vickers penetrators with minimum loads (varying in relation to chromium thickness). This is a typical micro indentation test in which the Vicker penetrator applies a minimum test force on the exposed surface of the specimen. As a result of this, a small indentation is created on the surface of the specimen which is then measured using a light microscope.

A diamond with a square base shaped like a right pyramid makes up the indenter, Figure 6.3. The vertex angle between opposing faces should be 136° +/- 0.5°. An accurate two-circle goniometer must have been used to confirm this angle. There is roughly a 7:1 relationship between the depth of the indentation, h, and the diagonals d1 and d2. Each line of junction (offset) between two opposing faces must be greater

than 0.5 μm. The four faces must all be evenly inclined to the indenter's axis (within 0.5°) and meet at a single place, ISO 4516 – 2002 .

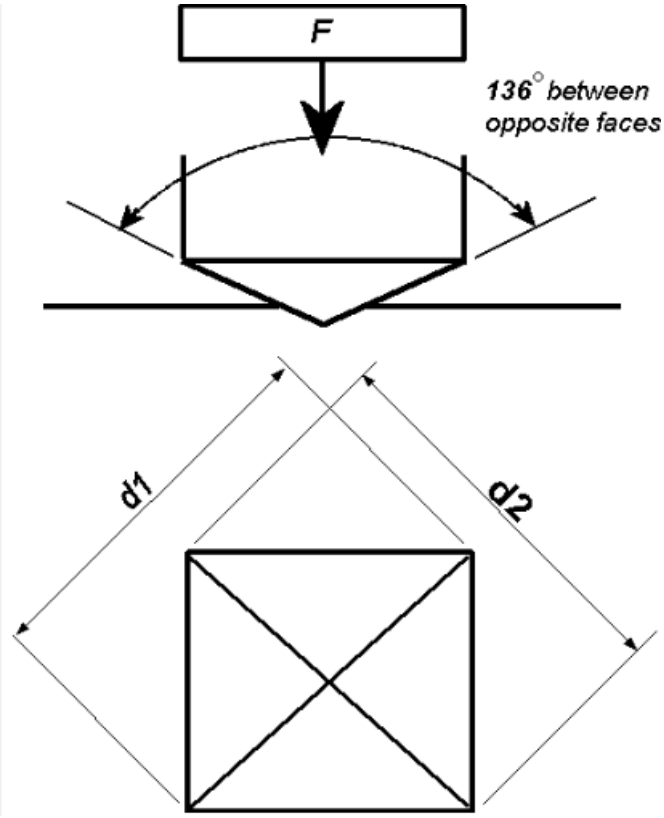

Figure 6.2 Vicker's indenter

The hardness is characterized by the Vicker hardness number, calculated by dividing the applied force to the exposed surface area of the specimen onto which the force is applied. For our analysis the standard ASTM E384 was used.

7 Results & Discussion

7.1. Microscopy with thickness analysis

7.1.1. Electroless nickel coating – Pulleys

The electroless nickel coating process adopted for this research consisted of 6 samples named as sample A, sample B, sample C, Sample D, sample E, and sample F. These 6 samples correspond to the different stages of the coating processes. Also, these 6 stages can be classified as process 1 and process 2. Process 1 begins with sample F followed by B & C. Similarly, process 2 begins with sample F, followed by E, D, and A in chronological order. Sample A - Vaporized + Sand Blasted + Nickel + Heat treated, sample B - Vaporized + Nickel, sample C - Vaporized + Nickel + Heat treated, sample D - Vaporized + Sand blasted + Nickel, sample E – Vaporized + Sandblasted, and sample F – Vaporized. So, process 1 begins with sample F.

Figure 7.1 Sample F - stereomicroscope image

Figure 7.1 shows the stereomicroscopic image of sample F. The arrow indicates the zone where the defect (stain) is observed. The representative SEM images of the surface inside and outside the defect are reported, while there is no difference in the EDS spectrum inside and outside the defect.

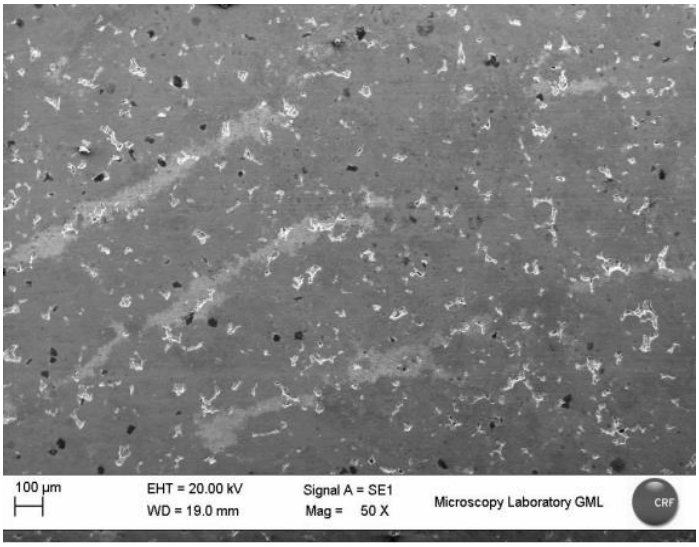

Figure 7.2 SEM image inside the defect - F

It has already been discussed that sample F corresponds to steam treatment (vaporizing). This is mainly done to generate an oxide layer to protect the part from corrosion during transportation and storage. In this process, there is no nickel coating takes place. This is kind of a preliminary stage to get the sample ready for coating process. Figure 7.2 shows the typical sem image (inside the defect) of the vaporized sintered material under consideration. From this figure, it is quite clear that the surface has a uniform distribution of pores (white spots), a typical characteristic of sintered material. Also, it is evident the presence of slender grey areas, which actually represent the base material. However, these slender grey areas are not so visible in the sem image (outside). This is shown in Figure 7.3.

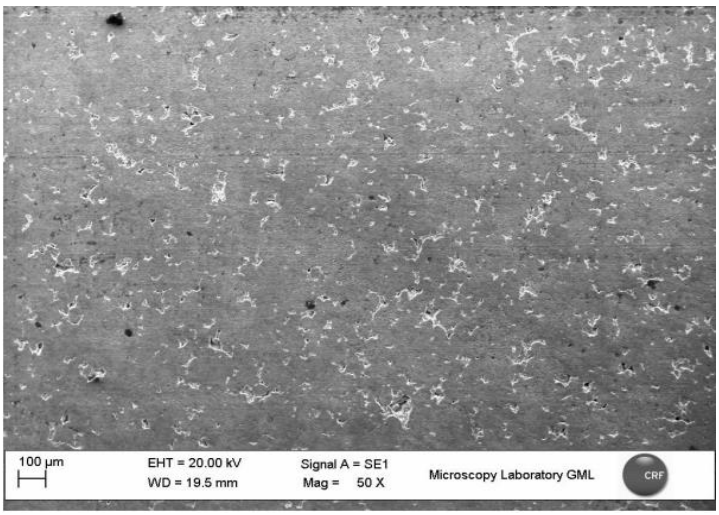

Figure 7.3 SEM image outside of the defect - F

It is evident from the figure that the sample has a uniform morphology with uniform distribution of the pores exactly similar to the previous image. The elemental composition of the material can be understood by observing the X-ray microscopic analysis of the sample (same for both inside & outside). This is shown in figure 7.4.

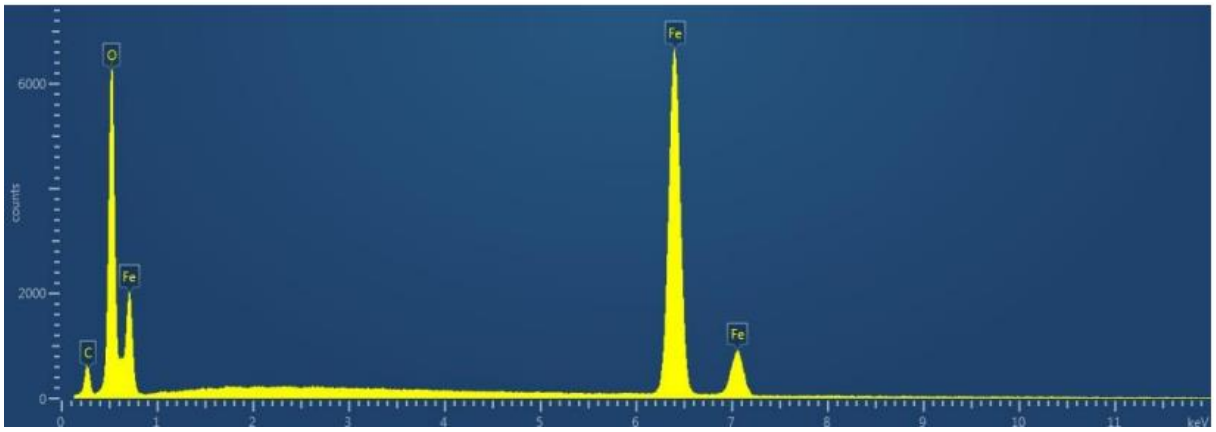

Figure 7.4 X-ray image of F both outside and inside the defect.

From the above figure, it is understandable that oxygen and iron account for as the major constituents of the sample. This represents the formation of the oxide layer with iron and oxygen due to the steam treatment process. Small traces of carbon can also be seen. This is due to organic contamination (resin) during the analysis. Now, moving on to the cross-section analysis, it gives information about the microstructure, uniformity, and thickness of the coating.

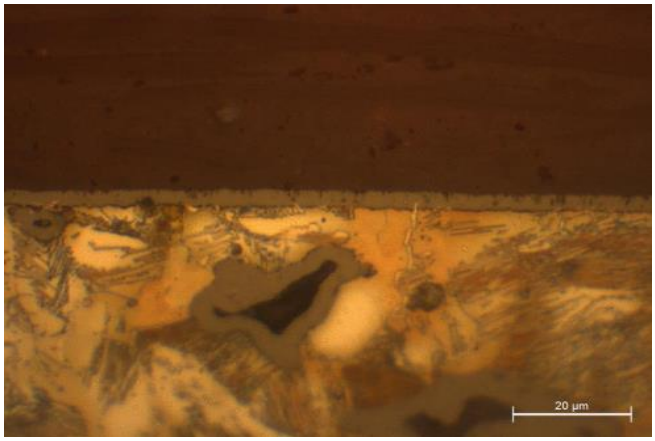

Figure 7.5 Image of the oxide coating.

In the figure above, the top layer represents the organic resin applied for the analysis, the small middle layer represents the iron-oxide layer formed because of steam treatment process, and the bottom part represents the base material. It is seen that the

base material consists of uneven voids, as mentioned above earlier, a characteristic of sintered material. The thickness of the oxide layer is found out to be around 2-3 micrometers. Regarding the bottom layer, which represents the base material, the microstructure is lamellar pearlite and ferrite. Uneven distribution of the voids (pores) can be seen. The elemental composition of the sample can be better understood by EDS analysis. This is shown in figures 7.6 and 7.7.

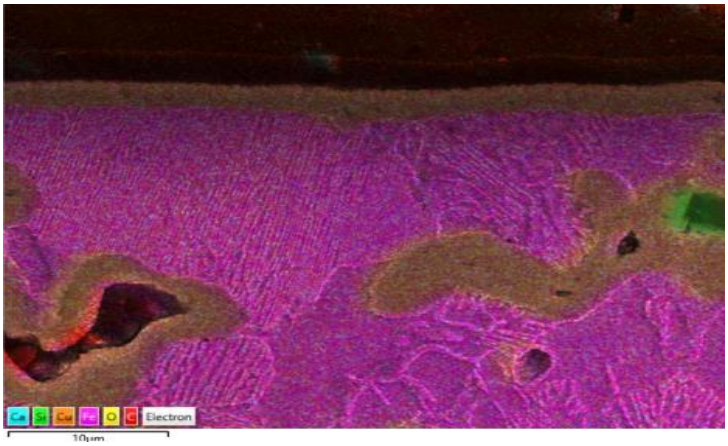

Figure 7.6 EDS distribution of F.

In the figure the different color code represents different elements that are present in the sample. This picture once again confirms what was discussed earlier. i.e., the presence of oxide layer (the middle layer with iron and oxygen, oxygen in yellow and iron in violet, the combination of both colors is seen in the middle layer). The top layer, which is black, represents carbon due to the application of the resin. Small traces of other elements such as silicon and calcium are observed in the sintered base material.

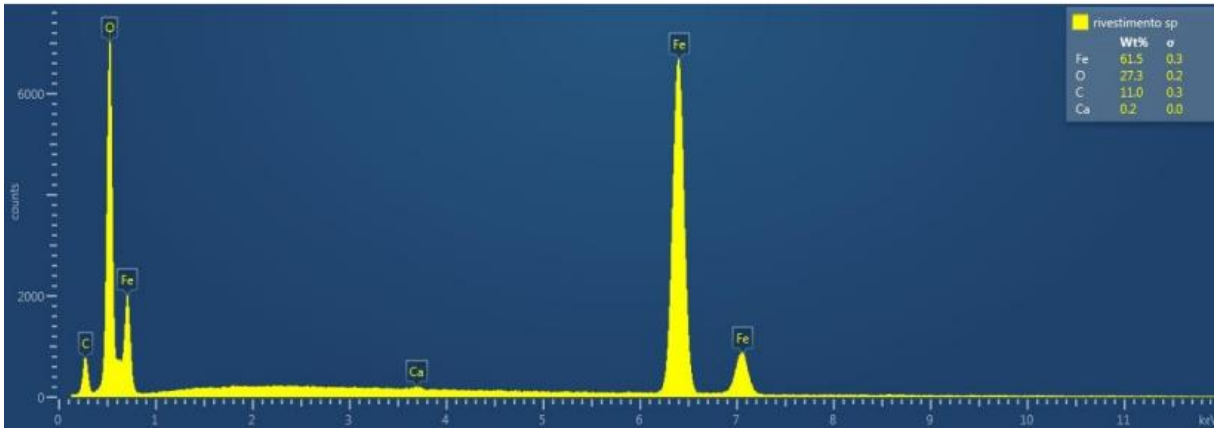

Figure 7.7 X-ray micrograph highlighting the composition of F.

Similarly, in the X-ray micrograph (cross-section), the weight percentage of different constituents is evaluated and shows the clear indication of the oxide layer along with some other elements such as carbon and calcium as minorities (inorganic contamination).

Moving on to the next step of process 1, i.e., sample B – vaporized + nickel, ni-p is coated on top of the oxide layer that has been formed in the previous step.

Figure 7.8 SEM image of B.

The figure shows the SEM image when viewed under the microscope, where the arrow represents the presence of stains on the surface. Here also, the surface outside and inside the defects are studied to get relevant information about the uniformity of the surface and the presence of irregularities. Figures 7.9 and 7.10 represent the outside and inside images respectively.

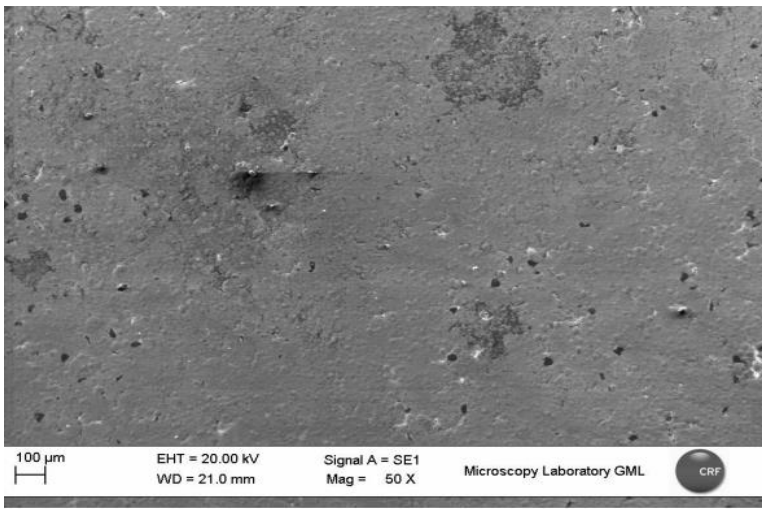

Figure 7.9 SEM image outside of F.

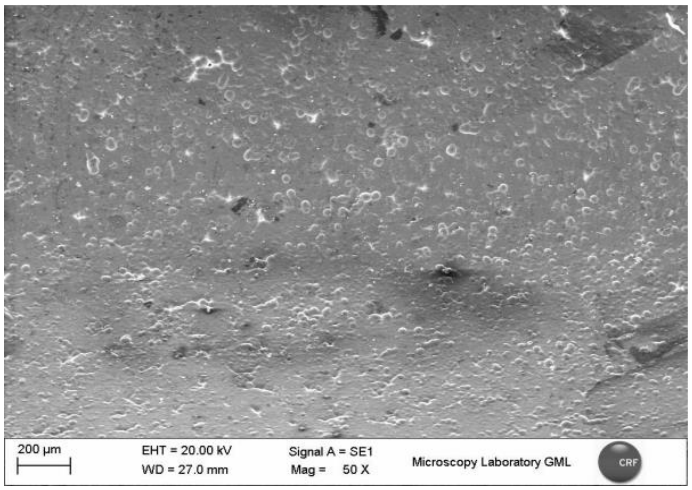

Figure 7.10 SEM image inside.

In both outside and inside, the distribution of the coating is uniform and compact. In both the figures, pores can be seen due to the material being sintered. However, in the image inside the defect, white stains are present due to contamination which is not present in the image outside the defect. Comparing these images with that of sample f, the pores observed are less. This is due to the Ni-P coating. To better understand the composition on the surface, X-ray micrograph should be considered.

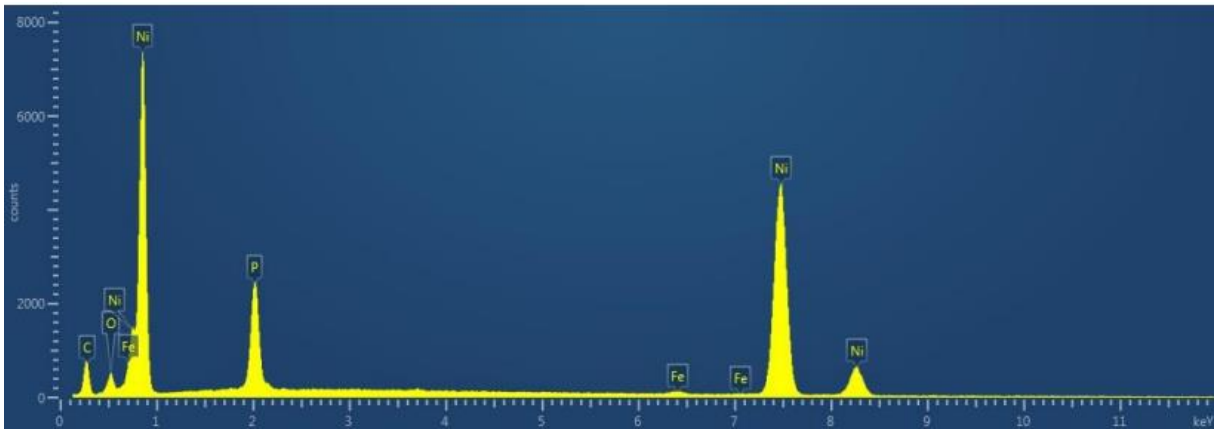

Figure 7.11 X-ray spectrum of B on surface.

From the spectrum, the presence of Ni-P coating can be clearly seen. Besides this coating, the presence of oxygen and iron can be seen which accounts for the oxide layer formed during the steam treatment process. However, compared to F, the oxide layer is so small due to the presence of Ni-P coating. Small traces of carbon can be seen due to organic contamination. Now, by analyzing the micrographic results on cross-section, the presence of coating and oxide layer can be confirmed.

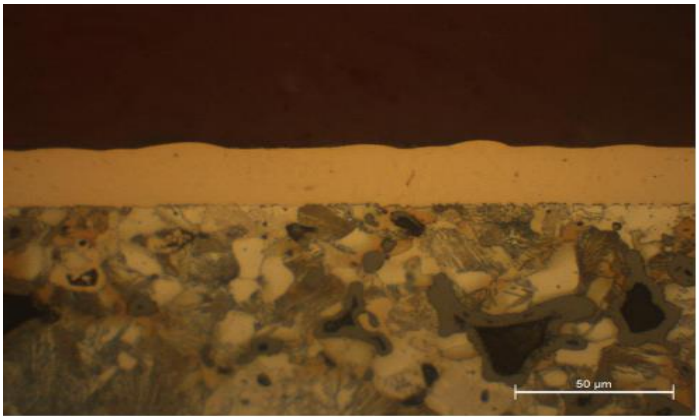

Figure 7.12 Cross-section of sample B.

In the above figure, the top layer represents the organic resin used for the analysis. The middle layer represents the uniform Ni-P coating which is around 22-24 micrometers in thickness. However, as we mentioned earlier, beneath this Ni-P layer, there is a thin oxide layer formed due to steam treatment during F, but it is not clearly visible as it is very thin. The bottom layer shows the microstructure of the base material with lamellar pearlite and ferrite structure. The structure shows the presence of uneven voids (sintered material). The presence of the different layers can be further confirmed by the EDS and X-ray micrographs on the cross-section. These are shown in figures 7.13 and 7.14 respectively.

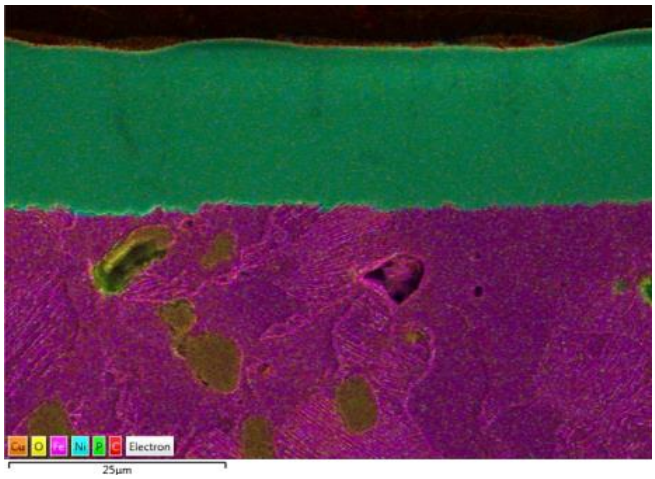

Figure 7.13 EDS distribution of B.

The bluish green layer represents the Ni-P coating on the base material. Just beneath it, a very thin combination layer of yellow (oxygen) and violet (iron) is there which is the oxide layer. Unfortunately, it is not so visible to the naked eye. But it can be very much affirmed by the X-ray spectrum.

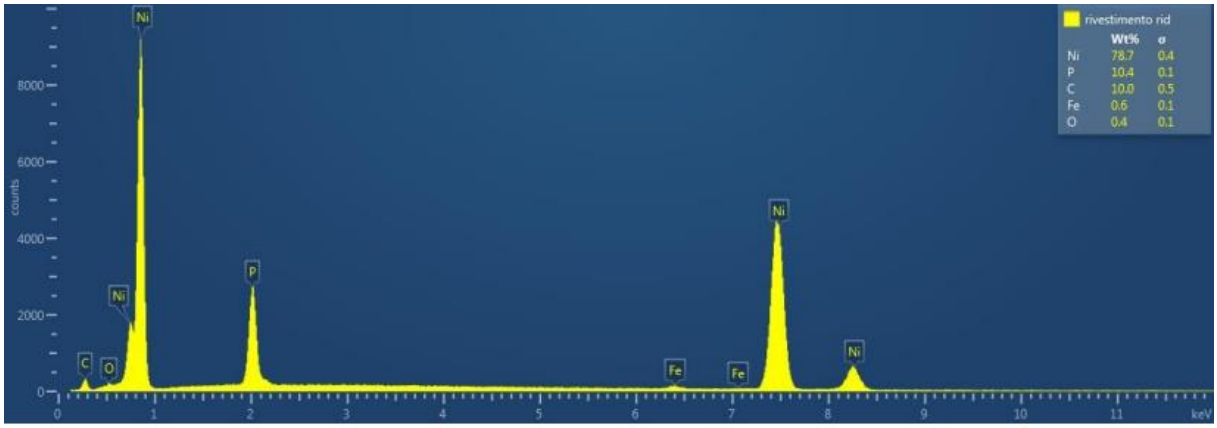

Figure 7.14 X-ray micrograph on the cross-section of B.

From the above spectrum, it can be concluded the presence of Fe-O oxide layer even though it is in very few traces. In the majority, the Ni-P coating is present. A small quantity of carbon is also present due to organic contamination.

Sample C accounts for the last step in process 1 of the coating process. In this step the previous sample is heat treated. Here also, the oxide layer from the previous step is present. Additionally in this case, there will be spots (not big craters) on the surface due to heat treatment application.

Figure 7.15 SEM image of C.

The figure above shows the sem image of sample C, where the arrow indicates the presence of stains (defects). By observing the inside and outside images of the defects, the distribution of the spots as well as the porous nature of the surface is observed. These are shown in figures 7.16 and 7.17.

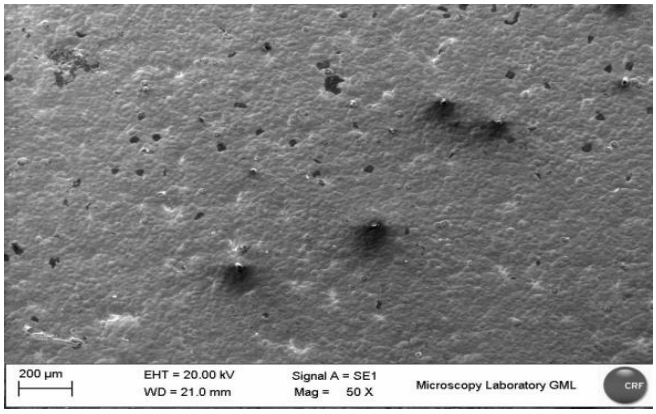

Figure 7.16 SEM image outside the defect of C.

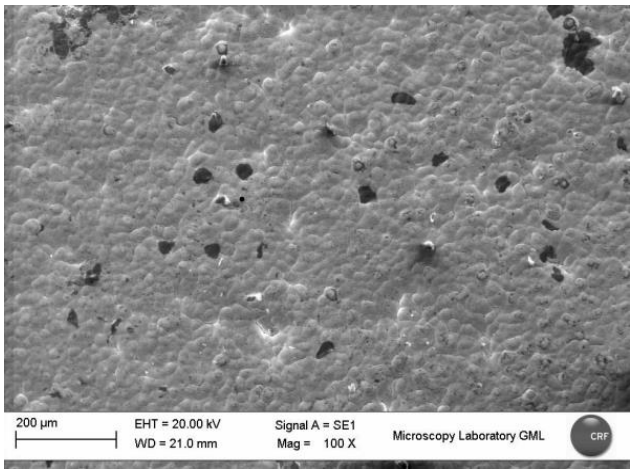

Figure 7.17 SEM image inside of the defect of sample C.

Comparing the above 2 images, the presence of spots due to heat treatment is much clearer in the SEM image corresponding to that of the inside. The porous nature of the material is observed due to the presence of white spots (sintered material). By analyzing the X-ray micrograph on the surface, a better understanding of the elemental constituents on the sample can be obtained.

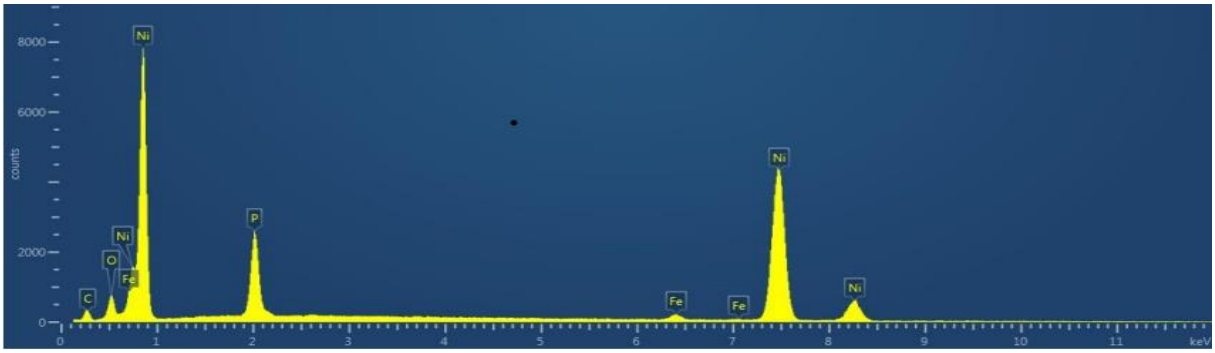

Figure 7.18 X-ray micrograph on surface of C.

The X-ray micrograph shows valid information about the different elemental constituents. As it can be seen that Ni-P accounts for the majority alongside a very small composition of iron and oxygen confirming the presence of the very thin oxide layer produced during the previous step.

Moving on to the micrographic cross-sectional analysis, relevant informatin regarding the microstructure, thickness and distribution of the coating is obtained. Figure 7.19 shows the crossectional view of the sample consisting of the different layers.

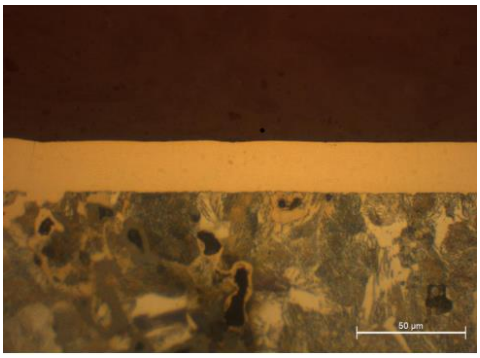

Figure 7.19 Cross-sectional view of C.

From the above figure, a uniform middle layer is seen which represents the Ni-P coating which is around 22-24 micrometers in thickness. The bottom layer shows the base material which has a lamellar pearlite and ferrite structure. Unevenly distributed voids and heat spots can be observed in this layer. However, the heat treatment does not have significant effects (spots, blisters…) on the appearance of the coating layer. Here also, an oxide layer is there but not so visible. The presence of oxide can be confirmed by looking into the X-ray analysis. Figures 7.20 and 7.21 show the EDS as well as X-ray results on the cross-section respectively.

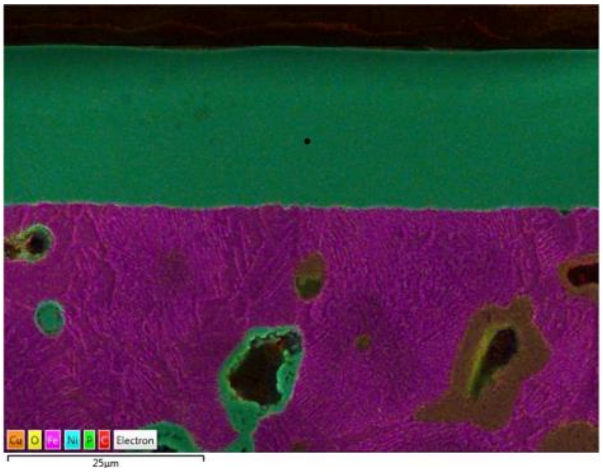

Figure 7.20 EDS analysis on cross-section of C.

As was with the case of previous step, the thick bluish green layer represents the Ni-P coating. Just like the previous case, there is an oxide layer beneath the nickel coating which can be confirmed by the X-ray micrograph on the cross-section. The bottom layer shows the base material (violet) with voids with some other elements. The top portion, which is red in color represents carbon, present due to organic contamination.

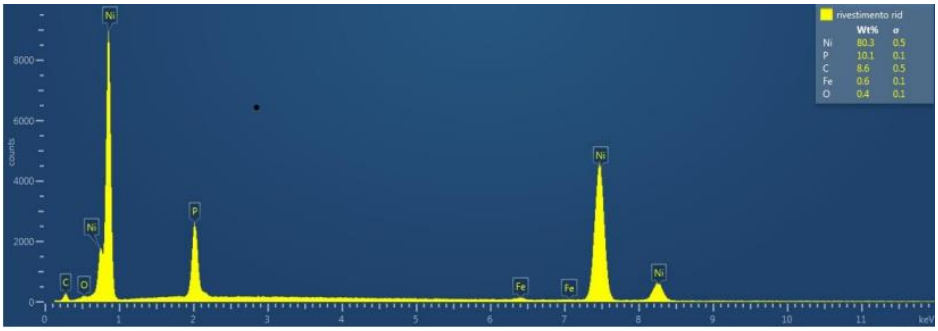

Figure 7.21 X-ray micrograph on cross-section of C.

X-ray micrograph on the cross-section of C gives the elemental composition of the sample. The small amounts of iron and oxygen account for the presence of the oxide layer in between the nickel layer and base material. As expected, in major composition, the Ni-P layer is observed. Some amounts of carbon are also observed due to organic contamination (application of resin).

So, these three steps conclude process 1. Process 2 begins with sample F, i.e., the steam treated sample that we have already discussed. Following this, the next step is the analysis of sample E. Sample E is the process in which the vaporized sample is subjected to sand blasting. Sand blasting is a mechanical process in which the surface is struck by metallic spears to get rid of the oxide layer generated during the steam treatment. This is because the oxide layer lessens the adhesion of the Ni-P layer on the base material. For better adhesion, it is always suggested to avoid any intermediate layers in between the coating and the base material. Figure 7.22 shows the SEM image of E under the microscope.

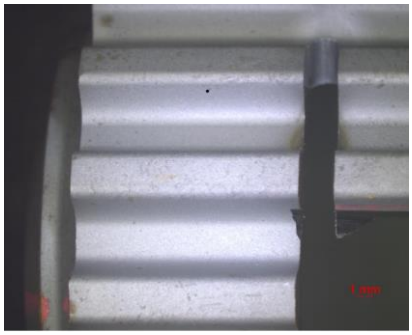

Figure 7.22 SEM image of E under microscope.

The image under microspe showed that there were no surface defects present. The Sem image of the surface was able to give relevant information about the uniformity and appearance of the surface. Figure 7.23 shows this.

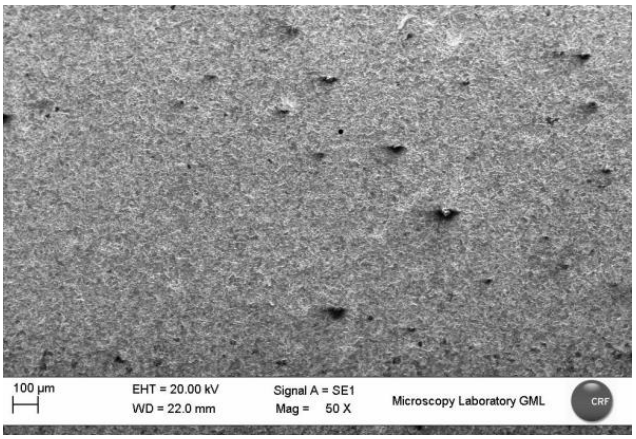

Figure 7.23 SEM image of the surface of E.

Here, a very uniform and compact structure is observed with spots due to sand blasting. The sample is devoid of any form of coating or oxide layer (sand-blasted). This can be better understood by cross-sectional analysis.

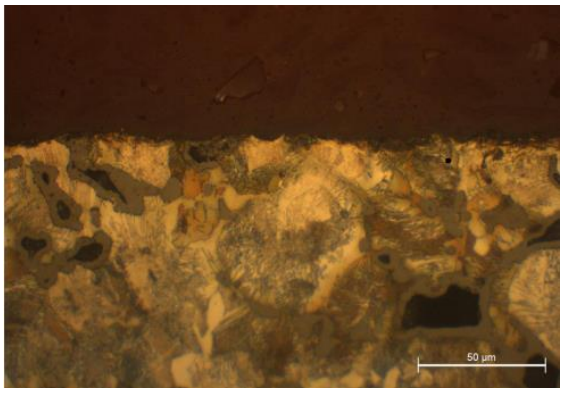

Figure 7.24 Cross-sectional analysis of E.

Here only two layers can be observed. The top layer for the organic resin and the bottom layer for the base material. The microstructure of the base material is the same throughout the whole procedure with lamellar pearlite and ferrite structure. Since this step only consisted of sand blasting of the vaporized sample, the sample became devoid of any coating or oxide layer. So, there is no need for further analysis such as EDS and X-ray spectrum for this case.

The next step in process 2 is sample D which accounts for the coating of Nickel on the sample from the previous step.

Figure 7.25 SEM image of D under microscope.

The above figure shows sample D under stereomicroscope in which the arrow indicates the defect (stain). For further information, the surface image outside and inside the defects are observed. These are shown in Figures 7.26 and 7.27 respectively.

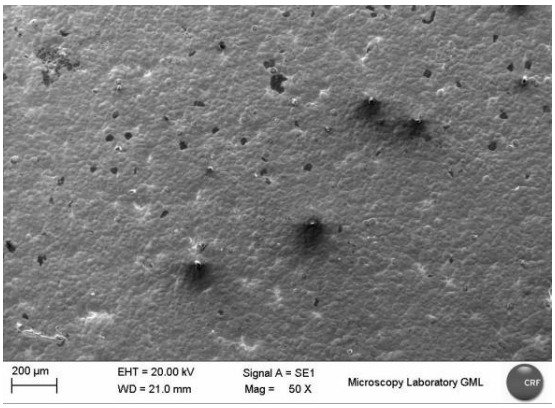

Figure 7.26 Surface outside the defect.

In the above picture, spots due to the sand blasting from the previous sample are seen. The surface shows uniform morphology with pores (sintered material). However, in figure 7.27, the spots are not that much highlighted and have a very uniform and pleasing appearance with uniform distribution of the pores.

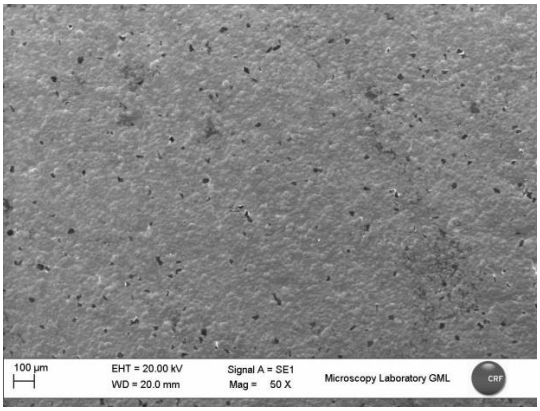

Figure 7.27 Surface inside the defect.

By analyzing the X-ray micrograph of surface, details about the Ni-P layer can be understood. Figure 7.28 shows this.

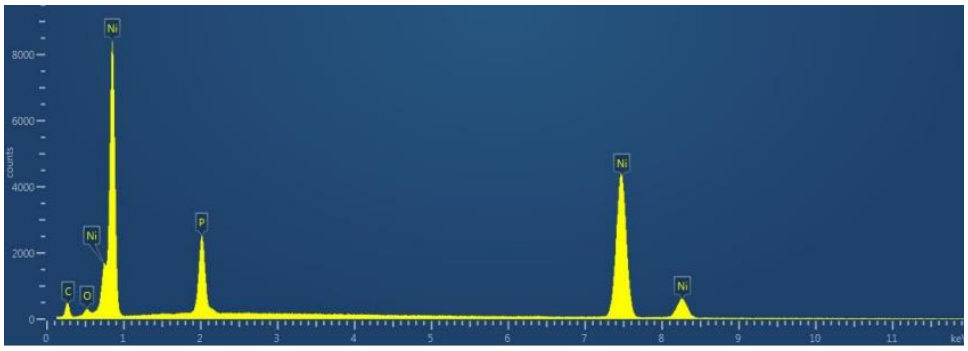

Figure 7.28 X-ray on the surface.

From the above picture, the sample only contains Ni-P as the major coating. As a result of sand blasting the vaporized sample got devoid of the oxide layer to provide better adhesion for the coating on the Ni-P layer. Some other elements such as carbon and oxygen are present due to contamination. The cross-sectional analysis of sample E gives information about the coating thickness and the microstructure. This is shown in figure 7.29.

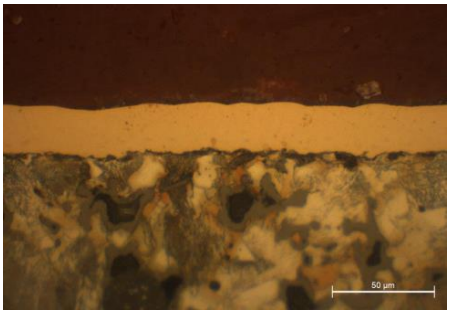

Figure 7.29 Cross-sectional view of D.

The uniform middle layer represents the Ni-P coating with a thickness of around 20-22 micrometers. The top layer, as in the previous cases represent the application of resin for the analysis. The bottom layer is the base material with lamellar pearlite and ferrite which is the same in all the cases. Uneven distribution of voids can be seen in the microstructure due to the material being sintered. Further information regarding the elemental composition is given by EDS and X-ray micrograph on the cross-section.

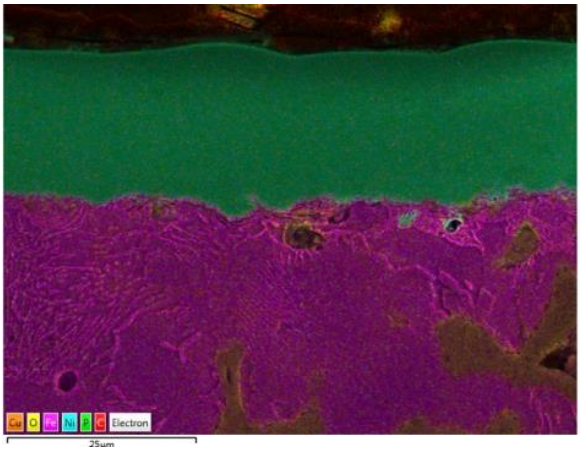

Figure 7.30 EDS analysis on cross-section.

Here also, the thick bluish green layer represents the Ni-P coating. The oxide layer is absent in this case on a first glance. As in the previous cases, the top red portion shows the contaminants during the resin application and the bottom violet coloured layer shows the base materials. Presence of somer other elements is also accounted in the base material.

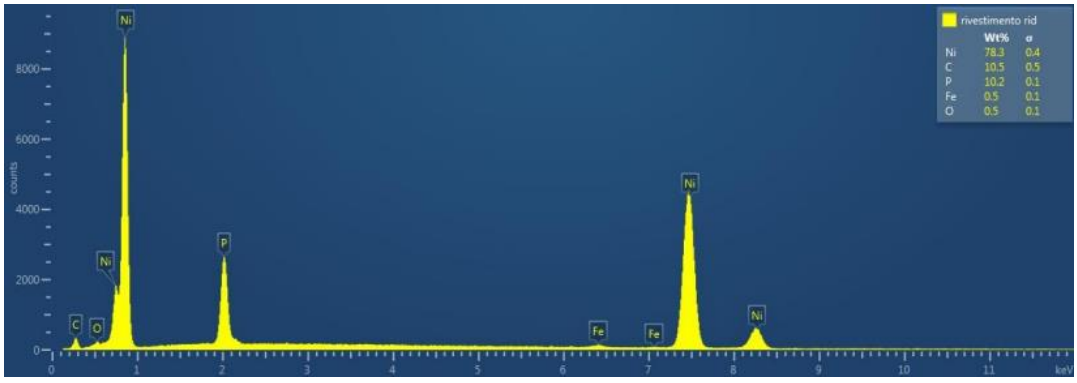

Figure 7.31 X-ray analysis on the cross-section.

In the X-ray micrograph, Ni-P accounts for the major constituent. With this analysis, it is quite clear that the oxide layer has been almost completely removed. Still, a very

minute quantity of iron and oxygen can be seen in the graph. This shows that sand blasting has not been successful in eliminating the oxide layer completely. This means that these parts should be scraped off before subjecting to bench tests due to concerns regarding adhesion. Small traces of carbon can be seen due to the application of resin (organic contamination).

The final step of process 2 and the whole of nickel coating is sample A. The sample from the previous stage is heat treated in this stage. Figure 7.32 shows the sample under stereomicroscope.

Figure 7.32 A under SEM.

The figure shows the SEM image of the surface of sample A when viewed under the microscope. The arrow points out the stains (defects). Further information regarding the sample is obtained through surface analysis and cross-sectional analysis. Figures 7.33 and 7.34 show the representative SEM images outside and inside the defects respectively.

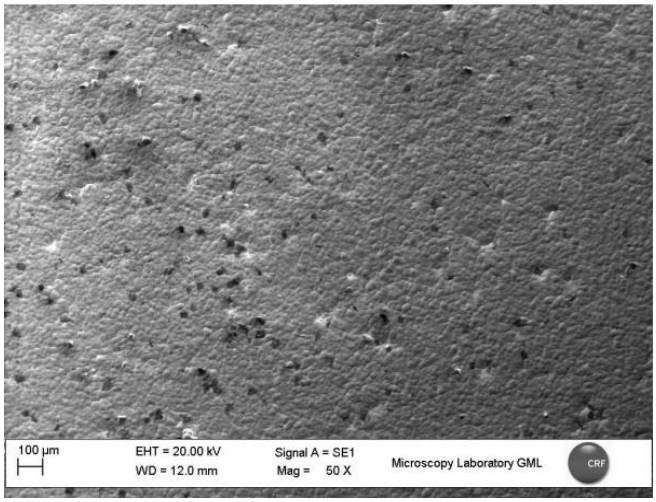

Figure 7.33 SEM image outside the defect of sample A.

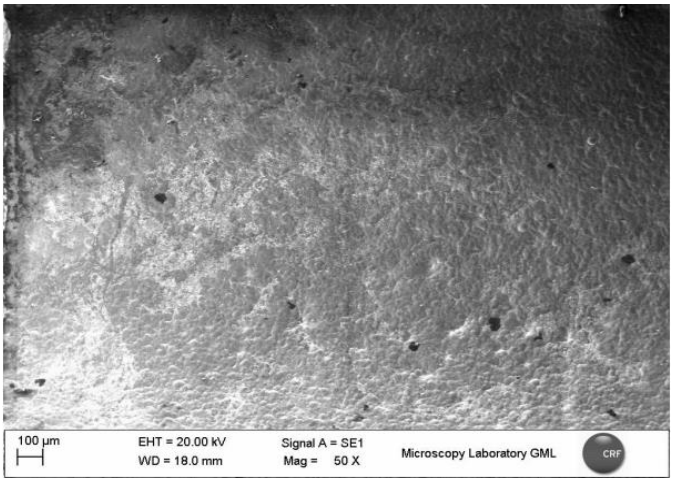

Figure 7.34 SEM image inside the defect of sample A.

In the two figures 7.33 and 7.34, there is a uniform distribution of the surface with pores here and there (sintered material). Some spots are present in both the figures due to the heat treatment activity. Heat treatment does not affect the microscopic results as it is a visual characteristic, however, it affects the hardness of the coating. By looking into the X-ray micrograph on the surface, further information about the composition of can be drawn out. This is shown in figure 7.35.

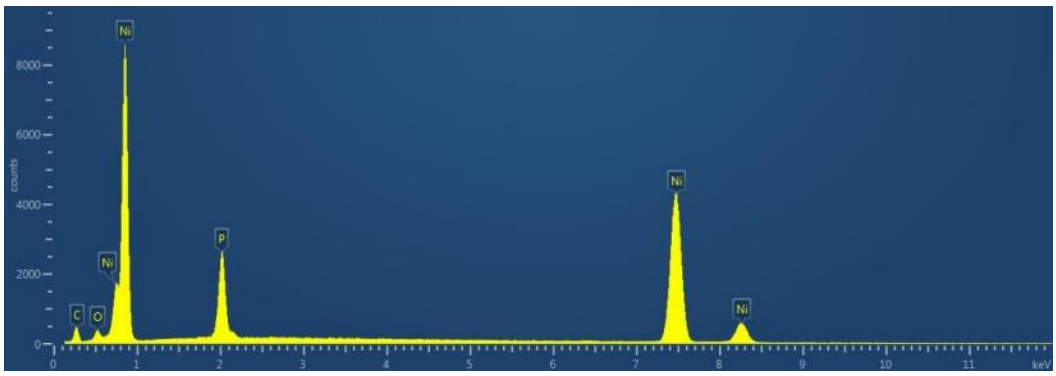

Figure 7.35 X-ray micrograph on the surface of A.

From the spectrum, Ni-P is the only major coating on the sample as it is shown in major proportion. Besides this, carbon and oxygen are also present in minor quantities. This is due to organic contamination.

Moving on to the cross-sectional analysis, data regarding microstructure, thickness and elemental composition can be further analyzed and confirmed. Figure 7.36 represents the cross-sectional view of sample A.

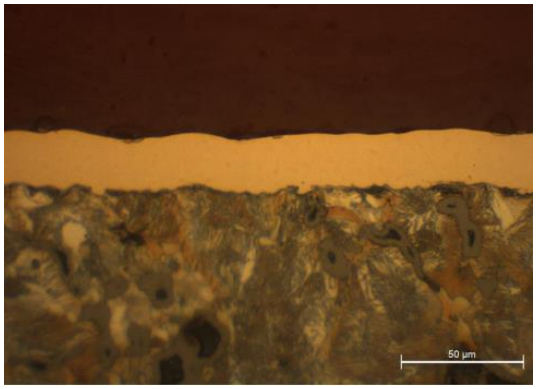

Figure 7.36 Cross-sectional view of sample A.

In the cross-sectional view, a very uniformly thick middle layer can be seen which accounts for the Ni-P coating. The thickness was found to be 20-22 micrometers. There were no irregularities or defects in the coating layer. As we have seen in previous cases, the microstructure of the base material (bottom layer) is the same i.e., lamellar pearlite and ferrite with uneven distribution of pores. Likewise, the top layer represents the resin used for the analysis. EDS analysis and X-ray spectrum on the cross-section gives much more detailed information on the composition. Figures 7.37 and 7.38 show this.

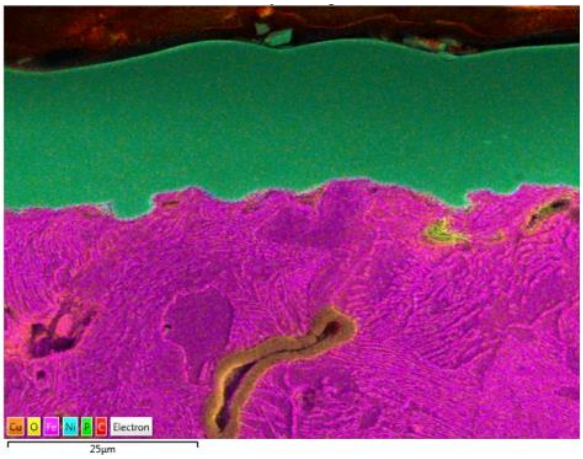

Figure 7.37 EDS analysis on cross-section of A.

The bluish green layer accounts for the Ni-P coating layer, while the violet layer accounts for the base material with other elements (probably contaminants) in small proportions. The top layer which is a combination of red and black represents the resin used for the analysis.

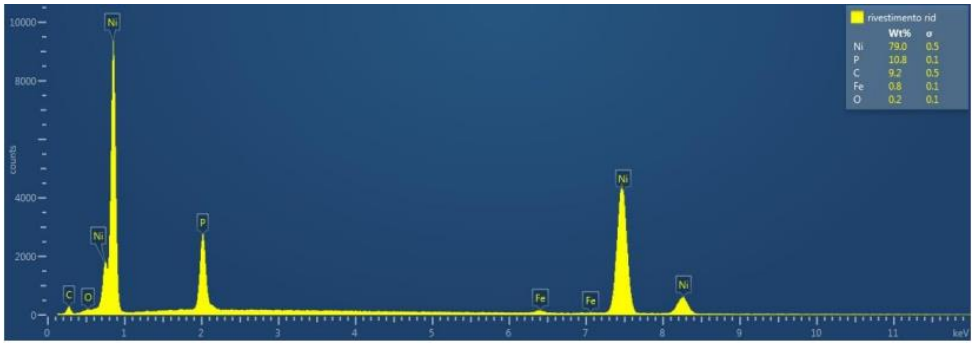

Figure 7.38 X-ray spectrum of the cross-section of sample A.

From the spectrum, the major coating present is Ni-P. Here also, as we have seen in the previous case, a small amount of oxygen and iron is present accounting for the fact that there is a slightly thin oxide layer even after the sand blasting process (sample a is obtained by carrying out heat treatment was carried on the previous sample). This should be considered as a warning to scrape off those parts before bench tests. Traces of carbon are present showing organic contamination.

7.1.2. Hexavalent Chromium coating

The microscopic analysis of hexavalent chromium coating is carried out and the following results are obtained. Figure 7.39 represents the macro image of the cross-section.

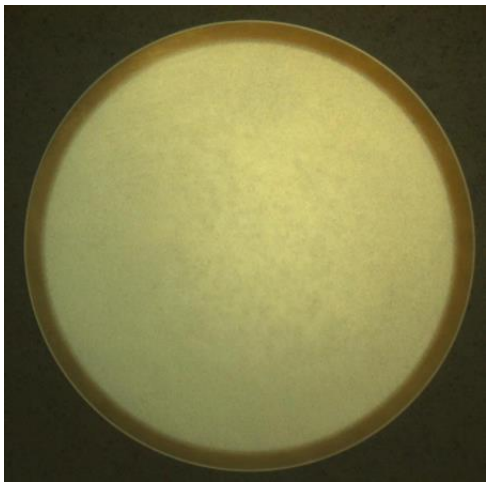

Figure 7.39 Macro image of Cr (VI).

In the figure, there is a uniformly distributed coating on the top layer of the base material. The chromium coating thickness is measured as 28-33 micrometers. From the analysis it has been understood that the microstructure on the surface is tempered martensite while inside the core, it is lamellar pearlite and ferrite. In both surface and core, a uniform distribution of grains is observed. Figure 7.40 represents the sectional view of the coating on the base material.

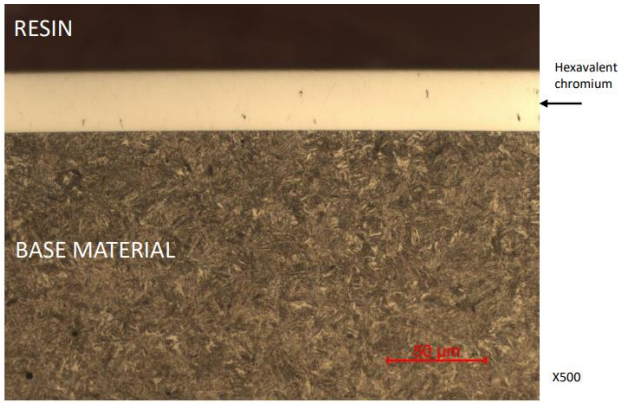

Figure 7.40 Cross-sectional view of Cr (VI) on the base material.

Here, it is clearly understood that there is a uniformly thick Cr (VI) coating in between the base material and the resin. There has been no defect or porosity observed in the structure. The base material is also free of defects / irregularities and has a very compact granular representation. The elemental composition of the sample can be understood by the X-ray spectrum. This is shown in figure 7.41.

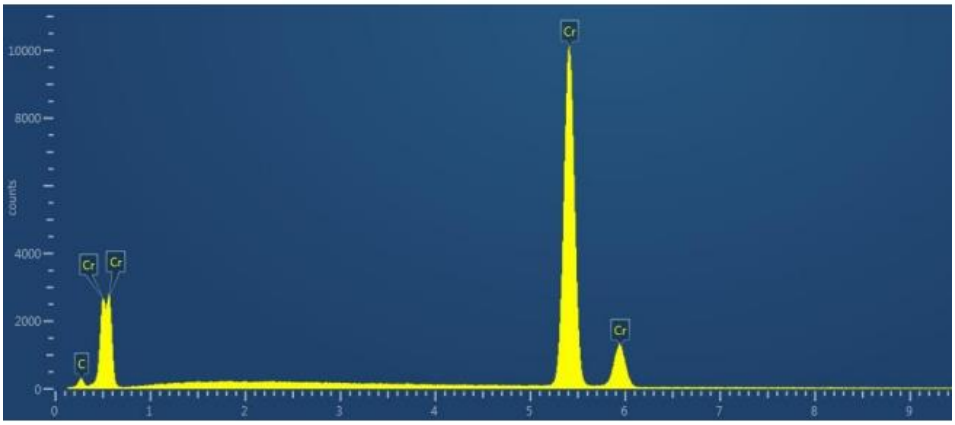

Figure 7.41 X-ray micrograph of Cr (VI).

From the X-ray micrograph, chromium accounts for as the major coating. Trace amounts of carbon can also be found due to the application of resin (organic contamination).

7.1.3. Trivalent chromium coating

The microscopic analysis of trivalent chromium coating is carried out and the following results are obtained. Figure 7.42 represents the macro image of the cross-section.

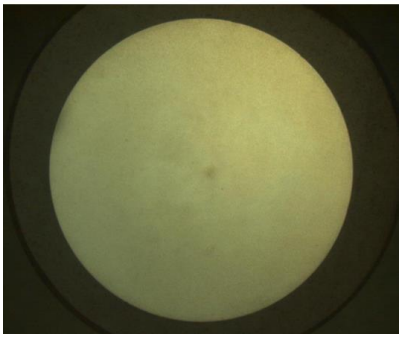

Figure 7.42 Macro image of Cr (III).

In the figure, there is a uniformly distributed coating on the top layer of the base material. The chromium coating thickness is measured as 13-23 micrometers comparatively low with Cr (VI). From the analysis it has been understood that the microstructure is lamellar pearlite and ferrite. A uniform distribution of crystal-like grains is observed in the microstructure. Figure 7.43 represents the sectional view of the coating on the base material.

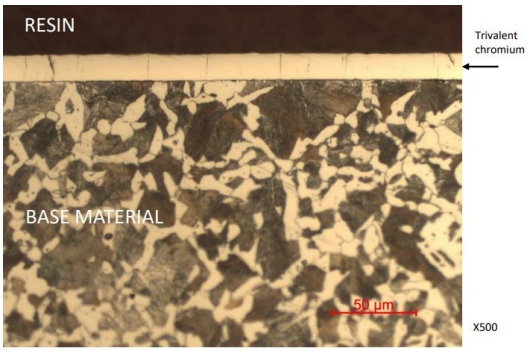

Figure 7.43 Cross-section of the coating.

Here, it is clearly understood that there is a uniformly thick Cr (III) coating in between the base material and the resin. There has been no defect or porosity observed in the structure. The base material is also free of defects / irregularities and has a very compact crystal-like granular representation. The elemental composition of the sample can be understood by the X-ray spectrum. This is shown in figure 7.44.

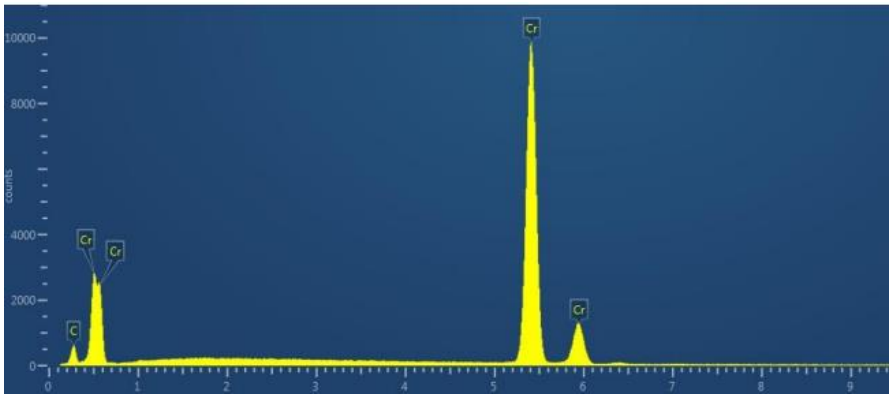

Figure 7.44 X-ray spectrum of Cr (III).

From the X-ray micrograph, chromium accounts for as the major coating. Trace amounts of carbon can also be found due to the application of resin (organic contamination).

7.1.4. Diamond like carbon coatings (DLC) – PVD coatings

The microscopic analysis results of DLC sample are given below.

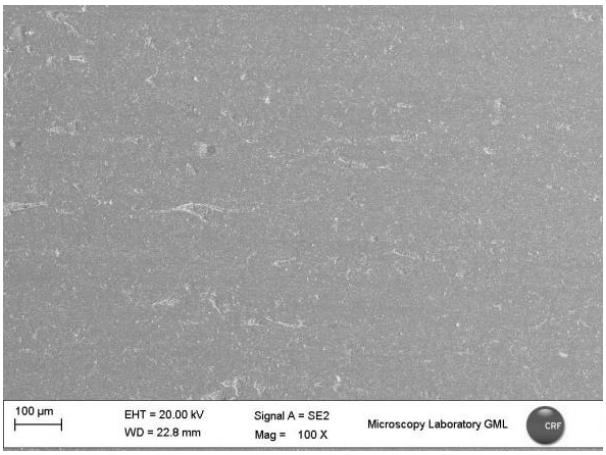

Figure 7.45 Surface image of DLC.

In figure 7.45, a very clean and uniform surface distribution free of defects / irregularities is obtained. Unlike nickel coatings where the base material always consisted of voids, here voids are absent (because of the lack of sintering). The X-ray micrograph gives information regarding the elemental composition. This is shown in figure 7.46.

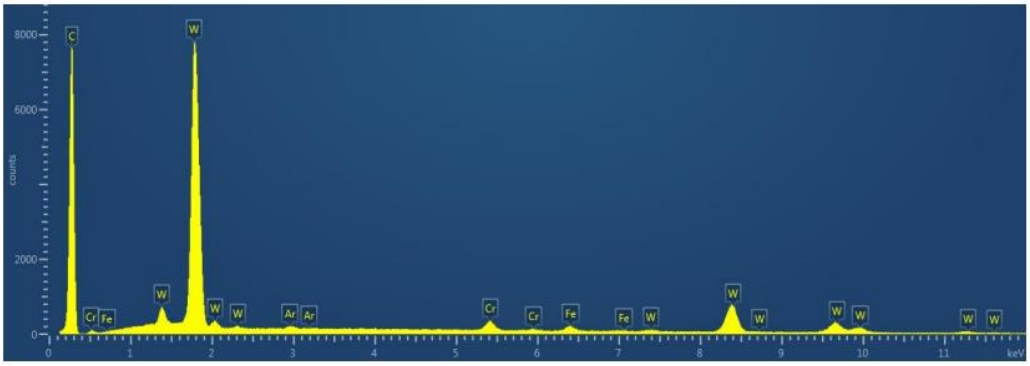

Figure 7.46 X-ray spectrum of DLC on surface.

Here we can see a variety of elements. In a DLC coating typically there are 3 layers. A base layer of chromium, on top of that, another layer of tungsten and finally on top of that layer, the DLC layer. This can be confirmed by analyzing the above image. Other elements are also present in minorities (application of resin and etchants – organic contamination).

Next, we have the cross-sectional analysis. In the cross-sectional analysis, clear information regarding the microstructure and thickness of the layers is obtained.

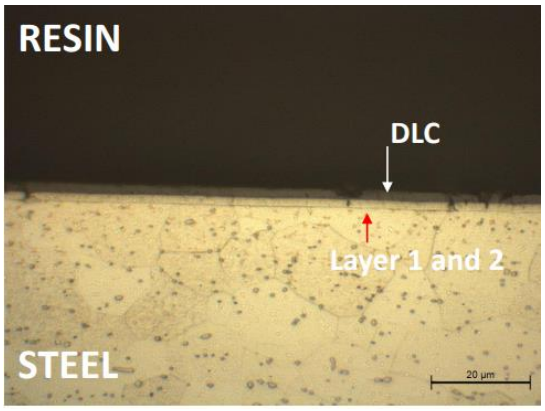

Figure 7.47 Image of the layers.

The above figure represents the different layers in the DLC sample. The topmost layer accounts for the application of resin while the bottom layer shows the microstructure of the base material. It was understood that the microstructure of the base material

was ferrite with carbides with the dimension of ferritic grain being 7.5 – 8 ASTM. Layer 1 represents the base chromium layer which is approximately 900 nm in thickness. The layer above it, which is the base tungsten layer, is approximately 700 nm in thickness. The DLC layer is the 3rd layer which is on top of the tungsten layer and is approximately 2 micrometers in thickness, considerably higher thickness compared to the base layers. EDS analysis and X-ray analysis can further confirm the presence of these layers. Figures 7.48 and 7.49 represent this.

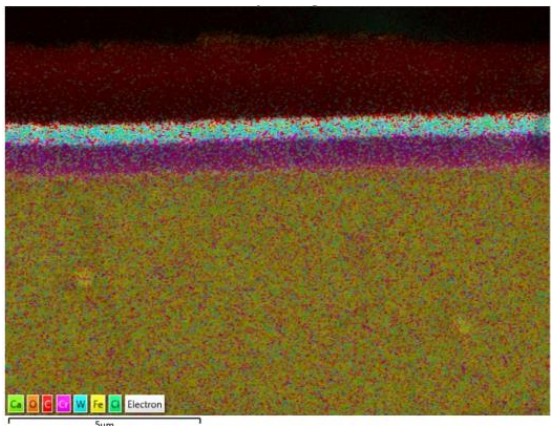

Figure 7.48 EDS analysis of DLC.

Here, it can be confirmed that the presence of the different layers. The middle layers, which are a combination of light blue, red and violet account for tungsten, carbon, and chromium accounts for base layers and DLC coating. In the bottom layer, which is the base material, trace amounts of other metals can be observed. This is due to contamination during the process. The elemental composition can be further confirmed by the X-ray spectrum of the sample.

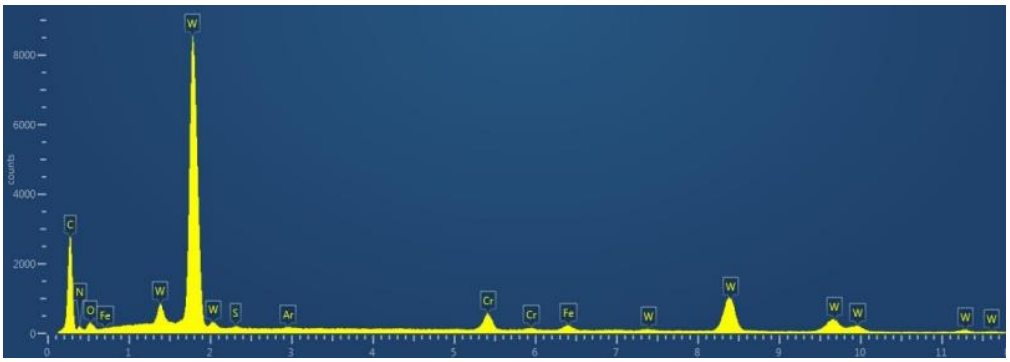

Figure 7.49 X-ray spectrum of DLC cross-section.

The X-ray spectrum of the cross-section gives clear cut idea about the different elements present in the sample whether it is for the coating, the base layers, and the contaminants.

7.1.5. Chromium nitride coatings (CrN) – PVD coatings

The microscopic analysis results of CrN sample are given below.

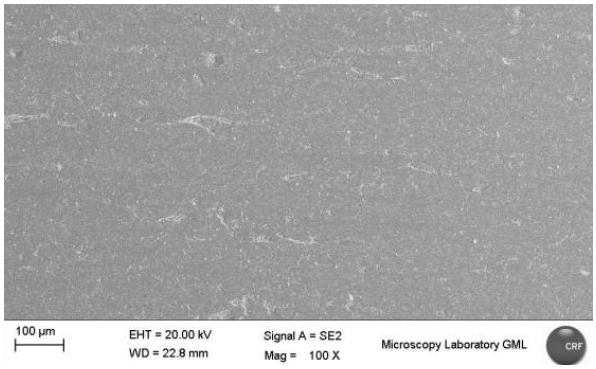

Figure 7.50 SEM image of CrN.

In figure 7.50, a very clean and uniform surface distribution free of defects / irregularities is obtained. As with the previous case, here also, voids are absent (because of the lack of sintering). The X-ray micrograph gives information regarding the elemental composition. This is shown in figure 7.51.

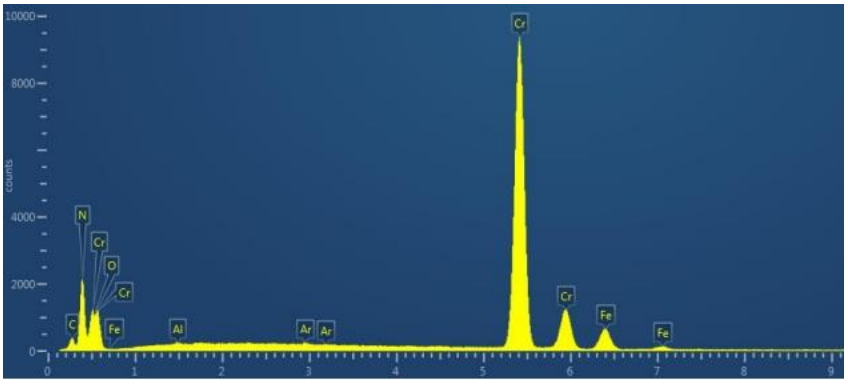

Figure 7.51 X-ray on the surface.

Here we can see a variety of elements. Unlike the DLC coating, the CrN coating consists of only one layer. This layer is formed by chromium and nitrogen. This can be

confirmed by analyzing the above image. Other elements are also present in minorities such as carbon, aluminum, argon and so on (application of resin and etchants – organic contamination).

Next, we have the cross-sectional analysis. In the cross-sectional analysis, clear information regarding the microstructure and thickness of the layer is obtained.

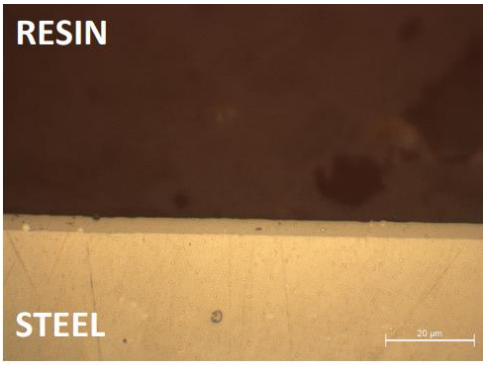

Figure 7.52 Cross-sectional view of the coating.

The above figure represents the layer in the CrN sample. The topmost layer accounts for the application of resin while the bottom layer shows the microstructure of the base material. It was understood that the microstructure of the base material was ferrite with carbides with the dimension of ferritic grain being 7.5 – 8 ASTM. The middle layer is the CrN layer which was found out to be 3-4 micrometers. EDS analysis and X-ray analysis can further confirm the presence of CrN layer. Figures 7.53 and 7.54 represent this.

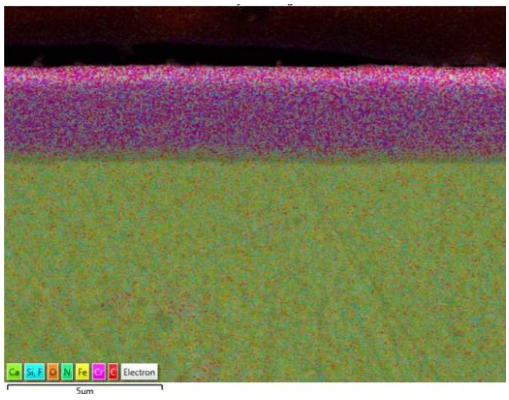

Figure 7.53 EDS analysis on Cross-section.

Here, it can be confirmed that the presence of the CrN layer. The middle layer, which are a combination of violet and light green represents chromium and nitrogen which accounts for the coating. In the bottom layer, which is the base material, trace amounts

of other metals can be observed. This is due to contamination during the process. The elemental composition can be further confirmed by the X-ray spectrum of the sample.

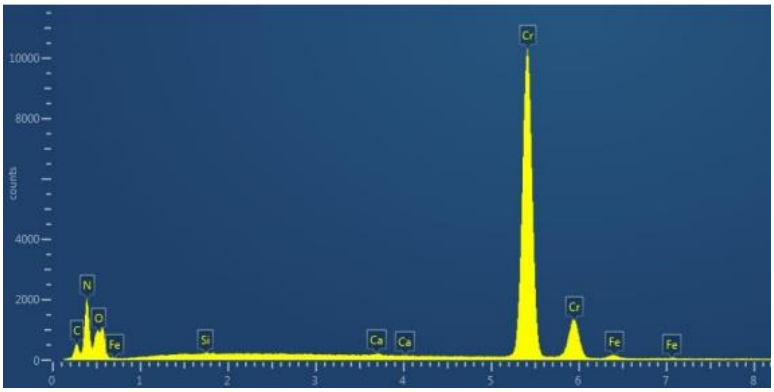

Figure 7.54 X-ray analysis of coating on the cross-section.

The X-ray spectrum of the cross-section gives clear cut idea about the different elements present in the sample whether it is for the coating, and the contaminants. N and Cr represent the CrN layer, while elements such as C, Si, Ca and so on are contaminants due to coating process and resin application. Fe represents the base material.

7.1.6. Tungsten carbide coatings (WC) coatings – PVD coatings

The microscopic analysis results of WC sample are given below.

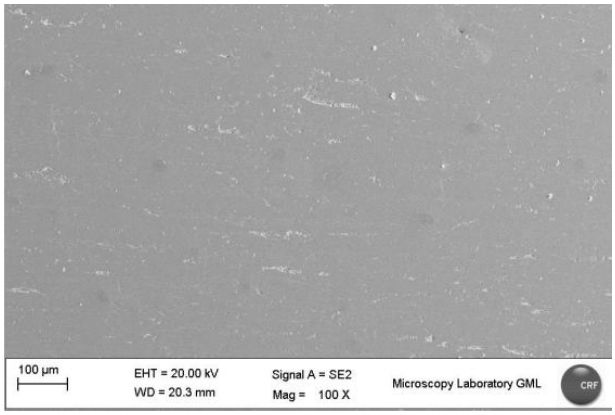

Figure 7.55 SEM surface image of WC.

In figure 7.55, a very clean and uniform surface distribution free of defects / irregularities is obtained. As with the previous case, here also voids are absent

(because of the lack of sintering). The X-ray micrograph gives information regarding the elemental composition. This is shown in figure 7.56.

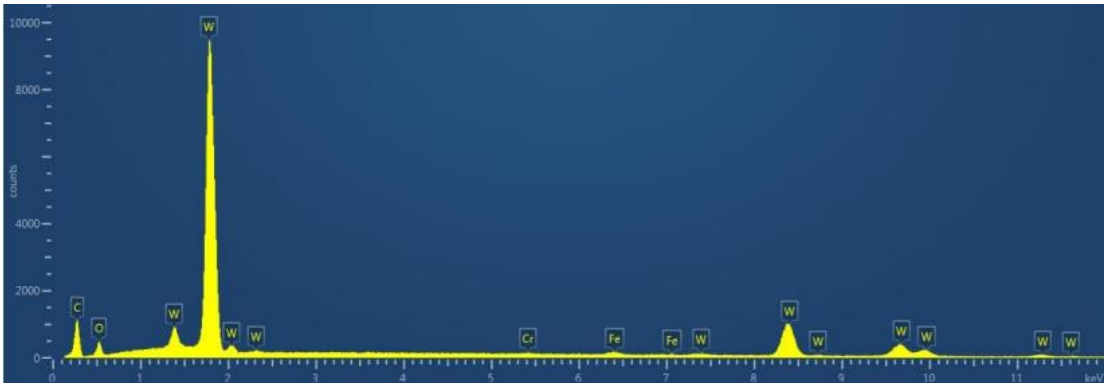

Figure 7.56 X-ray micrograph on the surface.

Here also we can see a variety of elements. The coating layer is formed by tungsten and carbon. However, in the WC coating a very thin chromium under layer is present. This can be confirmed by the above image as well as the EDS analysis. Fe accounts for the base material while other elements are due to contamination.

Next, we have the cross-sectional analysis. In the cross-sectional analysis, clear information regarding the microstructure and thickness of the layer is obtained.

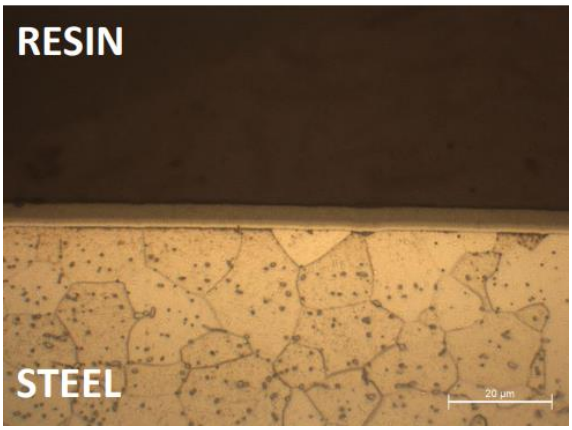

Figure 7.57 Cross-sectional view of the coating.

The above figure represents the layer in the WC sample. The topmost layer accounts for the application of resin while the bottom layer shows the microstructure of the base material. It was understood that the microstructure of the base material was ferrite with carbides with the dimension of ferritic grain being 7.5 – 8 ASTM. The middle layer is the WC layer which was found out to be 3-4 micrometers, the same as that of CrN

coating. EDS analysis and X-ray analysis can further confirm the presence of WC layer. Figures 7.58 and 7.59 represent this.

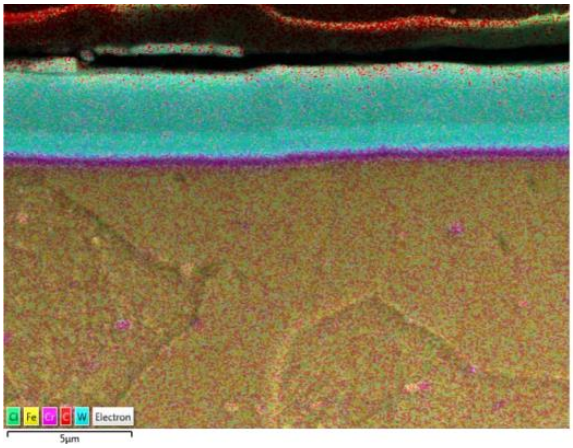

Figure 7.58 EDS analysis of WC.

In the EDS analysis, there have been some slight differences as compared to the CrN coatings. Here, a thin chromium under layer is formed just beneath the WC (red and light blue) coating, which is represented in violet. Also, another major difference is the detachment of the topmost layer with the WC coating. This might be due to the polishing of the section. The base material remains the same with some contaminants. This can be further confirmed by The X-ray microanalysis of the coating on the cross-section. The following figure shows this.

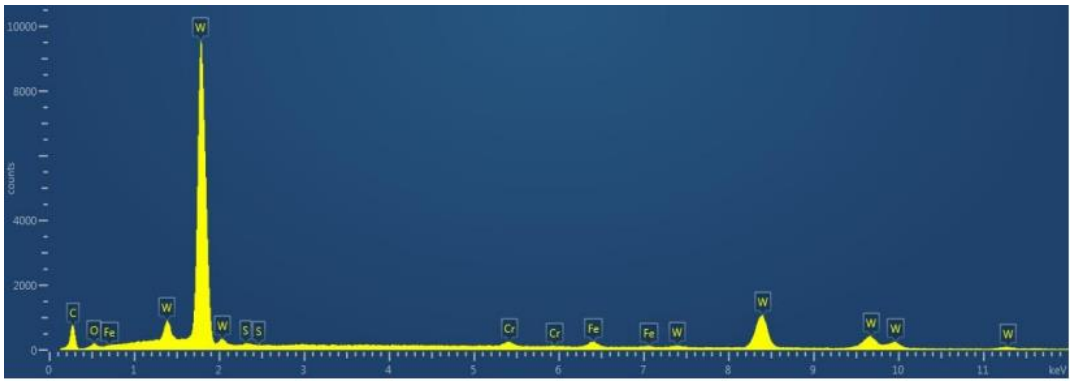

Figure 7.59 X-ray microanalysis on the cross-section of the coating.

The X-ray spectrum of the cross-section gives clear cut idea about the different elements present in the sample whether it is for the coating, and the contaminants. W and C represent the WC layer, while Cr represents the chromium under layer. Fe represents the base material.

7.2. Micro-hardness analysis

7.2.1. Electroless nickel coatings - pulleys

The following table showcases the microhardness test results carried out on the cross-section of the different stages in the electroless nickel coating process. Microhardness measurement is a characteristic of the wear behavior of the coating. The higher the microhardness, the better the wear resistance of the coating. Microhardness analysis can also be used to identify whether the sample has been subjected to heat treatment or not. Heat treated parts will have high micro hardness compared to those which have not undergone heat treatment. By looking at the table, it is quite clear that sample A and sample C have very high hardness compared to the other samples of the coating process. This is since sample A and C have been heat treated as we have discussed in the previous session. It can also be concluded that sandblasting (sample E) and steam-treatment (vaporizing – sample F) considerably reduces the microhardness of the coating surface.

Sample (A)	**Sample (B)**	**Sample (C)**	**Sample (D)**	**Sample (E)**	**Sample (F)**
958	572	931	572	247	231
964	567	936	615	236	229
958	576	942	587	239	235
947	568	939	599	241	224
962	570	935	584	239	231

Table 7.1 Microhardness test results of different samples of electroless Nickel coating.

7.2.2. Hexavalent Chromium

The table 7.2 and 7.3 represents the microhardness analysis of hexavalent chromium and trivalent chromium respectively. It can be seen that hard chromium coatings have high microhardness in comparison with all the other coatings (PVD, electroless nickel), in that itself Cr (VI) being the hardest. The interesting thing about this result of Chromium coating is that these values are generated without the specimen being subjected to heat treatment. So, it can be concluded that chrome coatings in general have very high microhardness values.

Surface hardness	1130	1106	1047

Table 7.2 Microhardness of Cr (VI).

Surface hardness	1000	1047	1150

Table 7.3 Microhardness of Cr (III).

7.2.3. PVD coatings – DLC, WCC, CrN

The microhardness test could not be carried out for the above coatings due to the dimensions of the samples as the samples were rectangular with a very thin structure. In order to perform the Vicker's test with the device available at Stellantis, the samples should have a certain thickness which was not the case with these samples.

7.3. Corrosion resistance – Neutral salt spray test

7.3.1. Trivalent chromium sample

The trivalent chromium sample that has been subjected to neutral salt spray test got corroded very easily even though the coating had a significantly higher thickness. It only took around 3 days to get the sample completely corroded. Figure 7.60 represents the fully corroded sample. Figure 7.61 represents the initial sample kept in the chamber. The reason why this happened was due to the lack of a nickel underlayer

beneath the trivalent coating layer. The presence of nickel under layer improves the corrosion resistance of the coatings significantly. So, it should be noted that wear resistant parts that are coated with trivalent chromium should not be used in aggressive environments.

Figure 7.60 Fully corroded trivalent sample.

Figure 7.61 Trivalent sample before subjecting to corrosion.

7.3.2. Hexavalent chromium coating

We have discussed above that nickel underlayer provides improved corrosion resistance for metal coatings. However, in the case of Cr (VI) coatings, the nickel underlayer is not required to obtain high corrosion resistance. They have already high corrosion resistance properties even without the nickel underlayer. Even after keeping the sample for more than one month in the salt spray chamber, the sample looked good as new. Hexavalent chromium can be used in any aggressive environment. Figure 7.62 represents the sample before keeping in the chamber and figure 7.63 represents the sample after almost one month.

Figure 7.62 Hexavalent chrome before keeping in the chamber.

Figure 7.63 Hexavalent chromium after one month in corrosion chamber.

The top part of the sample got corroded since there was no coating. The remaining part of the sample which had the coating remained intact.

7.3.3. Electroless nickel coatings

In the case of electroless nickel coatings, out of the 6 samples that have been evaluated, sample E and sample F, which were the steam treated and sand blasted sample, got corroded very easily only after 4-5 days in the chamber. In that itself, the sample E (sand blasted) got corroded even faster than the steam treated one. Figures 7.64 and 7.65 represent sample E and F respectively.

Figure 7.64 Sample E after 2 days in the chamber.

Figure 7.65 Sample F after 4-5 days in the chamber.

So, it can be clearly concluded that these 2 samples, that are sample E and sample F, sand blasted and vaporized, cannot be exposed to aggressive environments. Regarding the other samples, they exhibited somewhat high corrosion resistance but not so high when compared with hard chromium Cr (VI) coating. In that itself sample D – vaporized + sand blasted + nickel showed the highest corrosion resistance while the remaining samples showed somewhat similar resistance after almost a month. Figure 7.66 represents sample D after one month in the corrosion chamber.

Figure 7.66 Sample D after one month in the corrosion chamber.

So, in general, it still might not be a good idea to use electroless nickel coatings for highly aggressive environments although it showed considerable resistance for a certain period, it still will not be good enough for such highly aggressive media.

7.3.4. PVD coatings

The corrosion resistance of PVD coatings was also very low. Just after being kept 4 days in the chamber, these coated samples started to get corroded. Among the 3 PVD coatings that has been analyzed, DLC showed better resistance than WC and CrN coatings. Still, it will not be wise to use these coatings for applications involving highly aggressive environments. One reason why these coatings showed very low corrosion resistance might be because of the very low thickness of the coatings. The figures 7.67, 7.68, and 7.69 represent DLC, WC, and CrN samples after 4-5 days in the corrosion chamber.

Figure 7.67 DLC coating after 4-5 days in the chamber.

Figure 7.68 WC coating after 4 -5 days in the chamber.

Figure 7.69 CrN coating after 4-5 days in the chamber.

8 Conclusion

The aim of this study was to create and test a procedure for the initial characterization of a coating prior to performance tests such as wear & tear tests, bench tests etc. This procedure is also useful for finding what type of coating has been applied on parts taken directly from the market. Microscopic methodology is used for analysing the morphology, identifying defects on the coated samples, and thickness of the samples. In this research, the microscopic analysis of both on the surface (SEM) and cross-section (Optical) were carried out. Thickness measurement is carried out to check the uniformity of the distribution of the coating across the entire surface and to make a relationship between thickness and performances (e.g., corrosion resistance). Thickness measurement is included in the micrographic analysis. Another important property, hardness is linked with wear behaviour. Corrosion resistance is a performance test and can be tested on specimens or on components, for e.g., Lever for gear boxes, transmission systems, some small pistons that are used in pneumatic and hydraulic systems in contact with fluids (Fluids could contain substances that can induce corrosion and wear - engine cooling system).

In most of the coatings, the analysis was able to detect the presence of some defects such as stains (SEM analysis) and to detect the nature of the defects. Both SEM & EDS were carried out by the same device. Stains were present due to the coating process & porosity of the base material (sintered material, mostly for nickel coatings). The elemental composition of the material is the same in the stain and outside the stain and this information is relevant because we can assume that these defects do not have an impact on the characteristic of the coating. This means that the parts can be accepted and be subjected to bench/ on vehicle tests. Electron microscopy was used to check the uniformity of the deposit whereas EDS was used to understand the chemical composition of the sample. For instance, sample A (electroless nickel) did not have any sort of contamination while it only consisted of Ni & P. For analysing the coating, EDS must be done on cross-section to get the results for each layer and to reduce the influence of the base material. The EDS analysis on cross-section was able to detect that sand blasting did not completely remove the oxide layer created by steam treatment (Sample D of electroless nickel coating process). This means that, it is possible to have a bad influence on the adhesion between the Ni layer and the base material. This can have adverse effects on bench tests and such parts should be scraped before carrying out bench tests. In short, this analysis gives relevant information about uniformity, contaminants, composition & thickness of the coatings.

Hardness test is a measure of wear behaviour of the coatings. As it was expected, hard chrome samples showed exceptional surface hardness compared to electroless nickel coatings (hardness of PVD coatings could not be carried out due to thickness issue). Microhardness test on the cross-section was able to detect whether the part was heat treated or not. For corrosion resistance, hard chrome samples obtained with hexavalent chromium technology showed the best results when subjected to neutral salt spray test, while the PVD coatings showed much lesser resistance compared to Cr (VI) hard chrome coatings. This has mainly to do with chemical composition of the layers. NSST (neutral salt spray test) showed a low corrosion resistance of the hard chrome plating obtained with a Cr (III) technology. It means that this coating must not be used for applications that are subjected to corrosive environments. To improve the corrosion performance of this type of coating, it is necessary to add a nickel underlayer between the base material and the chromium coating. Regarding the electroless nickel coating process, the steam treated part resulted in poor corrosion resistance while the corrosion resistance of the other samples was in between that of the hexavalent chromium and PVD coatings. It means that steam treated parts cannot be used in applications that are in contact with aggressive environments while electroless nickel plated parts characterized by a thickness of the layer lower than 25 micrometres can be used in moderately aggressive environments.

In this work, the procedure that has been created and tested is able to detect defects and evaluate their natures. This procedure is also able to analyse details on the type of coatings applied on the parts and to detect the presence of a heat treatment on the specimens. Finally, it can provide indirect information about the wear resistance, and direct details about corrosion resistance of the coatings.

Bibliography

1. A.S. Racz , Z. Kerner, M. Menyhard. (2022). Corrosion resistance of tungsten carbide-rich coating layers produced by . *Applied Surface Science*.
2. B. Podgornik, O. Massler, F. Kafexhiu, M. Sedlacek. (2018). Crack density and tribological performance of hard-chrome coatings. In *Tribology International 121* (pp. 333-340).
3. C. Rincon , G. Zambrano , A. Carvajal , P. Prieto , H. Galindo , E. Martınez , A. Lousa , J. Esteve. (2001). Tungsten carbide/diamond-like carbon multilayer coatings on steel for tribological applications. *Surface and Coatings Technology 148*, 277-283.
4. Donald M. Mattox. (n.d.). HANDBOOK OF PHYSICAL VAPOR DEPOSITION (PVD) PROCESSING. In *Film Formation, Adhesion, Surface Preparation and Contamination Control.* Westwood, New Jersey, U.S.A.: NOYES PUBLICATIONS.
5. Electroplating. (n.d.). In *Metallurgical industry 7/96* (pp. 12.20, 1-17).
6. Fernando B. Mainier, Maria P. Cindra Fonseca, Sérgio S. M. Tavares, Juan M. Pardal. (2013). Quality of Electroless Ni-P (Nickel-Phosphorus) Coatings Applied in Oil Production Equipment with Salinity. *Journal of Materials Science and Chemical Engineering*, 1-8.
7. Horner, J. (1994). *"Electroplating",Kirk-othmer Encyclopedia of Chemical Technology, 4th Ed., Volume No.9.* New York: John Wiley and Sons, Inc.
8. (n.d.). *https://cdn.standards.iteh.ai/samples/31876/a4cd5a83f7c246218937dd448607b462/ISO-4516-2002.pdf.*
9. K. Legg, M. Graham, P. Chang, F. Rastagar, A. Gonzales and B. Sartwell. (May 1996). The replacement of electroplating. In *Surface Coating Technology, Vol.81* (pp. 99-105).
10. L. M. Apininskaya; I. D. Radomysel'skii. (1965). The electroless nickel plating of porous sintered iron-base parts., 4(5).
11. P Gillespie. (n.d.). Electroless nickel coatings: case study.

12. Podgornik B, Vilhena LM, Sedlacek M, Rek Z, Zun I. (2012). Effectiveness and design of surface texturing for different lubrication regimes. *Meccanica*, 47:1613-22.

13. R. A. Lane, C. Fink, C. Grethlein and N. Rome. (Sept. 2012). "Analysis of alternatives to hexavalent chromium: A program management guide to minimize the use of CrVI in military systems". AMMTIAC-WSTIA, vol. 1, no. 2.

14. R. A. Lane, C. Fink, C. Grethlein and N. Rome. (Sept. 2012). Analysis of alternatives to hexavalent chromium. In *A program management guide to minimize the use of CrVI in military systems* (pp. 3-9). AMMTIAC-WSTIA, vol. 1, no. 2.

15. Sedlacek M, Podgornik B, Vizintin J. (2012). Correlation between standard roughness parameters skewness and kurtosis and tribological behaviour of contact surfaces. *Tribology International*, 48:102-12.

16. (n.d.). *Technical_Data_Sheet_CrN_PVD_coatings.*

17. (n.d.). *Technical_Data_Sheet_DLC_PVD coating.*

18. (n.d.). *Technical_Data_Sheet_Electroless_Nickel_High_Phosphorous.*

19. (n.d.). *Technical_Data_Sheet_Electroless_Nickel_Medium_Phosphorous.*

20. (n.d.). *Technical_Data_Sheet_Hexavalent_chrome.*

21. (n.d.). *Technical_Data_Sheet_trivalent_chrome.*

22. (n.d.). *Technical_Data_Sheet_WC_PVD_coatings.*

23. Yong Choi , M. Kim , S.C. Kwon . (2003). Characterization of chrome layer formed by pulse plating. *Surface and Coatings Technology 169 – 170*, 81-84.